Calibration of the Advanced X-ray Astrophysics Facility (AXAF): Project Science analyses

M. C. Weisskopf
NASA, Marshall Space Flight Center, ES01

R. F. Elsner, J. J. Kolodziejczak, S. L. O'Dell, M. E. Sulkanen, and A. F. Tennant
NASA, Marshall Space Flight Center, ES84

R. A. Austin, D. A. Swartz, and G. Zirnstein
USRA, Marshall Space Flight Center, ES84

(DRAFT: Editing is incomplete.)

Interim report

May 6, 1999

Abstract

This document is the interim report on Project Science analyses of data from the calibration of the Advanced X-ray Astrophysics Facility (AXAF). The report provides an introduction to AXAF calibration activities at the X-Ray Calibration Facility (XRCF) and then describes Project Science analyses of calibration data:

1. Beam-Normalization Detector (BND) data for X-ray Source System (XSS) monochromators;
2. Beam-uniformity data for X-ray Source System (XSS) monochromators;
3. Solid-State Detector (SSD) internal calibrator;
4. Solid-State Detector (SSD) continuum measurements;
5. Flight Contamination Monitor (FCM); and
6. Limits on High-Resolution Mirror Assembly (HRMA) contamination.

Contents

List of Figures

List of Tables

1 Introduction

This document is Project Science's contribution to the interim report on the calibration of AXAF. Each AXAF Science Instrument team has provided an interim report on the calibration analyses for which it is responsible. In order to facilitate the reading of this document, as well as the other documents comprising the full interim report, we begin by giving an overview [1] of XRCF calibration instrumentation (§1.1) and of XRCF calibration activities (§1.2). We then summarize those calibration analyses for which Project Science is responsible (§1.3), which is the subject of this document.

1.1 Calibration instrumentation at the XRCF

The X-Ray Calibration Facility (XRCF), operated by MSFC's System Analysis and Integration Laboratory (SAIL), provides a 518-m guide tube separating the x-ray-source building from the Instrument Chamber (IC). For a table of relevant distances and their estimated errors, for configurations used during the calibration of AXAF at the XRCF, please visit the Project Science calibration page at `http://wwwastro.msfc.nasa.gov/xray/xraycal/`.

In this section, we describe x-ray instrumentation, both ground-support and flight, used during AXAF testing and calibration at the XRCF. Figure 1 illustrates the x-ray components employed during the calibration — namely, the source system (§1.1.1), the monitor detectors (§1.1.2), the x-ray optics (§1.1.3), the transmission gratings (§1.1.4), and the focal-plane detectors (§1.1.5).

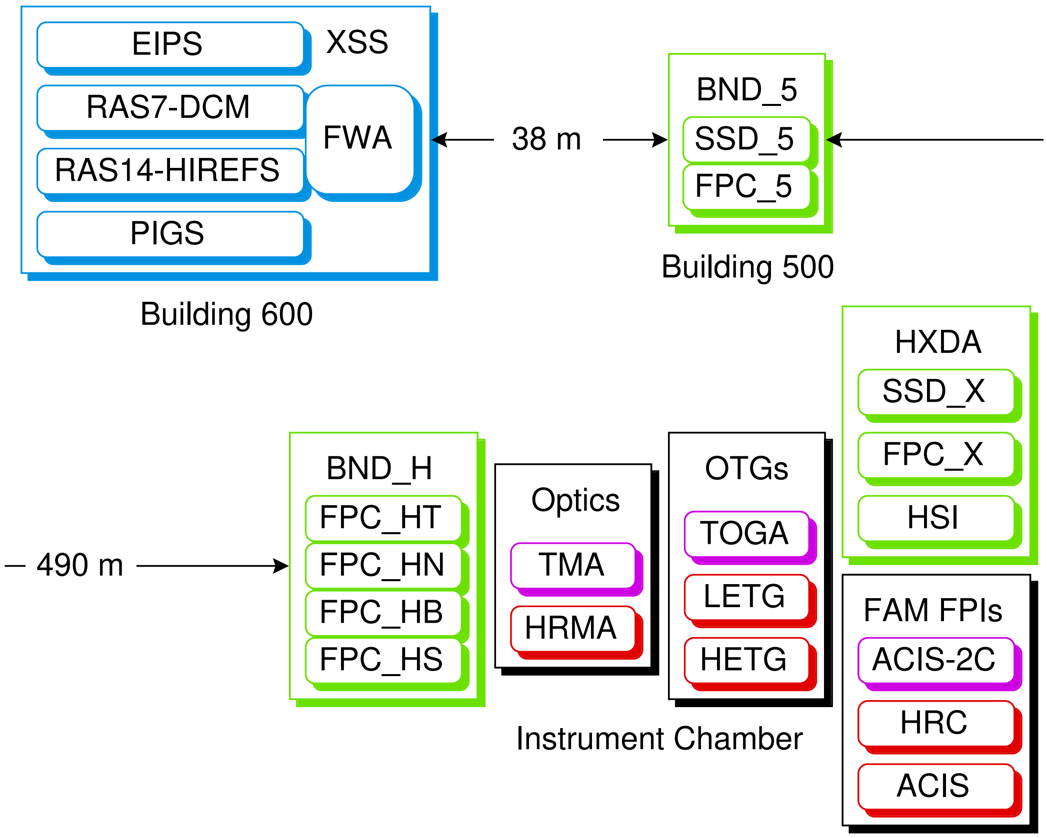

Figure 1: Configurations of x-ray sources, monitor detectors, optics, transmission gratings, and focal-plane detectors during calibration of the AXAF observatory at the X-Ray Calibration Facility (XRCF).

1.1.1 X-ray Source System (XSS)

The X-ray Source System (XSS) [2] comprises a conventional electron-impact source, two monochromators, a Penning source, and transmission filters. MSFC SAIL integrated the XSS; AXAF Project Science characterized the XSS prior to AXAF calibration. In addition to the x-ray sources of the XSS, the AXAF optics and both focal-plane instruments employ flight, radioactive calibration sources to ensure an accurate ground-to-orbit transfer of the AXAF flux scale [3].

Electron-Impact Point Source (EIPS) MSFC's System Analysis and Integration Laboratory (SAIL) developed the Electron-Impact Point Source (EIPS), which produces electron-induced fluorescence lines and bremsstrahlung in its fixed, oil-cooled anode. Numerous interchangeable, conical-anode targets provide atomic K and L lines over the AXAF energy range (0.1–10 kev).

Double-Crystal Monochromator (DCM) The National Institute of Standards and Technology (NIST) fabricated the dual-pentagonal-turret Double-Crystal Monochromator (DCM, §2.2.1, Figure 2). The AXAF calibration employed Thallium Acid Phthalate (TAP001), germanium (Ge111), and abraded silicon (aSi400) crystals to span the respective energy ranges 0.7–2.3, 2.1–9.0, and 6–12 keV. Rigaku manufactured the Rotating Anode Source (RAS) used with the DCM.

Reflection-grating monochromator (HIREFS) Hettrick Scientific fabricated the reflection-grating monochromator, the HIgh-Resolution Erect Field Spectrometer (HIREFS^{TM}, §2.2.1, Figure 3). The AXAF calibration employed 3 of the HIREFS' 4 selectable gratings to span the respective energy ranges 0.12–0.40, 0.30–1.2, and 0.9–2.0 keV. Rigaku manufactured the Rotating Anode Source (RAS) used with the HIREFS.

Penning Ionization Gas-discharge Source (PIGS) The Smithsonian Astrophysical Observatory (SAO) Mission Support Team (MST) provided the Penning Ionization Gas-discharge Source (PIGS); MSFC SAIL refurbished the PIGS during the calibration. The PIGS produces narrow, soft-x-ray L lines of ionized aluminum and argon, for calibrating spectral resolution of the AXAF gratings in the energy range 0.07–0.25 keV (wavelengths 170–50 Å).

Filter-Wheel Assembly (FWA) MSFC's System Analysis and Integration Laboratory (SAIL) developed a dual-wheel Filter-Wheel Assembly (FWA), which holds assorted x-ray transmission filters, pin holes, occulting bars, and open (unobstructed) apertures. Nominally, the filters provide 2, 4, or (when used in combination) 6 mean-free-path attenuation at the characteristic lines of EIPS anode targets.

1.1.2 Beam-Normalization Detectors (BNDs)

The Smithsonian Astrophysical Observatory (SAO) Mission Support Team (MST) provided the HRMA X-ray Detection System (HXDS) [4], which comprises Beam-Normalization Detectors (BNDs) to monitor the x-ray source and (non-flight) focal-plane detectors (§1.1.5) to characterize x-ray optics (§1.1.3) and gratings (§1.1.4). Of the 6 BNDs, one is a Solid-State Detector (SSD) and the other 5 are Flow Proportional Counters (FPCs).

Solid-State Detector (SSD) The BND SSD ("SSD_5"), residing approximately 38 m from the XSS (§1.1.1), is a liquid-nitrogen-cooled, high-purity-germanium (hpGe) detector [5]. In front of the detector's 6-mm-diameter active area, lies an aperture wheel, holding circular apertures up to 5-mm diameter and a radioactive calibration source. Prior to the AXAF calibration, SAO and Physikalisch–Technische Bundesanstalt (PTB) calibrated [6] this SSD at the Berliner Elektronenspeicherring-Gesellschaft für Synchrotronstrahlung (BESSY).

Flow Proportional Counters (FPCs) One BND FPC ("FPC_5") lies slightly in front of the BND SSD (SSD_5), about 38 m from the XSS (§1.1.1). This BND, FPC_5, has an aperture slide, with aperture diameters of 1, 4, 12, and 36 mm; it is mounted on a 2-degree-of-freedom stage, for mapping the x-ray beam. Four BND FPCs ("FPC_H") reside just in front of the x-ray optic, about 526 m from the source; one of these is mounted on a 2-degree-of-freedom stage for mapping the x-ray beam near the optic's entrance aperture. SAO and PTB will calibrate the absolute efficiencies of the FPCs at BESSY.

1.1.3 X-ray optics

Calibration activities at the XRCF involved not only the flight optic, the High-Resolution Mirror Assembly (HRMA), but a non-flight optic, the Technology Mirror Assembly (TMA).

High-Resolution Mirror Assembly (HRMA) The Eastman Kodak Company (EKC) aligned and assembled the HRMA; Hughes Danbury Optical Systems (HDOS) figured and polished its Zerodur mirrors; and Optical Coatings Laboratories Inc. (OCLI) sputter-coated the optical surfaces with iridium. With 4 Wolter-1 mirror shells (segment lengths of 0.83 m and diameters of 0.63, 0.85, 0.97, and 1.2 m), the HRMA [7, 8] provides both high-resolution (sub-arcsecond) imaging and a large (1140 cm^2) geometric area. With a focal length of 10 m, the HRMA focal-plane plate scale is about 50-μm/arcsec. EKC provided HRMA ground-support equipment, including actuators to yaw and pitch the HRMA for off-axis measurements and a 16-shutter assembly to isolate specific HRMA mirror-shell quadrants.

Technology Mirror Assembly (TMA) The TMA is a gold-coated 60%-scale model of the smallest of the AXAF's 4 mirror shells. Fabricated and tested a decade earlier, as a demonstration of technologies to be used in producing the mirrors for AXAF, the TMA served as a surrogate optic during calibration rehearsals, prior to arrival of the (flight) HRMA.

1.1.4 Objective transmission gratings

Located immediately behind an optic, objective transmission gratings (OTGs) disperse the convergent beam, to form high-resolution spectra near the focal plane. The AXAF observatory has 2 OTGs — the Low-Energy Transmission Grating (LETG) and the High-Energy Transmission Grating (HETG) — either of which may be inserted into the x-ray path behind the HRMA. Matched to the TMA's geometry, the custom-built TMA Objective Grating Assembly (TOGA), using flight-type gratings from the LETG and the HETG, allowed a realistic rehearsal prior to the HRMA's arrival at the XRCF.

Low-Energy Transmission Grating (LETG) Designed and fabricated by the Space Research Organization of the Netherlands (SRON) and the Max-Planck-Institut für extraterrestrische Physik (MPE), the LETG comprises 540 16-mm-diameter free-standing-gold facets, mounted (3 per module) on a ring structure which locates the facets on the Rowland toroid which includes the focal plane. The Low-Energy Grating (LEG), free-standing gold bars of about 991-nm period, provide high-resolution spectroscopy from 0.08 keV to 2 keV.

High-Energy Transmission Grating (HETG) Designed and fabricated by the Massachusetts Institute of Technology (MIT), the HETG comprises 336 25-mm-square polyimide-supported-gold facets, mounted (1 per frame) on a ring structure which locates the facets on the Rowland toroid. The HETG functions as 2 gratings with slightly rotated dispersion directions: Medium-Energy Gratings (MEG), with a 400-nm period, lie behind the HRMA's outer 2 mirror shells, for high-resolution spectroscopy from 0.4 keV to 4 keV; High-Energy Gratings (HEG), with a 200-nm period, lie behind the inner 2 shells, for high-resolution spectroscopy from 0.8 keV to 8 keV.

TMA Objective Grating Assembly (TOGA) The Massachusetts Institute of Technology (MIT) designed and fabricated the TOGA for use with the TMA. Employing all 3 flight-type grating facets (LEG, MEG, HEG), oriented with different dispersion directions, the TOGA provided early diagnostic data on each type of grating, and the opportunity to rehearse spectroscopy data collection and analysis.

1.1.5 Focal-plane detectors

The AXAF observatory has 2 focal-plane science instruments — the (microchannel plate) High-Resolution Camera (HRC) and the AXAF CCD Imaging Spectrometer (ACIS). Each provides two detectors: The "I" detector is primarily fro direct imaging; the "S" detector is primarily for reading out dispersed spectra of the LETG or of the HETG.

Prior to arrival of the HRC and ACIS at the XRCF, the rehearsal and the HRMA calibration employed 4 non-flight focal-plane detectors. Three of these — an SSD, an FPC, and the (microchannel plate) High-Speed Imager (HSI) — are part of the HRMA X-ray Detector Assembly (HXDA), which also incorporates a 3-degree-of-freedom stage, an SSD aperture wheel, and an aperture plate for the FPC. The SAO Mission Support Team (MST) provided the HXDA, which, with the (monitor) BNDs (§1.1.2), comprise the HRMA X-ray Detection System (HXDS). In addition, the (non-flight) ACIS two chip (ACIS-2C) served as a surrogate CCD detector, to provide practice in CCD data collection and analysis and to calibrate its flight-type CCDs. Ball Aerospace and Technologies designed and fabricated the Five-Axis Mount (FAM) which positioned the ACIS-2C, as well as the HRC and ACIS.

High-Resolution Camera (HRC) The Smithsonian Astrophysical Observatory designed and fabricated the HRC [9]. The HRC-I and HRC-S employ 6°-chevron pairs of low-noise microchannel plates (MCPs), coated with cesium–iodide (CsI) and covered with an aluminized-polyimide UV/ion shield. For both HRC-I and HRC-S, the spatial resolution is better than 20 μm (< 0.4 arcsec) and the read-out resolution is 6.4 μm (0.13 arcsec). With a 93-mm-square active area, HRC-I has a 31-arcmin field of view; with an approximately 300-mm-by-20-mm area and good soft-x-ray efficiency, the tri-segmented HRC-S is the primary read-out for the LETG, providing spectral coverage shortward of 160 Å.

AXAF CCD Imaging Spectrometer (ACIS) The Pennsylvania State University (PSU) and the Massachusetts Institute of Technology (MIT) designed and fabricated the ACIS with Lockheed–Martin. The ACIS-I and ACIS-S employ large-format (25-mm square) CCDs with 24-μm-square (0.5 arcsec) pixels, covered with an aluminized-polyimide optical blocking filter. All I CCDs and 4 of 6 S CCDs are front-side devices, with little response below 0.4 keV; 2 S CCDs are back-side, affording useful response down to 0.2 keV. With a 50-mm-square area, ACIS-I has a 17-arcmin field of view; with a 150-mm-by-25-mm area, the ACIS-S is the primary read-out for the HETG.

Focal-plane Solid-State Detector (SSD_X) One of the 3 detectors of the HRMA X-ray Detector Assembly (HXDA) is a solid-state detector, designated "SSD_X". The SSD_X is identical to the BND (monitor) detector SSD_5 (§1.1.2). Except for the absence of a radioactive calibration source, the SSD_X aperture wheel is also identical to that of SSD_5.

Focal-plane Flow Proportional Counter (FPC_X) Another of the 3 HXDA detectors is a Flow Proportional Counter, designated "FPC_X". The FPC_X is identical to the 5 BND (monitor) FPCs (§1.1.2). A 2-degree-of-freedom aperture plate, with circular apertures up to 35-mm-diameter for measuring encircled energy and slits for measuring dispersed spectra from the OTGs, lies in front of FPC_X.

High-Speed Imager (HSI) The third HXDA detector is the High-Speed Imager, an uncoated microchannel plate (MCP), with 18-mm-diameter active area and 6.4-μm (0.13-arcsec) read-out resolution.

ACIS Two-Chip (ACIS-2C) The ACIS team (PSU and MIT) and SAO designed, fabricated, and operated the ACIS two chip (ACIS-2C), comprised of one front-side and one back-side flight-type CCDs.

1.2 Calibration activities at the XRCF

Occurring in 12 at-vacuum phases (§1.2.1), calibration activities at the XRCF occupied 6 months of intense (around-the-clock) activity over a one-year period. During this period, calibration of AXAF-observatory subsystems occupied 4 months (§1.2.2), including 3 x-ray months of data collection.

1.2.1 Calibration phases

Table 1 shows the purpose, configuration, and duration of the dozen AXAF-related phases during which the XRCF Instrument Chamber was at vacuum and x-ray data were being acquired. XRCF calibration of the (flight) AXAF observatory system or subsystems occurred in 6 vacuum phases, which were required for planned change-out of focal-plane instrumentation and for repairs to ground-support equipment.

Table 1: XRCF configurations for the AXAF calibration.

CMDB	Phase	X-ray optic	Gratings	FP instrument	Days
	HXDS T&V 1	TMA	TOGA	HXDA	7
A	Rehearsal 1	TMA	TOGA	HXDA	12
B	Rehearsal 2	TMA	TOGA	ACIS-2C	7
	HXDS T&V 2	TMA	TOGA	HXDA	10
C	Calibration 1.1	HRMA	LETG, HETG	HXDA	4
D	Calibration 1.2	HRMA	LETG, HETG	HXDA	26
E	Calibration 1.3	HRMA	LETG, HETG	HXDA	14
F	Calibration 2.1	HRMA	LETG, HETG	ACIS-2C	16
G	Calibration 2.2	HRMA	LETG, HETG	HRC	24
H	Calibration 2.3	HRMA	LETG, HETG	ACIS	8
I	Cross-calibration 1	none	none	ACIS	10
J	Cross-calibration 2	none	none	HXDA	10

1.2.2 Observatory calibration timeline

During daily meetings led by Project Science, the Science team planned impending measurements in a detailed Calibration Measurements Data Base (CMDB), maintained by the AXAF Science Center (ASC). Based on the CMDB, the TRW Test Conductor prepared a test-list script for conducting the planned measurements.

Table 2 shows all calibration phases during which the flight optic (HRMA) was present — namely, CMDB series C–H (see Table 1). Recorded in Table 2, for each phase, are start date of the first measurement, end date of the last measurement, duration in x-ray days, total integration time, number of measurements, and average efficiency ((integration days)/(x-ray days)). Despite a few failures in ground-support equipment, which were eventually rectified, daily — and, in some cases, real-time — replanning of the CMDB enabled useful data collection to continue, with minimal loss of efficiency.

Table 2: Timeline for AXAF calibration measurements at the XRCF.

CMDB	First x ray	Last x ray	X-ray days	Integ. days	Number	Efficiency
C	12/19/1996	12/24/1996	4.40	0.76	96	0.172
D	12/31/1996	01/26/1997	25.71	8.07	799	0.314
E	01/28/1997	02/11/1997	13.58	6.23	277	0.459
F	02/22/1997	03/10/1997	16.46	8.19	584	0.498
G	03/19/1997	04/12/1997	23.84	16.31	1111	0.684
H	04/17/1997	04/26/1997	8.25	5.50	303	0.666
			92.24	**45.05**	**3170**	**0.488**

1.3 Project Science analyses

Project Science is performing analyses of certain data from the AXAF calibration at the XRCF. The remainder of this document constitutes our interim report on these analyses, which we summarize briefly below.

1.3.1 BND data for XSS monochromators

In view of its necessity for analyzing many calibration measurements performed with the flight instruments, our highest priority is the analysis of BND data for the DCM and HIREFS monochromators (§2). Owing to potential contributions from higher spectral orders and the near absence of continuum emission, the spectral-fitting analyses for the monochromators differ significantly from those for the EIPS, which the Mission Support Team is performing.

1.3.2 Beam uniformity of XSS monochromators

Monochromators offer the great advantages of a tunable x-ray source; however, the beams of monochromators are inherently nonuniform. Owing to potentially large spatial variations in the x-ray beam, the beam-uniformity data for the monochromators (§3) require more elaborate analyses than those for the EIPS.

1.3.3 SSD internal calibrator

A radioactive source in the SSD_5's aperture wheel permits calibration of the SSD_5's gain and energy resolution and monitors changes in its response, e.g., due to accumulation of ice on the detector's window. Knowledge of changes in the SSD_5's response is critical for those measurements for which SSD_5 was the primary monitoring detector. Thus, our next highest priority is analysis of SSD_5 data taken with its calibration source in place (§4).

1.3.4 SSD continuum measurements

To complement HRMA calibration measurements using the EIPS optimized for line emission and the focal-plane FPC (FPC_X), the HRMA calibration included measurements using the EIPS optimized for continuum emission and the focal-plane SSD (SSD_X). These allow simultaneous measurement of the HRMA effective area for energies exceeding about 1 keV, at the spectral resolution of the SSD. In view of the importance of accurately calibrating the effective area, the analysis of the SSD continuum measurements (§5) is a high priority. The Mission Support Team has performed extensive analyses subsequent to the preliminary report.

1.3.5 Flight Contamination Monitor (FCM)

The HRMA's Forward Contamination Cover (FCC) contains 16 (1 per shell quadrant) radioactive calibration sources. This system of sources, the Flight Contamination Monitor (FCM), will serve to confirm the ground-to-orbit transfer of the AXAF flux scale, which could be compromised by post-XRCF changes in the contamination of the mirrors' surfaces. Hence, the analysis of the FCM data (§6) provides a baseline for comparison to similar measurements to be acquired during the orbital activation of AXAF.

1.3.6 Limits on HRMA contamination

Having recognized the potential influence of contamination on AXAF performance, the AXAF Project has maintained rigorous contamination controls. While all contamination monitoring indicates that the HRMA should be quite clean, it is important to confirm this in the x-ray calibration measurements. In that this is derivative to other analyses of the calibration measurements, the use of x-ray data to set limits on HRMA contamination started after the aforementioned analyses. Here (§7) we present initial results of the analysis, which set an upper limit on the particulate contamination. Owing to the lack of success in modeling the effective area, we are not yet able to establish limits on molecular contamination.

2 BND data for XSS monochromators

2.1 Objectives

This section is the interim report on spectral analysis of data acquired with the Beam Normalization Detectors (BNDs), during AXAF calibration maeasurements using the XRCF monochromators — the Double-Crystal Monochromator (DCM) and the HIgh-Resolution Erect-Field Spectrometer (HIREFS^{TM}) reflection-grating monochromator. The monochromators offer valuable capabilities: They provide high spectral purity at high spectral resolution and, with nearly continuously selectable energies over a large bandwidth, the ability to scan across many spectral features in the response of the gratings and focal-plane detectors. On the other hand, analysis of the monochromator data require special treatment: The beams are inherently spatially nonuniform, the spectra contain higher spectral orders at many energies which can severely overlap in the relatively low-resolution BNDs, HIREFS spectra also contain spectral lines from the tungsten anode scattered in the monochromator, and tuning of the DCM exhibits some non-repeatability. We address each of these issues in this and the following section (§3).

Here we describe spectral analysis of data taken with the five Flow Proportional Counter (FPC) BNDs. Other contributors will describe analysis of data taken with focal-plane instruments. Our goal is to provide, for each calibration measurement, background-corrected flux (photons s^{-1} cm^{-2}) at the HRMA node, in each spectral feature, incident upon each quadrant of the HRMA's 4 mirror shells. Together with focal-plane data, one may then use data obtained suring monochromator measurements, to generate calibration data products, such as shell-by-shell effective areas.

From Pulse-Height Amplitude (PHA) spectra, we extract spectral content by fitting the data with a *jmkmod* model [10] within the XSPEC [11] spectral fitting package. First we describe the monochromators and BNDs (§ 2.2) and then the procedures used in the spectral analysis (§ 2.3). Next we dicuss trends in the results of the data analysis (§ 2.4) and the data products and their current status (§ 2.5).

The principal refinements highlighted here, relative to our preliminary report (1997 October 17), are these:

1. Use of a physical model of the monochromators to predict the energy-dependent spatial content pf the beam (§ 3). We have applied the new spatial fitting procedure to all monochromator measurements, superseding our previous beam-uniformity (BU) analysis results.

2. Use of improved FPC quantum efficiencies, as provided by the Mission Support Team (§ 2.2.2)

3. Re-fitting of a large number of individual spectra, in order to reduce formal fitting uncertainties.

At this point, we have completed analysis of spectral data obtained during ACIS 2-chip (ACIS-2C), HRC, ACIS, and ACIS cross-calibration (flat-field) measurements. Unresolved difficulties correlating PHA spectra to source settings currently precludes successful analysis of data from HRMA–HXDA measurements (CMDB Series D and E, obtained 1997 January 21–23 and February 5–7, respectively). Future work will include the following:

- Analysis of DCM data from Series D and HIREFS data from Series E.
- Re-examination of spectra with severely overlapping spectral features, to ensure all spectral components are accounted for, if possible (§ 2.4.2), including W Mη_1.
- Re-evaluation of the use of the χ^2 figure of merit, versus maximum-likelihood methods (§ 2.4.1).

2.2 Measurement descriptions

The X-ray Source System (XSS, § 1.1.1) includes 2 monochromators — the Double-Crystal Monochromator (DCM) and the HIgh-Resolution Erect-Field Spectrometer (HIREFS^{TM}). In that the characteristics of the DCM and HIREFS differ substantially from those of the other XSS sources, we first describe the monochromators' unique features, as they pertain to reduction and analysis of XRCF data (§ 2.2.1). We also describe relevant properties of the BNDs (§ 2.2.2, also § 1.1.2) and briefly review characteristics of the raw data (§ 2.2.3). For more details, see presentations from the (1996 June) Calibration Readiness Review, at `http://wwwastro.msfc.nasa.gov/xray/xraycal/xssrr`.

2.2.1 Monochromators

Double-Crystal Monochromator (DCM) For operation of the DCM, Turret-1 rotation (Figure 2) selects the energy satisfying the Bragg condition; Turret-2 rotation then makes the 2 crystal faces parallel. Turret-2 translation parallel to the optical axis holds fixed the beam displacement and, hence, the apparent source position. Attached to the DCM is the Rotating-Anode Source RAS7 (also called "RAS North"), containing a tungsten anode drum. The AXAF calibration measurements used only 3 of the 5 turret faces — Thallium Acid Phthalate (TAP001) for 0.7–2.3 keV, germanium (Ge111) for 2.1–9.0 keV, and, rarely, abraded silicon (aSi400) for 6–12 keV. A few DCM measurements — particularly, of the PSF inner core —utilized the x-ray transmission filters in the dual-wheel filter assembly, in order to limit the flux at specific energies.

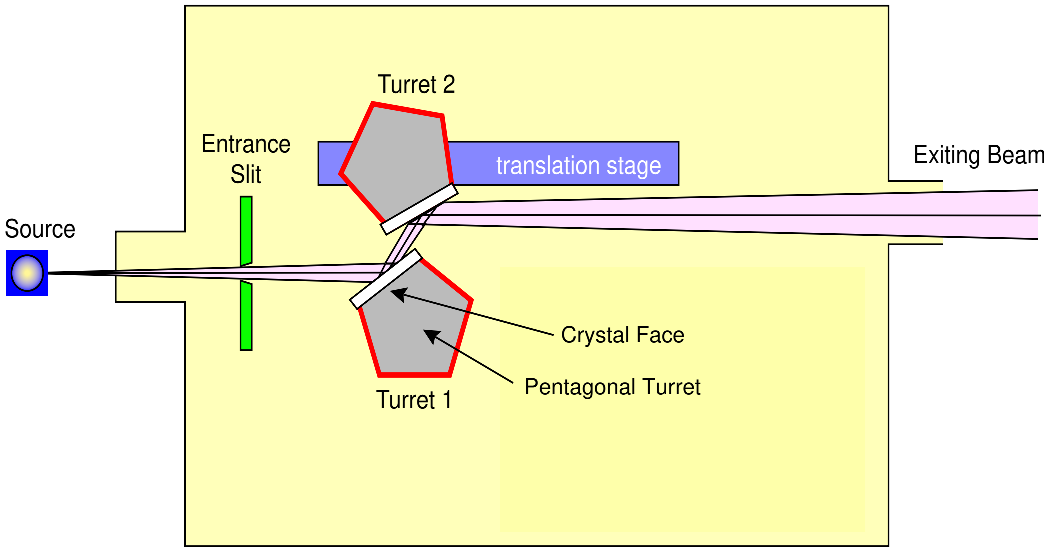

Figure 2: Schematic top view of the optical elements and path for the DCM–RAS7 monochromator. X rays from RAS7 Bragg reflect off the parallel crystal faces of the pentagonal turrets. The calibration of AXAF employed only the TAP, Ge, and Si crystals.

Most calibration measurements using the DCM employed a "mini-scan" while setting the energy, in order to optimize the flux in the first spectral order. During a DCM mini-scan, typically lasting about 30 s, FPC_5 monitored the flux while Turret 2 rotated in small steps independently of the Turret-1 position. The degree of tuning or detuning varied from measurement to measurement, even at the same selected energy. Furthermore, the FPC_5 was in its home position rather than at the Facility Optical Axis (FOA) for some mini-scans, which results in optimization at a different detuning angle and, hence, effects different beam spatial properties. In order to match the spatial variation of the beam, as deduced from BU measurements (or, from interpolations of BU measurements to other energies), to a given calibration measurement, we must allow for the detuning angle.

Although the RAS7 operates at high voltage to generate a strong continuum, the tungsten (W) anode also produces several strong W lines, the most prominent being M$\alpha_{1,2}$ (1.775 keV), Mβ (1.835 keV), and Mζ_1 (1.384 keV), and L$\alpha_{1,2}$ (8.398, 8.335 keV). Because the DCM's beam is slightly energy dependent in its dispersive direction, aligned to the XRCF Y (horizontal) axis, there is significant beam nonuniformity when the DCM is tuned to energies near these spectral lines, the strongest of which lie in the TAP energy range. Furthermore, measurements made using the TAP crystal showed additional beam nonuniformity due to curvature of the crystal's surface (§ 3). In contrast, the Ge beam was highly uniform: The only W lines within the Ge operating energy range are $L\alpha_1$ (8.398 keV) and $L\alpha_2$ (8.335 keV), at the extreme end of its range; furthermore, the crystal's surface is relatively flat (§ 3).

While the contribution of higher spectral orders is generally small for the DCM, higher orders are observed in the energy range 1.5–2.2 keV for the TAP crystal. Higher spectral orders are very weak for the Ge crystal.

High-Resolution Erect-Field Spectrometer (HIREFS) The HIREFS$^{\mathrm{TM}}$monochromator (Figure 3) offers 4 selectable reflection gratings. The AXAF calibration measurements used only 3 of these — SX for 0.8–1.9 keV, SA for 0.25–1.2 keV, and, rarely, SB for 0.1–0.4 keV. The HIREFS's beam is nonuniform, both in its dispersive direction (XRCF Y, horizontal) and in its cross-dispersive direction (XRCF Z, vertical), typically varying by ±20% over the HRMA's aperture.

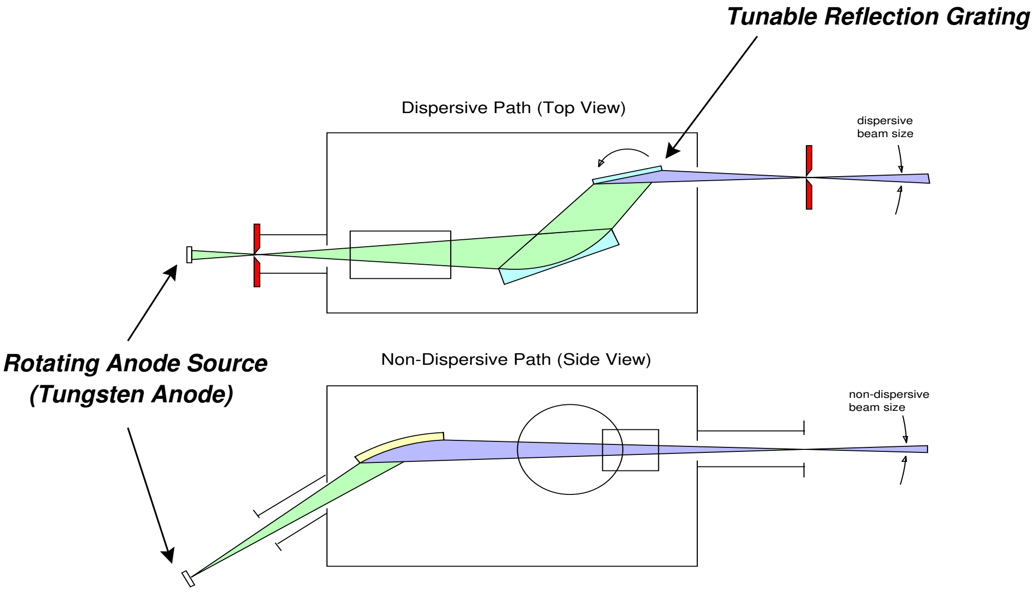

Figure 3: Schematic of the optical elements and path for the HIREFS–RAS14 monochromator. X rays from RAS14 reflect off a flexible astigma-adjusting mirror, then a spherical mirror, before being dispersed by a selectable reflection grating and focussed (in the dispersive direction) onto the exit slit.

Attached to the HIREFS is the Rotating-Anode Source RAS14 (also called "RAS South"), containing a tungsten anode drum. Owing to scattering in the HIREFS, the strongest W line in the HIREFS energy range, M$\alpha_{1,2}$ at 1.775 keV, appears in all FPC PHA spectra of moderate photon counting rate, for which the FPC gain permitted detection of this line. In addition, higher spectral orders are often strong, particularly at low energy ($E \lesssim 0.6$ keV) for the SA grating and throughout the SB energy range, but are absent for the SX grating due to a 2-keV cut-off in the HIREFS optics. Consequently, the spectral fitting algorithms (described below) include higher-order lines and the scattered M$\alpha_{1,2}$ line, in addition to the first-order line. In the fits reported here, we do not include the W Mζ_1 line, which is much weaker than the M$\alpha_{1,2}$ line and usually severely blended with other spectral lines (§ 2.4.2).

2.2.2 Beam-Normalization Detectors (BNDs)

The HRMA X-ray Detection System (HXDS) [4] includes 6 Beam-Normalization Detectors to monitor the x-ray source. One BND is a Solid-State Detector (SSD) [5]; the other 5, Flow Proportional Counters (FPCs) [12]. The 5 FPCs are FPC_5, FPC_HT, FPC_HN, FPC_HB, FPC_HS, corresponding to the FPC in Building 500 and the 4 BND–HRMA (BND_H) detectors located at the top, north, bottom, and south, respectively, of the HRMA entrance aperture (§ 1.1.2). The BND_H detectors have an open aperture area of 35.75 cm^2. FPC_5 has an aperture slide with 36, 12, 4, and 1 mm diameter circular apertures. Because the FPC window-support mesh comprises a cross grid of opaque 100-μm-diameter wires at 2-mm pitch, the geometric area of the larger apertures is reduced by 9.75%.

Mounted on a 2-degree-of-freedom stage, FPC_5 served as the mapping detector for monochromator beam-uniformity (BU) measurements. Although FPC_HN is also mounted on a stage and served for BU measurements using the EIPS source, monochromator fluxes are generally too low for efficient mapping at the distance of the HRMA aperture. Due to its proximity to the source, the high count rate measured by the FPC_5 made it ideal for constraining the spectral model (see below). However, in their monitoring positions, both the FPC_5 and SSD_5 lie too far from the optical axis to be useful for establishing the beam spatial properties during non-BU measurements (§ 3). The SSD_5, with greater spectral resolution compared to the FPCs, served as an aid in identifying spectral features and confirming monochromator spectral 'line' energies. The channel-to-energy conversion for the SSD is $E = 4.98N + 40$ eV, where N is the channel corresponding to the spectral line peak obtained by fitting gaussians to SSD PHA data. For this final report, we adopt quantum efficiencies for the FPCs as communicated by the MST on 1998 June 22 (see 'Quantum Efficiency' under `http://hea-www.harvard.edu/MST/simul/xrcf/HXDS/`). In addition, we employ aperture areas and mesh corrections, provided by MST private communications and interim reports.

For monochromator energy settings above about 0.4 keV, the moderate spectral resolution of an FPC is sufficient to separate spectral orders. However, below ≈ 0.4 keV (HIREFS SB and SA gratings), the PHA spectra of adjacent orders overlap so much that the XSPEC fitting engine cannot reliably distinguish individual orders. Similar difficulties arise, again with the HIREFS, when orders overlap with the scattered W-M$\alpha_{1,2}$ line at 1.775 keV. *When two lines are unresolved, we combine them into a single line for modeling purposes, thereby minimizing the formal fitting error at the expense of obtaining the flux in the individual features.* For either monochromator, the continuum flux is negligible. Besides the x-ray lines themselves, the FPC's argon–methane gas mixture (P10) effects an escape peak, ≈ 2.95 keV below each spectral 'line'. In the spectral analysis, then, we model each escape peak as a separate line, at known energy, and add the rates of the line and its corresponding escape peak to obtain the total modeled count rate in the 'line'.

We use the detector-software estimate of the dead time, which is included in the PHA spectral data files. By time-correlating aperture stage settings with measurement start times, we automatically determine the selected aperture for each measurement.

2.2.3 Raw data

All data used in the analysis comes from the Mission Support Team (MST) mirror site. The MST document "XRCF Phase 1 Testing: Preliminary Results", Chapter 16, discusses the locations and formats of the raw data. Raw data include separate PHA files for each detector, for each measurement, and for each iteration; and they include sum files for each detector and each measurement. Here, an iteration denotes an exposure of fixed duration, short relative to the total measurement time. Typically, individual exposures ranged from 20 s to 90 s, depending upon measurement type and the focal-plane instrument. An HXDS-defined `runid` uniquely identifies each measurement. Owing to restarts of aborted measurements, there can be more than one `runid` associated with a given CMDB-identified measurement (`trwid`). In addition to these data, the analysis requires ancillary data, such as the MST-archived source parameter logs (`xsslog`) and detector stage positions (`stglog`, from which detector apertures are determined). In order to time-correlate data and ancillary data, we employ the IRIG time stamps included in each data and log file.

2.3 Data analysis procedures

In the reduction and analysis of the data, the major stages, in chronological order, are these:

1. Identify and accumulate raw and ancillary data; then condense these to a manageable state for each (monochromator) measurement (§ 2.3.1).

2. Determine the spectral content of these data, using model *jmkmod* within the XSPEC spectral-analysis package (§ 2.3.2).

3. Separately determine the spatial content through fitting physical models of the monochromators to results of spectral fits to beam uniformity (BU) measurements (§ 3).

4. Convolve results of (3) with (2) to define the flux incident on individual HRMA shell quadrants (§ 2.3.3).

2.3.1 Data acquisition and preprocessing

Data acquisition and preprocessing is the same as for the preliminary report. We process data from the MST mirror site as follows:

1. Identify monochromator measurements by searching (parsing) detector 'sumfiles'.

2. Accumulate a list of `runids`, `trwids`, and dates data were taken. The date identifies the data-file and log-file locations on the mirror site.

3. Correlate PHA data files to monochromator energy settings, using `xsslog` files and IRIG time stamps.

4. Link the data files on the mirror site to a pre-defined local disk area.

5. Create a bi-spectrogram from the PHA data files — pulse-height channel versus iteration number — in QDP (Quick and Dandy Plotter) text format and in FITS (Flexible Image Transport System) image format.

6. Co-add data in appropriate PHA data files to create a single PHA file for each detector, measurement, and energy, omitting data obtained during monochromator translations or mini-scans. The monochromator control computer records the IRIG time whenever a new energy is requested through software. To avoid periods of monochromator translations and mini-scans, we ignore PHA data acquired within ±35 seconds of this time. We visually inspect each bi-spectrogram to confirm filtering of undesired data. The resulting PHA files have the same format as the original ones, the `liveTime` being the accumulated time for the sequence of original files.

7. Create XSPEC-readable FITS files from the filtered, co-added PHA files, using the MST script `pha2xspec-fits`.

8. Place files for each `runid` in a separate subdirectory, named by `trwid`. Contents include (*a*) co-added ASCII PHA data files and corresponding FITS files, (*b*) sumfiles; (*c*) bi-spectrograms, (*d*) ASCII files containing mapping of (original) PHA files to IRIG times and source energy settings. Remove links to original PHA files.

xsslogs Correlating PHA data files to monochromator energy settings requires information contained in the (rdb-formatted) `xsslog` files. For the DCM, the relevant `xsslog` fields are `DCM.date` and `XB6HDCT1RT`, the execution time of the DCM energy-setting command, and the resulting Turret-1 position in motor steps, respectively. Equation 1 gives the fitting function for the crystal grazing angle θ (radians), in terms of the Turret-1 position s (motor steps):

$$\theta(s) = (\frac{\pi}{180^\circ})[0.31615^\circ - \frac{(s - s_i)}{r_i}] \ , \tag{1}$$

with s_i (steps) the Turret-1 offset and r_i (steps/°) its conversion factor, for crystal i. Then, for crystal grazing angle θ (Eq. 1), Equation 2 gives the corresponding Bragg energy:

$$E(\theta) = \frac{(12.3984 \text{ keV Å})}{2 d_i \sin\theta} \ , \tag{2}$$

with d_i the lattice spacing of crystal i. Prior to 1997 February 17, the yaw value for the DCM was 0.3333°; thereafter, it was 0.31615° (as used in equation 1). In the preliminary report, we used the value 0.3333° throughout. Therefore, the new results quote Bragg energies which differ by a few eV from those in the Preliminary Report. Table 3 lists the lattice spacing d_i and fitting parameters r_i and s_i, for each crystal employed in the calibration.

Table 3: Fitting parameters for the DCM.

Crystal plane	Lattice d_i (Å)	Offset s_i (steps)	Conversion r_i (steps/°)
TAP 001	12.8784	7820115.0	25538.819
Ge 111	3.266434	4160079.0	25386.677
aSi 400	1.357755	2331545.0	25384.629

For further analysis (§ 2.5) and bookkeeping, we also extract the RAS7 (North) beam current and voltage, and the Turret-2 rotation setting (`XB6VR1HIGH`, `XB6CR1BEAM`, and `XB6HDCT2RT`, respectively) from the `xsslog` files. For correct determination of the DCM crystal selection and energy setting, we use the Turret-1 setting, rather than any other `xsslog` entry.

For the HIREFS, the relevant `xsslog` fields are `HIREFS.date` and `XB6HHRWLEN`, the execution time of the HIREFS energy-setting command and the resulting HIREFS wavelength (in Å), respectively. In addition, we record the RAS14 (South) beam current and voltage, and HIREFS grating selection (`XB6VR2HIGH`, `XB6CR2BEAM`, and `XB6QHRBAND`) for inclusion in the data products.

The `xsslog`s are invalid for HIREFS measurements made on Februrary 5–7 (CMDB Series E). For this time interval, we obtain information about the HIREFS from log-files generated by the HIREFS control computer, located in the source building and independent of the HXDS.

Backgrounds The `trwid` measurement type BG identifies background measurements. During ACIS set-up (measurement type SG), additional background measurements occurred. Typically, each background measurement comprises several iterations. For analysis purposes, we first plotted these to check for anomalies, and then co-added channel-by-channel, and wrote the data as XSPEC-readable FITS files. The PHA file header documents the detector high-voltage setting (in field `voltage_V`), which we tabulated along with the data acquisition time, to facilitate matching backgrounds to measurements.

Beam-uniformity measurements Beam-uniformity (BU) measurements employed FPC_5 as the mapping detector. For a given monochromator configuration (source voltage and beam current, grating or crystal selection, and energy setting), each BU measurement sampled the beam at, typically, 13 positions within the angle subtended by the HRMA's aperture, as well as at the monitoring locations of the SSD_5 and FPC_5. Because the FPC_5 obscures the BND_Hs during the BU measurements, we analyzed only the FPC_5 spectral data. For the BU measurements, we neither co-add PHA spectra nor generate bi-spectrograms. Often, beam uniformity measurements for monochromators occurred during breaks in the HRMA–focal-plane-detector calibration and, thus, have no CMDB-identified `trwid` but only HXDS-defined `runids`. (The BND_Hs purposely did not collect data during these breaks.) Tables 4 through 7 list the `runids` and monochromator energy settings of beam-uniformity measurements used in our analysis (§ 3).

2.3.2 Spectral content

The spectral data reduction fits the model *jmkmod* [13] to the PHA data, within the XSPEC [11] spectral fitting package. The analysis follows closely that described in the preliminary report and further elucidated in reference [14] and proceeds as follows:

- Generate XSPEC command files for fitting the co-added PHA files. The principal spectral features are 'lines' that occur at known energies, corresponding to the selected monochromator setting and multiples thereof. Consequently, 'line' energies are held fixed in the fitting procedure. For 'lines' at energies greater than the argon K-shell ionization (3.2 keV), the model also includes the corresponding escape lines. In addition, for HIREFS measurements at most energies, the model includes the W-M$\alpha_{1,2}$ line (1.775 keV) generated in the RAS anode and scattered within the HIREFS. Due to overlap of this line with either the 1st or 2nd order feature, the W-M$\alpha_{1,2}$ line is

Table 4: DCM beam-uniformity maps using the TAP crystal.

RUNID	Energy	RUNID	Energy	RUNID	Energy	RUNID	Energy
112149	0.950	112176	2.200	112193	2.080	113386	1.530
112150	1.200	112177	2.050	112194	2.110	113387	1.570
112152	1.450	112178	2.065	112195	1.950	113388	1.400
112153	1.700	112179	2.080	112219	2.080	113389	1.950
112154	1.950	112180	2.095	112220	2.110	113391	2.050
112155	2.050	112181	2.110	112221	2.140	113392	2.100
112156	2.065	112182	2.125	112222	2.170	113393	1.700
112166	2.080	112183	2.140	112223	2.200	113394	1.900
112167	2.080	112184	2.155	112224	1.875	113395	1.980
112168	2.095	112185	2.170	112225	1.895	113396	1.800
112169	2.110	112186	2.185	112226	1.855	113463	1.570
112170	2.125	112187	2.200	112250	1.830	113471	1.570
112171	2.140	112188	1.865	112251	1.835	113473	1.900
112172	2.155	112189	1.875	112252	1.830	113475	1.950
112173	2.170	112190	1.885	112259	1.840	113477	1.980
112174	2.185	112191	1.895	112260	1.845	113480	2.050
112175	2.185	112192	1.905	112261	1.850	113482	2.100

Table 5: DCM beam-uniformity maps using the Ge crystal.

RUNID	Energy	RUNID	Energy	RUNID	Energy	RUNID	Energy
112200	2.670	112214	2.870	112258	3.500	113417	4.900
112201	2.670	112215	2.970	113398	2.230	113419	5.060
112202	2.070	112216	3.000	113399	2.290	113435	2.560
112203	2.170	112217	3.070	113400	2.560	113444	5.250
112204	2.270	112218	3.170	113401	2.190	113446	5.650
112205	2.370	112253	2.700	113403	2.260	113448	6.300
112210	2.470	112254	2.725	113405	2.350	113450	9.000
112211	2.500	112255	2.750	113407	3.500	113457	2.560
112212	2.570	112256	2.775	113415	4.510	113459	2.190
112213	2.770	112257	2.800				

Table 6: HIREFS beam-uniformity maps using the SA grating.

RUNID	Energy	RUNID	Energy	RUNID	Energy	RUNID	Energy
113282	0.523	113296	0.785	113315	1.177	113321	0.785
113285	0.539	113311	1.046	113319	0.625	113322	0.523
113292	0.625	113313	1.078	113320	0.640	113323	0.539
113294	0.640						

Table 7: HIREFS beam-uniformity maps using the SX grating.

RUNID	Energy	RUNID	Energy	RUNID	Energy	RUNID	Energy
113336	1.569	113341	1.616	113348	1.280	113354	1.546
113338	1.569	113344	1.962	113350	1.876	113357	1.384
113340	1.616	113346	1.250	113352	1.919	113359	1.775

not included in fits to HIREFS measurements at energies $1.487 \leq E \leq 2.0$ keV and $0.8 \leq E < 0.96$ keV. The command files also identify a corresponding background, which we subtract using the 'back' command within XSPEC. Because the data show negligible continuum, the model includes no continuum component.

- Fit *jmkmod* in XSPEC to spectra with line energies fixed. Free parameters are gain (`gain`, μ, relating line energy to channel number), Polya width parameter (`polyah`, h, described in reference [15]), shelf-norm parameter (`shelfnm`, δ, for the partial-charge-collection shelf in channels below each 'line'), line strengths (`E_norm`, relative norms), and overall model norm (`norm`). We set the Fano factor (`fano`) to 0.2, turn off *jmkmod* continuum parameters (`contin`= 0), and employ no additional XSPEC model component. To obtain the optimum fit, we use the χ^2 minimization criterion.

- Archive details of the fit (XSPEC log file) and a QDP-formatted figure, displaying data and model fit in one panel and the fit residuals in a second panel, as generated for each PHA file analyzed. We place these, along with the XSPEC command files, in the same directories as the corresponding PHA files, bi-spectrograms, etc. (§ 2.3.1).

- Convert counts s^{-1} (from XSPEC fit with XSPEC-generated errors) to photons s^{-1} cm^{-2} at the HRMA node, at the respective BND positions, using aperture areas correlated to detector stage positions (from `stglogs`), quantum efficiencies described previously, and distances from source to detectors and HRMA (from http://wwwastro.msfc.nasa.gov/xray/xraycal/distance.htm).

- Place resulting flux (with errors) for all fitted spectral features, along with line energies, identifying parameters (`runid`, `trwid`, IRIG times, background `trwid`), model free parameters (with errors), fit statistics, Region Of Interest (ROI) used in fit (typically channels 21 to 399, up to 499 for DCM multi-energy measurements extending to $E > 8$ keV), integration times, y and z stage positions, aperture areas, etc., into rdb-format table files. (See example of a tab-delimited rdb table in § 2.5.)

2.3.3 Convolution of spectral and spatial information

As the final step, we combine the spectral content for each measurement with the spatial information from the beam-uniformity models as described in § 3. At this stage, the count rates detected in the four BND_Hs and the FPC_5 have already been converted to background-subtracted flux (photons s^{-1} cm^{-2}) corrected for detector quantum efficiencies. Thus, ideally, the flux at the 4 HRMA BNDs, predicted using the spatial model, can simply be scaled to the observed BND_H fluxes for a given measurement to obtain an overall normalization factor and then the model-predicted flux in the HRMA quadrant-shells computed using this factor. In practice, however, we must introduce an additional fit parameter to account for (a) detuning of the DCM or (b) change of alignment of the HIREFS between equipment change-outs. In § 3, we describe the convolution procedure.

2.4 Spectral analysis results

We identified 33895 DCM and 8805 HIREFS iterations corresponding, respectively, to 578 and 489 independent `runids` and to 151 and 53 discrete source energy settings. From these, we obtained 1155 DCM and 486 HIREFS co-added spectra for each of the 5 FPC BNDs (there are more co-added spectra than there are runids because of energy scans). Thus far, we have analyzed all data with the exception of DCM data taken during CMDB D-series and HIREFS data taken during CMDB E-series. As it is impractical to describe each measurement individually, we describe trends in the data and in the fitting statistics and discuss their influence on the overall fidelity of the results.

2.4.1 Fitting trends

The principal task is to determine the flux from the various spectral features incident upon each BND and to minimize the uncertainty in these quantities. Toward this end, we employ the χ^2-minimization criterion to determine the best-fit parameters, estimate errors, and to provide a statistical measure of the goodness of fit. In the absence of systematic errors, purely statistical uncertainties would result in model fits with these well-defined statistical properties:

Parameter uncertainty. The fractional uncertainty in the estimated flux, $\delta F/F \sim \sqrt{N}/N$ where N is the number of counts detected.

χ^2 value. The mean value of $\chi^2 \sim \nu$ where ν is the number of degrees of freedom (with standard deviation, $\sigma_{\chi^2} \sim \sqrt{2\nu}$).

Parameter mean. The model-predicted rate equals the observed rate.

The following addresses these points before discussing possible sources of systematic errors.

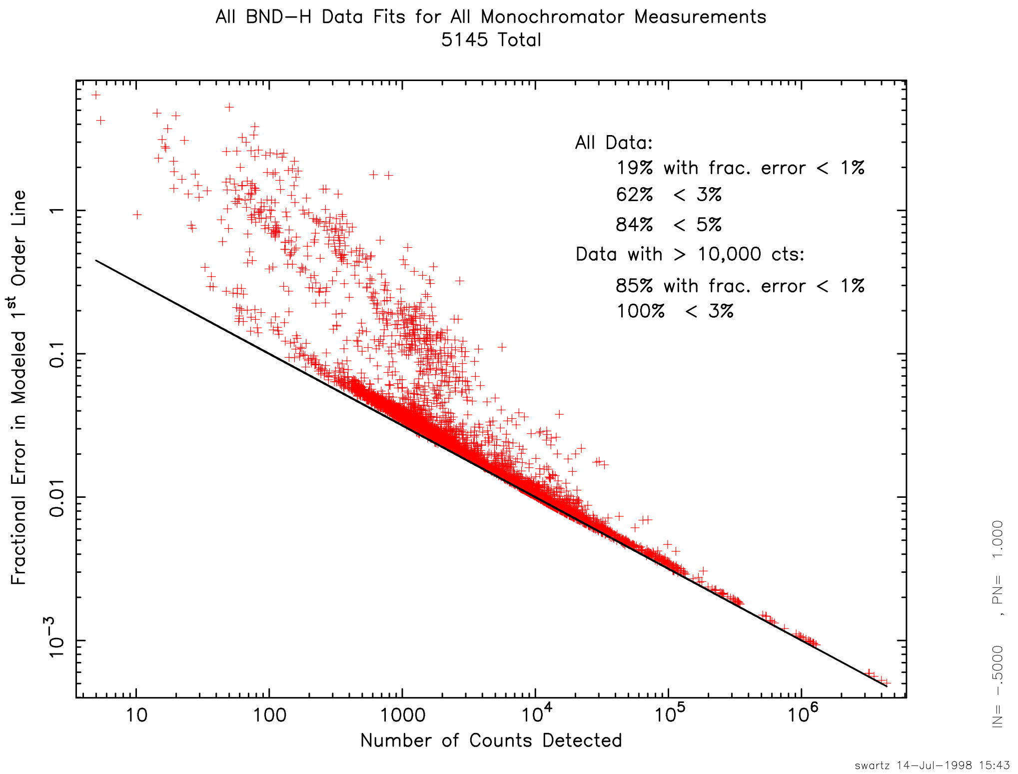

Figure 4: Results of spectral fits of all monochromator measurements, displaying fractional error in the modeled first-order 'line' flux against the number of counts detected. Inset displays fractions of those measurements lying within $C = \sqrt{N}(\delta F/F)$, where C is a constant. The solid curve in the main figure corresponds to $C = 1$.

Parameter uncertainty. For the majority of the measurements, determination of the flux to reasonable precision is possible. Figure 4 displays the fractional error in the modeled flux of the first-order 'line' ($\delta F/F$) versus the number of counts detected in this feature (N), for all detectors and all monochromator measurements. Of all measurements, 84% have fractional statistical errors less than 5%. For measurements with > 10000 counts, 85% have fractional errors less than 1% and none have fractional errors greater than 3%. Measurements with low number of counts tend toward larger fractional errors, primarily because those measurements with $\delta F/F \gtrsim 0.3$ are low-energy HIREFS measurements with severely overlapping spectral orders and low first-order flux. The solid curve in Figure 4 traces the fractional error expected from purely statistical uncertainties, $\delta F/F = \sqrt{N}/N$, as applies to widely separated spectral orders. The vast majority of the points lie near this line, as shown in the inset which displays the fraction of the measurements which lie within $C = \sqrt{N}(\delta F/F)$ where C is a constant, logarithmically binned.

χ^2 value. The value of χ^2 provides a statistical measure of the agreement between the data and the model for a chosen set of model parameters, with smaller values of χ^2 indicating closer agreement. Figure 5 displays the values of χ^2 as a function of the number of counts detected, for all detectors and all monochromator measurements. Depending upon the number of spectral features, the number of degrees of freedom (ν) ranges from 369 to 375, for the typical ROI of 379 PHA channels. For large values of ν, we would expect χ^2 to be distributed normally with mean ν and standard deviation $\sqrt{2\nu}$. Inspection of Figure 5 shows that the value of χ^2 begins to deviate from the expected behavior for $N \gtrsim 10^4$ counts, indicating an average systematic error of order $N^{-1/2} \sim 1\%$.

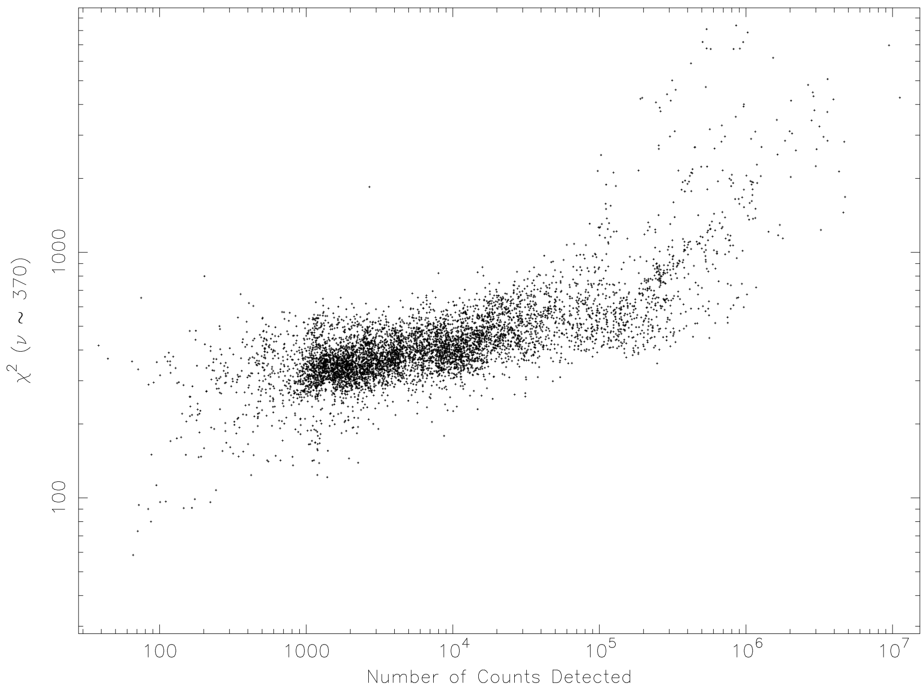

Figure 5: Value of χ^2 for all spectral fits to monochromator measurements against total counts detected in the region of interest (typically 379 PHA channels).

Parameter mean. The model under-predicts the total flux at low total counts in the spectrum. As shown in Figure 6, the deviation of the model-predicted rate from the observed rate, over the ROI, increases as the number of counts decreases. This count-dependent bias may result from the assumption in XSPEC that the error equals the square-root of the observed number of counts in the bin ([16]) and/or from use of an incorrect model. As the curve shows, any systematic effect which becomes more important as the number of counts decreases, such as the source-to-background flux ratio, may contribute to the trend shown. Figure 7 shows that the deviation of the model-predicted rate from the observed rate is greatest for the lowest count *rates* as well.

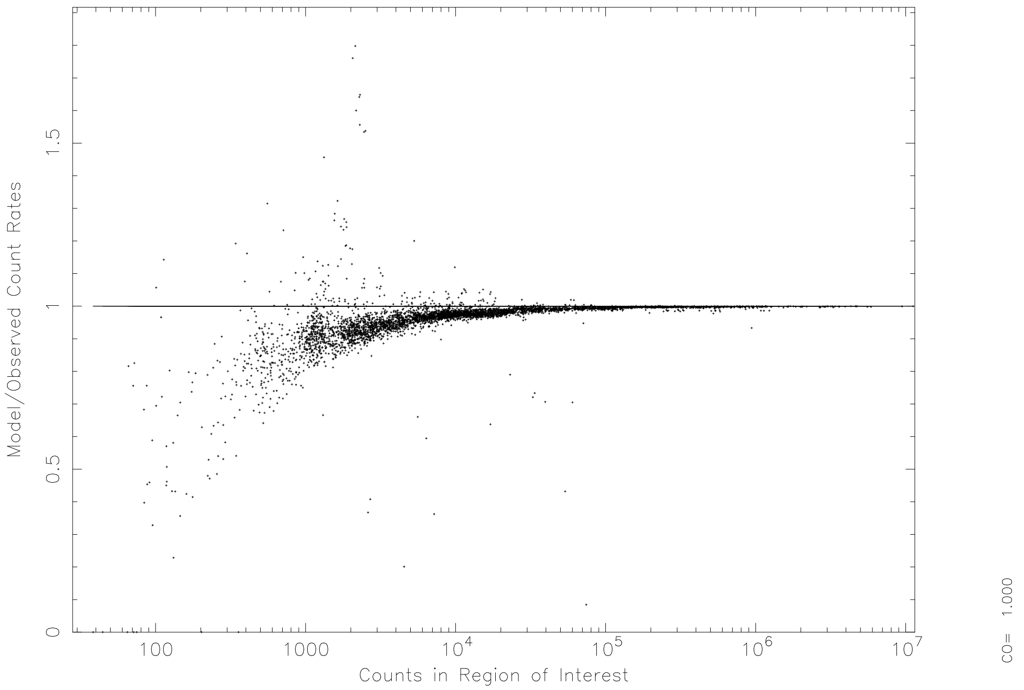

Figure 6: Ratio of the model predicted count rate to the detected count rate, over the entire ROI, as a function of the total number of counts detected. The plot includes results for all 5 FPCs and all monochromator measurements.

Providing further evidence of this trend, Figure 8 displays the variation of specific flux (photons s^{-1} cm^{-2} mA^{-1}) with number of counts detected in the line, for the 4 BND_H counters, for measurements made using the HIREFS-SX grating set to 1.487 keV. We use these data for illustration due to the relatively large number of measurements made at this energy, the large range in the number of counts detected, and the fact that a single line component is sufficient to estimate the flux in the feature. Note the different behavior in the different detectors, attributable to spatial variations in the beam. (We have already corrected the specific flux for quantum efficiency, aperture area, etc.) In this example, the use of the χ^2 statistic systematically under-predicts the flux in the spectral features by X% for Y counts in the line. For two of these measurements, summarized in Table 8, the predicted count rates in the line differ substantially using the χ^2 figure of merit, either with the background subtracted or with it treated as an added component with parameters fixed. However, count rates predicted using the C-statistic are in better agreement with each other and are systematically higher than those predicted using the χ^2 statistic by $\approx 6\%$ and $\approx 14\%$. This is respectively consistent with the data in Figure 6, for measurements with comparable total counts.

The increase in fractional error at low number of counts, the deviation of the value of χ^2 from the expected value at high counts, and the failure of the model predicted rate to coincide with the observed rate at low counts and low counting rates may result in part from the use of the χ^2 figure-of-merit. However, systematic effects also contribute: Certainly, the largest deviations shown in Figure 4 are for

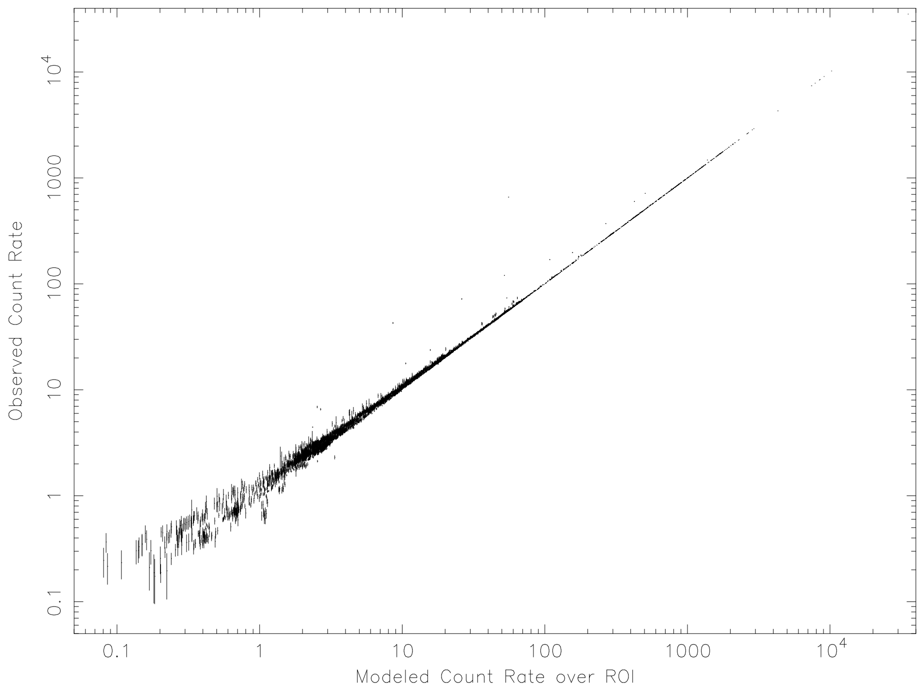

Figure 7: Comparison of measured to modeled count rates for monochromator data. Observed count rate compared to the model predicted count rate for all 5 FPCs and all monochromator measurements. Compare to Figure 6.

Table 8: Comparison of results of fitting (cts s^{-1} mA/10^{-2}) using χ^2 and C statistics.

trwid	cts in line	χ^2 (subtracted BG)	χ^2 (fitted BG)	C-statistic
G-LHS-EA-9.001	7639	4.023 ± 0.095	4.059 ± 0.090	4.305 ± 0.092
G-IHI-EA-2.077	1993	3.591 ± 0.164	3.672 ± 0.160	4.234 ± 0.169

those measurements made at low energy, where the first order line is weak relative to higher orders and severe line overlap occurs. Two classes of systematic effects may contribute — inappropriate source modeling and poorly constrained detector parameters.

2.4.2 Source-specific parameters

The source model parameters in *jmkmod* are the line norms (cts s^{-1}). Although, for some measurements, the spectrum was filtered upon leaving the monochromator, the monochromators generate negligible continuum and thus require no continuum nor filter-specfic source parameters for fitting the data. Hence, the source model includes the first-order line at the energy of the monochromator energy setting, (possibly) higher spectral orders, escape peaks, and (in some cases) scattered lines from the RAS W anode.

When the detector does not spectrally resolve the lines, including both lines in the model results in an unrealistically high uncertainty in the flux of each line, because an increase in the flux of one component compensates for a decrease in flux of the other. This overlap is most severe in HIREFS spectra near the lines from the tungsten anode, scatttered by the grating. Ideally, we could use the (higher resolution) SSD_5 detector to determine relative line strengths, then hold the relative strengths fixed in fitting

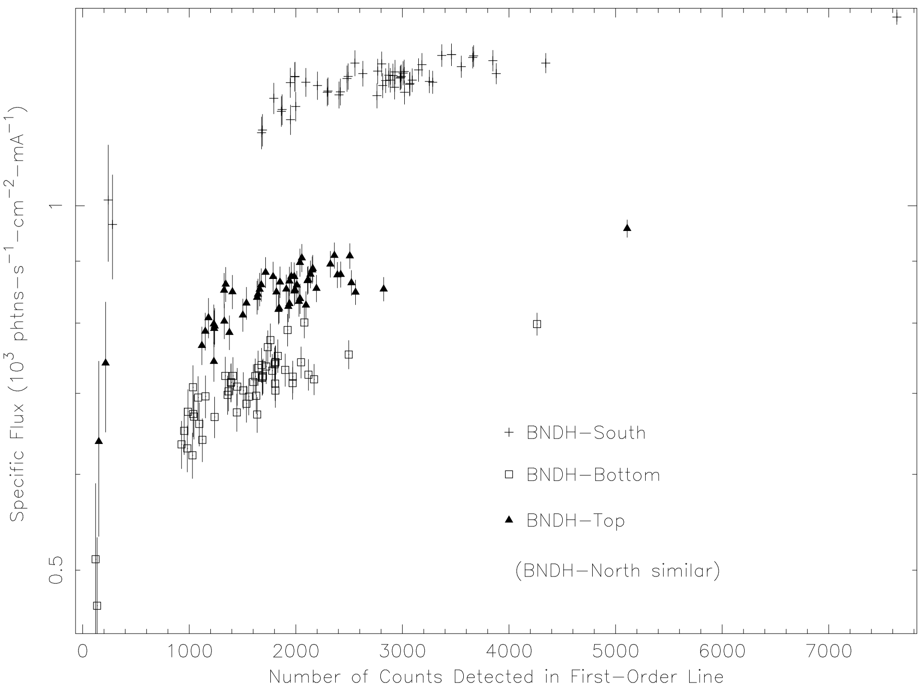

Figure 8: Modeled HIREFS 1.487-keV specific flux (flux per unit RAS beam current) versus number of counts detected in the line. Data are for all BND_Hs measurements made with HIREFS SX grating, tuned to 1.487 keV. The trend of increasing specific flux with increasing number of counts detected is consistent with the trend seen for all data (*cf.* Figure 6). This plot includes only counts in the single spectral feature. The model incorporates only the single line at the HIREFS energy setting. (FPC_5 data show a similar trend, although the number of counts is much larger due to its proximity to the source.)

FPC data. Unfortunately, the beam spatial characteristics of the scattered lines differ from those of the (nearby in energy) monochromator-selected spectral lines; furthermore, these characteristics change with monochromator energy setting. In addition, the beam spatial properties are poorly determined far from the FOA, where the SSD_5 and FPC_5 are located; thus, even at a given energy, this procedure is suceptible to errors.

The approach we adopt here is to fit such unresolved features with a single line component at the expense of determining the flux in the individual lines. Table 9 lists the HIREFS energies for which we model W-M$\alpha_{1,2}$ (1.775 keV) lines overlaping with the first- and higher-order lines as a single component. Because the W-Mβ (1.835 keV) line always strongly overlaps with M$\alpha_{1,2}$, we never treat it separately. We do not include the Mζ_1 (1.384 keV) line in our models because there is no spectrum in our dataset for which we can unequivically isolate this line from other features: At low energy settings, higher orders and M$\alpha_{1,2}$ appear near the location of Mζ_1; at higher energy settings, Mζ_1 appears as a low energy shoulder on the first-order line. However, fits to high-flux measurements indicate that this line is present at significant confidence. Future work will attempt to include Mζ_1 as an additional model component. For low-flux (particularly BND_H) spectra, we might best accomplish this by fixing line-strength ratios, as described above, to values determined from similar measurements at higher count rates. Below, we show that the unmodeled Mζ_1 line accounts for an increase in the value of the shelf normalization parameter, in fits to HIREFS spectra at energy settings $E \gtrsim 1.5$ keV. In fact, Mζ_1 accounts for as much as 4% of the modeled flux in the first-order line near $E \approx 1.5$ keV.

Treatment of the detector background is another possible source of systematic errors associated with

Table 9: HIREFS spectral orders overlapping with W-M$\alpha_{1,2}$ line.

Energy-setting range	**Orders in fit**	**Order overlapping W M$\alpha_{1,2}$**
1.487–2.000 keV	1	1$^{\mathrm{st}}$
0.826–0.960 keV	2	2$^{\mathrm{nd}}$
0.600–0.705 keV	3	3$^{\mathrm{rd}}$

modeling. In Section 2.3.1, we describe the identification and construction of background files appropriate for each measurement. The previous example (*cf.* Table 8) shows that there is no significant difference between subtracting the background or modeling the background as a separate component (with fixed parameters) in XSPEC. Therefore, the background treatment should not affect the flux determination, unless the background used is inappropriate to the data. There is no indication that this is the case.

2.4.3 Detector parameters

Extracting the source spectrum from the measured pulse-height distribution requires deconvolution of the detector response function. By design, however, *jmkmod* includes the detector response function in the model with detector-specific adjustable parameters. The rational for this is that several detector properties are either uncertain or are purposely adjusted between measurements for optimal performance during calibration. (As the term is used here, the detector response function does not include the absolute quantum efficiency. Rather, it applies this multiplicative factor in the final step, along with aperture area and distance scale factors, to convert detected counts s^{-1} to incident photons s^{-1} cm^{-2}.) The variable detector-specific parameters are the gain (μ, channels per ion pair), Polya width parameter (h, dimensionless), and flat-shelf normalization (δ, dimensionless).

Gain. The gain parameter (μ) relates the mean channel ($\langle q\rangle$) corresponding to the distribution peak, to the incident photon energy (E), through $\langle q\rangle = (\mu/w)E$, where $w = 0.028$ keV/pair is the work per ion pair for the FPC's argon gas. There is no evidence for a correlation between μ and the computed flux in spectral features. However, there are variations in FPC detector gain observed, some of which we have not fully analyzed. As expected, the gain varies exponentially with detector high-voltage setting (Figure 9). Between XRCF measurements at different energies, the HXDS operators adjusted the detector voltage to maintain a constant resolution in PHA channels. The gain is also an exponential function of the detector gas temperature. Model fits show the fitted gain parameter varies significantly for FPC_5, whose temperature can vary by several degrees Celsius over a period of hours. Conversely, the BND_Hs are much more thermally stable, typically varying periodically by $\sim 0.1°$C on ~ 1 day timescales, effecting changes in μ of $\sim 1\%$.

Figure 10 shows the gain variation with source energy setting, for the 4 BND_Hs, when the DCM monochromator was used and the detector high voltage was set to 1586 V. Note the decrease in gain at decreasing energies, in the range 1–2 keV. This gain shift does not result from erroneous monochromator energy settings: We confirmed the first-order line energies from the corresponding SSD spectra (with known gain). Furthermore, there is no correlation of these gain variations with temperature, nor time the measurements were made. A possible cause is a bias in the fitting related to the shift of the line peak to increasingly lower channels as the energy decreases; but this is not necessarily a zero-point offset, which should be evident at all energies. For these measurements, the first-order spectral line appears in channels as low as $q \approx 40$ at $E \approx 1$ keV.

Figure 10 shows another gain change, observed at energies above $E \approx 4$ keV, which correlates to the time the measurements were taken. The model gain changes by about 2% between those DCM measurements performed in Series G (20–25 March) and those in Series H (18–21 April, 1997). A change in detector high voltage of $\Delta V \approx 2$ V at $V \approx 1586$ V could produce the observed change in μ; however, there is no independent evidence for a change in the actual *versus* recorded voltages during this time period.

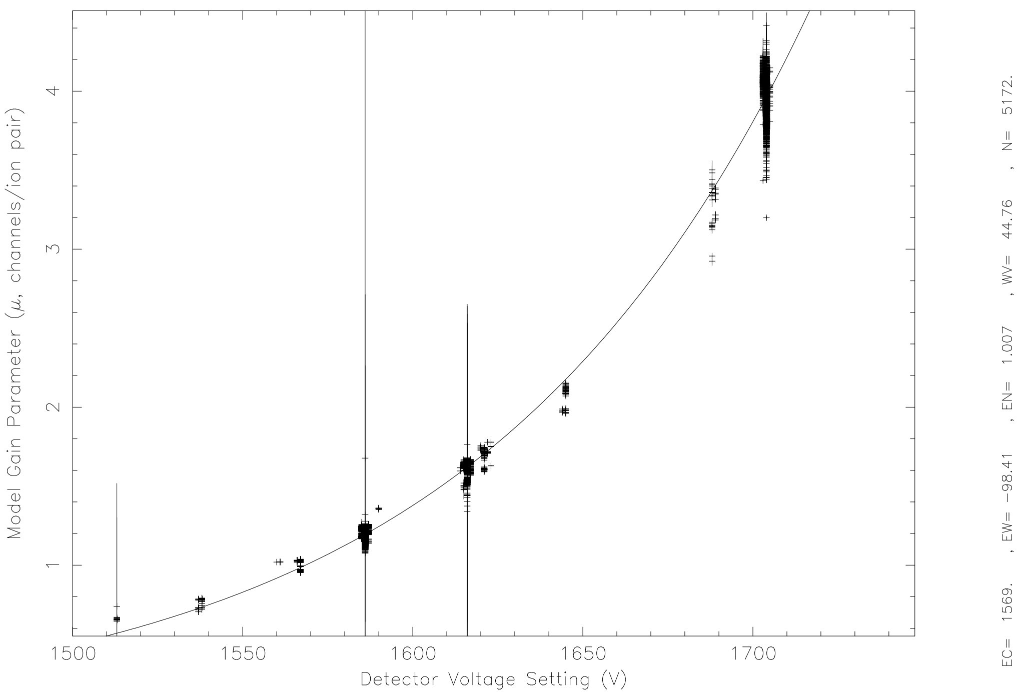

Figure 9: Model-predicted FPC gain parameter (μ) vesus detector voltage setting (`voltage_V` in the PHA files). The voltage was adjusted between measurements to maintain the same resolution in PHA channels for the principal spectral feature (first-order line). The dependence is exponential.

Polya width. The Polya parameter (h) controls the width of the modeled pulse-height distribution. Physically, this distribution is proportional to the combination of the statistical distribution of secondary ionizations created by a primary photo-electron — the variance of this distribution being described by the Fano factor (F) — and the statistical distribution of avalanche electrons produced in Townsend discharge as the secondary electrons approach the anode wire — characterized by the width parameter h and the gas gain. Thus, both F and h affect the model line width. We choose to hold $F = 0.2$ and allow only h to vary in our fits. At low energies, the data poorly constrain h, due to the presence of multiple, overlapping spectral orders in HIREFS spectra. There is a slight decrease in h (Figure 11) with increasing monochromator energy setting — $h \approx 1.3$ at 3 keV dropping to ≈ 1.1 at 9 keV. As expected, this variation is detector-dependent. At the highest count rates (particularly, for Series I DCM measurements), the fit to the *shape* of the FPC spectra is rather poor, as seen in the fit residuals, indicating perhaps another shape parameter such as the Fano factor (F) is not optimized in our models. However, the observed rates and the model-predicted rates, over the range of channels included in the fits, agree to better than 0.4% for measurements with count rates > 1000 cts s^{-1}. In fact, there is no observed correlation between computed flux in spectral features and h. Because the value of h should depend upon energy, a single value for this parameter is inappropriate for spectra containing multiple lines, particularly when they are well separated in energy.

Shelf normalization. The shelf normalization parameter (δ) characterizes the flat region of the PHA spectrum observed in channels below that of the line peak. The value of δ roughly corresponds to the fractional contribution of the shelf to the total flux in the line. Physically, this shelf results from partial charge collection, due mainly to drift losses through the detector window. Consistent with this interpretation, δ is highest at the lowest energies, because lower energy photons are preferentially

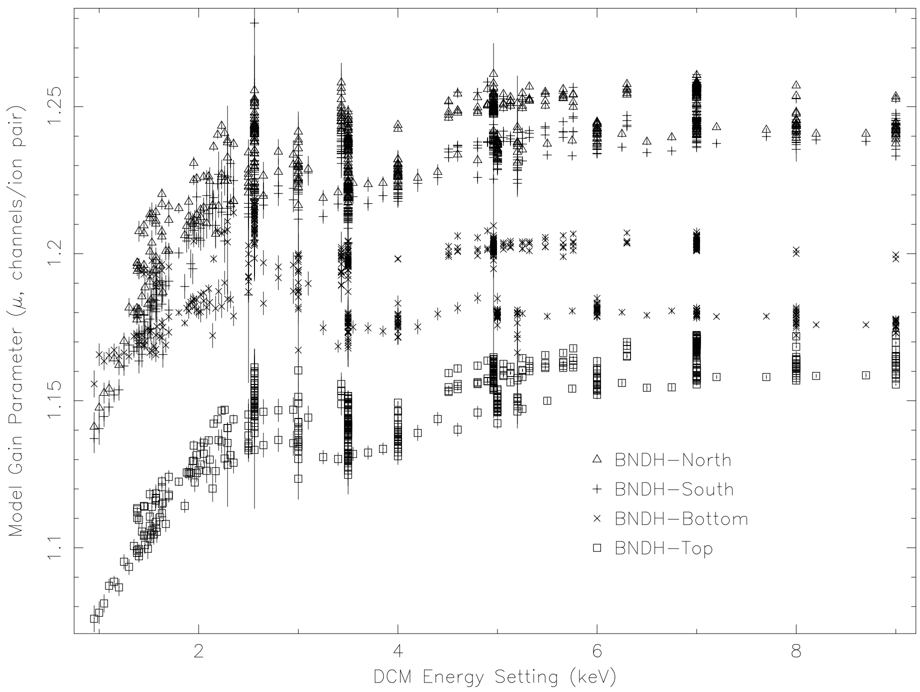

Figure 10: Model-predicted FPC gain parameter (μ) versus monochromator energy setting. The plot includes all BND_H observations taken with detector voltage set to $V = 1586 \pm 1$. FPC_5 underwent much larger thermal fluctuations during calibration than did the BND_Hs, producing a much greater spread in μ. Note the decrease in gain with decreasing energy in the range $E \approx$ 1–2 keV and the systematic change in gain, most clearly seen above $E \approx$ 3–4 keV, which correlates with the time the measurements were made. (See discussion in the text.)

absorbed nearer the entrance window. Below $E \approx 1.5$ keV, δ decreases approximately exponentially with E; at higher energies, δ is nearly flat (Figure 12). Values of δ range from ≈ 0.1 at the lowest monochromator energy setting (0.277 keV) to ≈ 0.01 at 1.5 keV, decreasing asymptotically to ≈ 0.008 at 9 keV.

For HIREFS spectra in the range 1.5–2.0 keV (the maximum energy setting for the HIREFS), the fits show δ increasing with energy: This nonphysical behavior is an artifact of not including the W-Mζ_1 line (1.384 keV) in the model. Figure 13 displays how this line appears as a broad bump (apparent maximum at channel 191) on the shoulder of the M$\alpha_{1,2}$ complex at 1.775 keV (maximum at channel 245). Over the range of energies illustrated, the Mζ_1 line gradually becomes more discernible as the source energy setting increases: This increases the *apparent* contribution of the shelf to the modeled line flux. Note also that, above $E \approx 1.8$ keV, the flux decreases rapidly and the peak channel does not change as the energy is increased. This indicates the combined presence of the M$\alpha_{1,2}$ feature and the rapidly decreasing efficiency of the SX grating — i.e., *only* the scattering line contributes to the flux at high energies.

The shelf normalization parameter can significantly affect the computed flux in spectral features. Formally, the contribution of δ to the line flux (line norm or global norm in *jmkmod* parlance) is a rather complicated function [10]; however, the value of δ corresponds roughly to the fractional contribution of the shelf to the overall flux in the line. Thus, the shelf contributes no more than $\approx 1\%$ to the total counts in DCM spectra above ≈ 2 keV and $\approx 3\%$ at 1 keV in HIREFS spectra, consistent with $\delta \approx 0.01$ and ≈ 0.03, respectively. At lower energies, the shelf and first-order features are strongly blended, precluding this separation. As with the Polya width parameter (h), applying a single value for the shelf

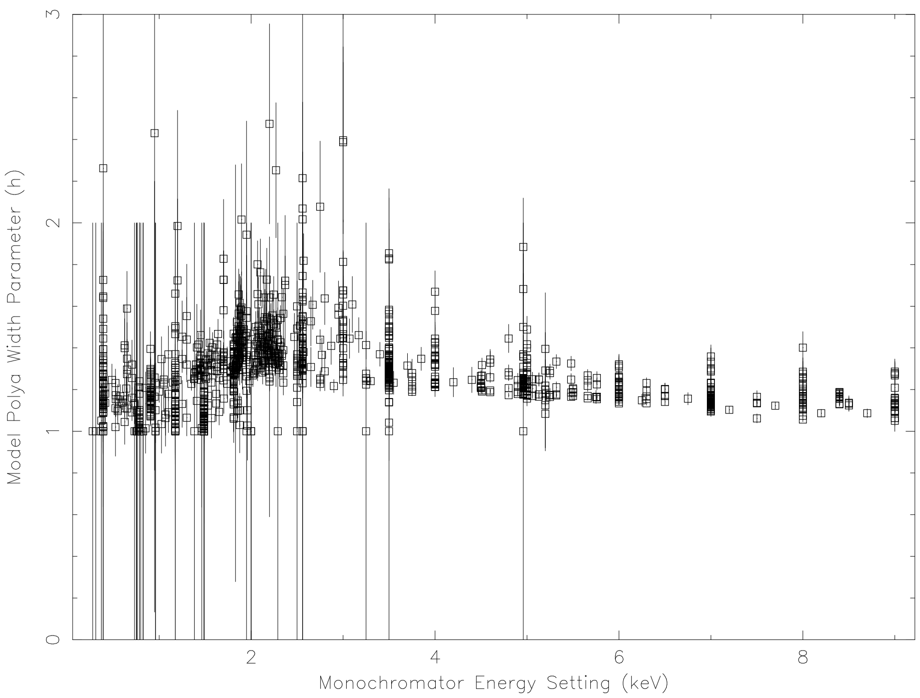

Figure 11: Model predicted FPC Polya width parameter (h) versus monochromator energy setting. The plot includes parameter values from the BND_H-top detector for all monochromator measurements. Note the slight decrease with increasing energy. The parameters μ and F (Fano factor) also contribute to the width of the modeled PHA distribution; therefore, the modeled variation in h may depend on the adopted value $F = 0.2$.

normalization parameter (δ), to spectra containing several widely spaced lines, is inappropriate.

2.5 Data products

The primary data products from spectral analysis of BND data for monochromators are rdb-formatted tables of the spectral content of each measurement, for each detector. These tables are identical in format to those produced for the Preliminary Calibration Report, except for the addition of 3 comment lines at the beginning of the table, which identify the time the table was created.

2.5.1 Intermediate products

We have generated several intermediate products for visualizing and understanding the data-analysis process, for estimating limitations and accuracy, and to facilitate reproducing the results:

- Bi-spectrograms (QDP (ASCII), FITS image formats);
- Co-added PHA spectra (rdb, XSPEC-readable FITS) and "mapping" (ASCII) of raw data to monochromator energy settings;
- XSPEC-generated plot files (QDP (ASCII)) showing spectral data and model fits versus channel number;
- XSPEC-generated "log" files (ASCII), containing *jmkmod* fit parameters and their errors, included PHA channels, observed and model count rates over these channels, associated background, and the χ^2 fit statistic; and

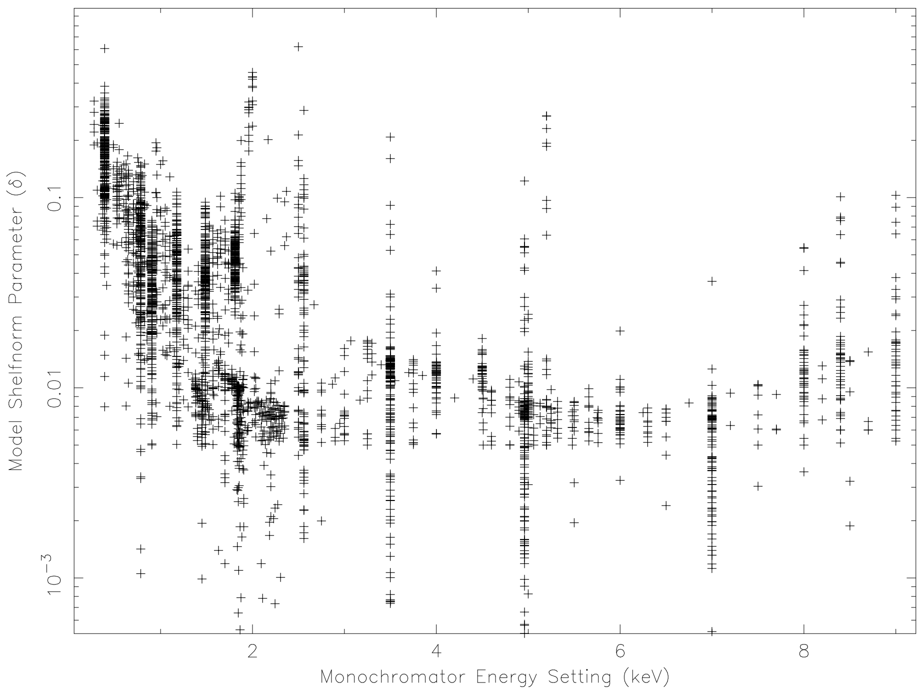

Figure 12: Model predicted shelf normalization parameter (δ) vesus monochromator energy setting. The plot includes parameter values from all 5 FPC BNDs and all monochromator measurements. The decrease with increasing energy at $E \lesssim 2$ keV is roughly exponential; the slow decrease at higher energies is roughly linear.

- Beam-uniformity analysis intermediate products, per § 3.

2.5.2 rdb tables

The primary spectral analysis data product is a set of rdb-formatted tables. We generated these tables for all calibration measurements, including BU measurements. These data constitute the spectral information which we use in the spatial analysis (§ 3). For each FPC and for each monochromator combination, we generate an rdb table (10 in all), containing the following information:

- Flux at the HRMA node (photons s^{-1} cm^{-2}), *at the XRCF Y, Z position of the particular BND*, with XSPEC-generated errors, for up to 5 lines — 4 spectral orders, plus the W-M$\alpha_{1,2}$ (1.775-keV) line, for most HIREFS measurements; and
- Measurement identifiers (`runid`, `trwid`, IRIG time, etc).

In addition, all tables contain the following ancillary data:

- Monochromator settings — monochromator name, grating or crystal, energy setting, and RAS beam current and high voltage;
- Detector settings — detector name, stage position, high-voltage setting, and aperture area; and
- XSPEC fitted values for the free parameters, with errors and fit statistics.

The following is the header section from an rdb table reporting the results of the spectral modeling of the PHA data. The header briefly describes all data contained in its columns and certain additional

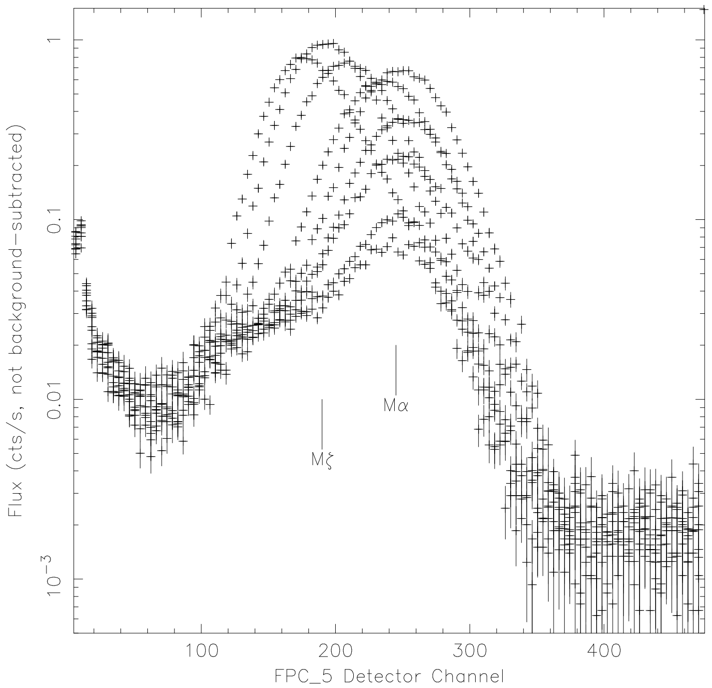

Figure 13: Scattering of the W-Mζ_1 line in the HIREFS. FPC_5 spectra (not background-subtracted) for 9 HIREFS-SX energies, over the range 1.3 to 2 keV, exhibit a weak W-Mζ_1 line (1.383 keV, peak at channel $\approx$ 191). All measurements used the same detector voltage setting and, hence, same model gain. The model fit excludes the Mζ_1 line which thus appears as an increase in the shelf normalization parameter (δ) as the source energy increases. Note also how the first-order-line peak channel reaches a limit at channel $\approx$ 245 accompanied by a sharp decrease in flux above 1.81 keV. Channel 245 corresponds to the location of the W-M$\alpha_{1,2}$ scattering line.

information useful to the data-product user. To facilitate display of the information, we here wrap the last 40 lines of the header, producing 21 2-column lines.

```
#
# date rdb table constructed:  Wed Aug 12 11:23:04 CDT 1998
#
#       COLUMN DEFINITIONS
#runid:          MST runid
#ymd:            yymmdd date
#trwid:          trwid
#irig:           irigStartTime
#srcName:        source name from sumfile
#srcType:        source anode for EIPS
#srcEnergy:      source energy for monochromator
#detector:       Beam Normalization Detector name
#iter:           iteration number (one per monochromator energy setting)
#BG_trwid:       corresponding background trwid
#eline1:         energy of first line fit (keV)
#flux1:          flux in first line fit (phts/s/cm2) at HRMA nodal point
#flux_err1:      error in flux in first line fit
```

```
#eline2:         energy of second line fit (keV)
#flux2:          flux in second line fit (phts/s/cm2) at HRMA nodal point
#flux_err2:      error in flux in second line fit
#eline3:         energy of third line fit (keV)
#flux3:          flux in third line fit (phts/s/cm2) at HRMA nodal point
#flux_err3:      error in flux in third line fit
#eline4:         energy of fourth line fit (keV)
#flux4:          flux in fourth line fit (phts/s/cm2) at HRMA nodal point
#flux_err4:      error in flux in fourth line fit
#eline5:         energy of fifth line fit (keV)
#flux5:          flux in fifth line fit (phts/s/cm2) at HRMA nodal point
#flux_err5:      error in flux in fifth line fit
#aper_area:      area of aperture in use (cm2)
#stage-y:        detector y-axis stage position (um)
#stage-z:        detector z-axis stage position (um)
#ras_i:          monochromator RAS beam current (from xsslog)
#ras_v:          monochromator RAS high voltage (from xsslog)
#grating_crystal:HIREFS grating or DCM crystal selection (from xsslog)
#turret2:        turret 2 rotation for DCM (else=0) (from xsslog)
#chn_lo:         lower channel included in fit
#chn_hi:         upper channel included in fit
#liveTime:       integration time for this iteration
#obs_rate:       count rate within roi
#obs_rate_err:   uncertainty in count rate within roi
#mod_rate:       model predicted count rate within roi
#Chi_sq:         model chi-squared
#nchan:          number of pha bins included in chi-square calculation
#gain:           model gain parameter value
#gain_err:       model gain parameter value error
#shelfnorm:      model shelf norm parameter value
#shelfnorm_err:  model shelf norm parameter value error
#polyah:         model polyah parameter value
#polyah_err:     model polyah parameter value error
#voltage_V:      detector high voltage setting
# ANCILLARY DATA FILES
#Distances:      http://wwwastro.msfc.nasa.gov/xray/xraycal/distance.htm
#Apertures:      see /pool14/swartz/tables/aper.tab
#fpc_qe:         see /pool14/swartz/tables/fpc.qe (from R. Edgar, 980622)
#ssd_qe:         see /pool14/swartz/tables/ssd.qe (data from BESSY)
#mesh_corr:      a mesh correction of 0.9025 is applied to all FPC fluxes
# JMKMOD FIXED PARAMETER VALUES
#fano:          0.20            #bfield:      14500.0
#E_offset:      0.0             #current:         1.0
#ch_off:        0.0             #incline:         0.0
#broad:         0.0             #abswitch:        0.0
#d_gain:        0.0             #phi:           135.4
#contin:        0.0             #theta:          40.2
#E_char:        2.0             #shell:          12.0
#E_width:       0.1             #src1:           35.0
#temper:       15.0             #src2:            6.0
#pressure:    400.0             #src3:            2.0
#argrat:        0.9             #src4:           19.0
#shelfsw:       1.0             #src5:           38.0
#t1norm:        0.0             #src6:           45.0
```

```
#t1par:        0.999     #srcthk1:      0.0
#t2norm:       0.0       #srcthk2:      0.0
#t2par:        1.001     #srcthk3:      2.000e-6
#pulser:       0.0       #srcthk4:      1.065e-4
#numcomp:      8.0       #srcthk5:      5.36
#numfil:       6.0       #srcthk6:      0.0
#pileup:       0.0
#pilepar:      1.0
```

3 Beam uniformity of the XSS monochromators

3.1 Objectives

For reasons described below, the XRCF monochromators produce inherently nonuniform beams. In many cases, the nonuniformity is substantially larger than that of the other XRCF sources. Thus, interpreting the results of these tests requires special care, for the following reasons:

1. The BNDs do not always provide a representative sample of the beam; hence, a simple average of the BND fluxes can lead to a significant error in the mean HRMA flux.
2. The differing energy response of individual HRMA shells results in a bias if the flux is radially nonuniform. Analyses must account for differences in shell reflectance at a given energy if the beam is nonuniform. This is especially important above 2 keV, where changes in the relative contributions of the 4 shells to the total effective area are substantial.
3. In some cases, the detector response depends significantly on incident angle and is, therefore, different for photons from each HRMA shell and azimuth. Clearly, were the beam to illuminate only one spot on the HRMA, then the test would measure the detector response to photons arriving only at the incident angle corresponding to that spot. Therefore, for a significantly nonuniform beam, derivation of the overall QE requires *a priori* assumptions about detector response versus incident angle.
4. Owing to its P-to-H decenter, the HRMA itself exhibits significant azimuthal nonuniformity in geometric aperture. If not accounted for, this nonuniformity results in an additional deviation between the unweighted BND mean and the average flux entering the HRMA.

To begin to address these problems requires adequate characterization of the spatial variations in the x-ray flux. Here, we present results from analysis of the beam characterizations, for each of the two monochromators. We then apply those results to the actual calibration measurements.

3.2 HIREFS monochromator

3.2.1 Description of model

The HIREFS is a complex optical system. (See schematic Figure 3, in Section 2.2.1.) Because it comprises two curved optics and a diffractive element, its behavior is as complicated as that of the HRMA–grating combinations. Our approach to characterizing the HIREFS beam is to construct a physical model of each component and then apply semi-empirical corrections to account for detailed complexities. In this section, we describe the HIREFS model in detail.

3.2.2 System geometry

X rays enter the HIREFS (Figure 3) through a selectable entrance slit. During calibration of the AXAF Observatory, the entrance-slit width remained fixed at 0.2 mm. Next in the optical path is a cylindrical mirror (M1) which focusses the beam in the cross-dispersive direction (vertical or -Z_{XRCF}). This "ASTIG" mirror partially removes astigmatism introduced by the next optical element, a spherical mirror (M2). M2 focusses the beam in the dispersive direction (horizontal or -Y_{XRCF}), projecting the dispersed image of the entrance slit onto the exit slit, after being selectively redirected by a reflection grating. The exit-slit width, also adjustable, remained fixed at 0.2 mm throughout the calibration.

3.2.3 Model for cylindrical mirror (M1)

Consider a cylindrical mirror of radius of curvature r_0, illuminated by a uniform beam, at a central incident grazing angle θ_0. As a result of geometric redistribution of the rays, the reflected beam is nonuniform. Furthermore, the dependence of reflectance upon grazing angle and energy produces energy-dependent beam nonuniformity. These combined effects lead to a HIREFS beam which varies in the cross-dispersion direction.

We derive the geometric term by assuming that the incident beam uniformly illuminates M1, and that M1 redistributes the rays according to the following equation:

$$V(v) = 1 + \frac{2\sqrt{r_0^2 - 2r_0 r_i \sin\theta_0 + r_i^2}\cos\left[v + \tan^{-1}\left[\frac{r_0\cos\theta_0}{r_0\sin\theta_0 - r_i}\right]\right]}{\sqrt{r_0^2 - \left(r_0^2 - 2r_0 r_i \sin\theta_0 + r_i^2\right)\sin\left[v + \tan^{-1}\left[\frac{r_0\cos\theta_0}{r_0\sin\theta_0 - r_i}\right]\right]^2}} . \quad (3)$$

Here, v is the vertical angle of the beam relative to the facility optical axis (FOA) (+ means angled up from the FOA), and r_i is the distance from M1 to the exit slit. For the HIREFS, we take $\theta_0 = 2°$ to be the central grazing angle, effecting a 4° change in direction. The radius of curvature r_0 is manually adjustable on the HIREFS.

We obtain the reflectance as a function of energy, grazing angle, and coating bulk density (ρ), using the Henke [17] optical constants. The grazing angle as a function of v is

$$\alpha(v) = 90° - \csc^{-1}\left[\frac{r_0 \csc\left[v + \tan^{-1}\left[\frac{r_0\cos\theta_0}{r_0\sin\theta_0 - r_i}\right]\right]}{\sqrt{r_0^2 - 2r_0 r_i \sin\theta_0 + r_i^2}}\right] . \quad (4)$$

These combine to produce a Z-dependent nonuniformity term. Figure 14 shows the spatial profile of a Z slice of the beam produced by this term, at two energies.

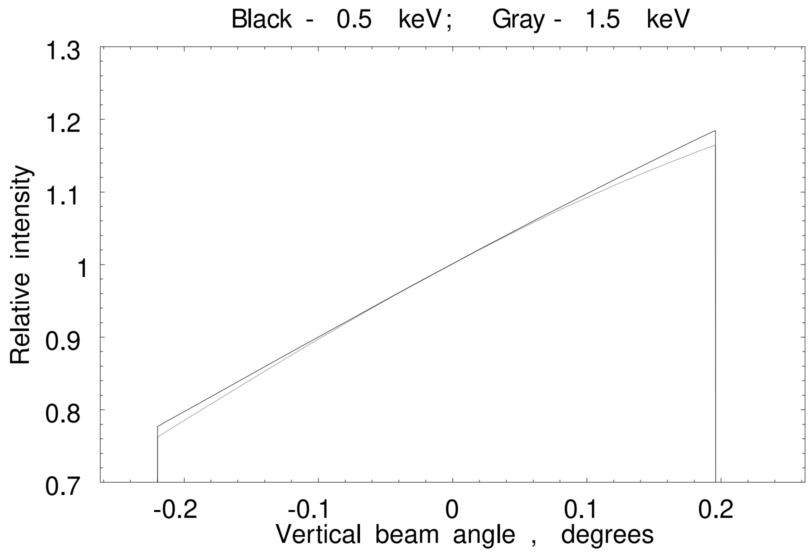

Figure 14: Nonuniformity due to factors affecting the vertical beam profile at 0.5 and 1.5 keV, for best-fit values of r_0 and gold bulk density. This nonuniformity component is independent of the grating selection.

The vertical size of the beam intercepted by the HRMA and BNDs is a small fraction of the total beam leaving the HIREFS. For the settings used in AXAF calibration, the edges of the M1 mirror define the top and bottom edges of the beam. The relative position of the HRMA aperture between these edges is adjustable and, thus, is a parameter of the fit.

3.2.4 Model for spherical mirror (M2)

The M2 mirror is similar to the M1. For simplicity, we neglect its spherical nature and treat it as a cylindrical mirror. The formulae are identical: Only the parameters of gold coating, distance to exit slit, and the radius of curvature differ. M2 overfills the grating and, therefore, is not a constraint on the beam edges. Figure 15 shows the spatial profile of a Y-slice of the beam produced by this term, for several energies.

Before leaving the HIREFS, the beam is, in effect, redirected by an asymmetric grating reflection. This results in a rescaling term for the exiting horizontal beam angle (u), which depends upon the

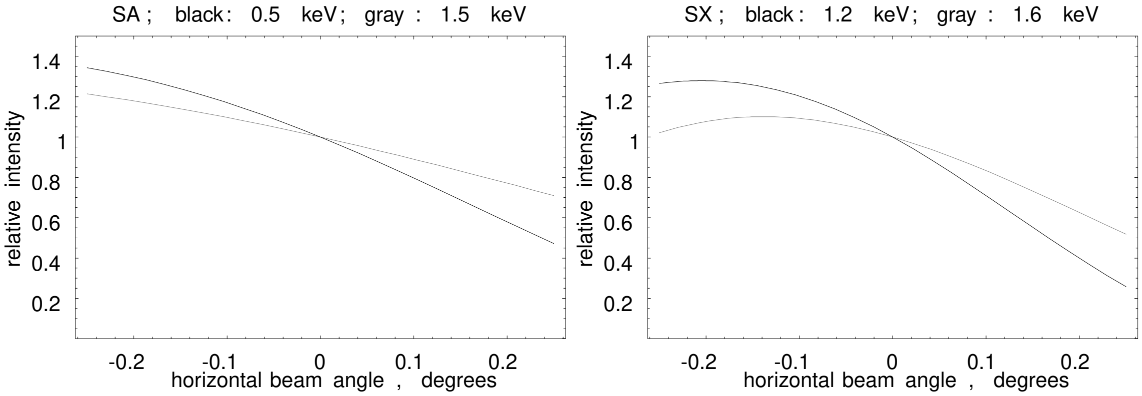

Figure 15: Nonuniformity due to M2 factors affecting the horizontal beam profile, for best-fit values of r_0 and Au bulk density. Left panel is for the SA grating, at 0.5 and 1.0 keV; right, SX grating, at 1.2 and 1.6 keV, This nonuniformity depends upon the grating selection, because the asymmetric nature of the reflection of the 1^{st} diffracted grating order produces a grating-angle-dependent scaling of the exiting horizontal beam angle.

grating angle (ϕ), defined in Equation 6 below. Thus, we apply Equations 3 and 4, substituting u_{M2} for v, giving the following formula for the horizontal angle of the beam leaving M2:

$$u_{M2}(u,\phi) = \frac{u \sin\phi}{\sin(176° + \phi)} \tag{5}$$

3.2.5 Model for SA and SX reflection gratings

As described earlier (§2.2), the HIREFS employs 4 reflection gratings to span 4 energy ranges. We analyzed the beam uniformity, for only the SX and SA gratings — with periods 0.69444 μm and 2.08333 μm, respectively. Because uncertainty in the FPC spectral fits for the 2 tests using the SB grating exceeded the variations in the beam uniformity, we excluded these data from the analysis.

Each flat, reflection grating tilts at a selectable angle, to direct the dispersed orders through the exit slit at a constant 4°. The following equation then gives the grating angle as a function of energy E (in keV) and period P (in μm):

$$\phi(E,P) = 2° + \sin^{-1}\left[\frac{0.0177632}{PE}\right] \tag{6}$$

Because the incident beam converges as it intercepts a grating, the incident grazing angle varies across the grating surface. We asume that the surface of the grating is "blazed" with a sawtooth-pattern cross section, the characteristic angle of the sawtooth being the blaze angle. The efficiency of the grating at a given horizontal beam angle u then depends upon the corresponding incident grazing angle ϕ, the blaze angle β_0, and surface reflectance R_G. Thus, the beam uniformity varies as the relative efficiency at different locations on the grating:

$$G(E,\phi(E,P),\beta_0,u) = (1 - \frac{\cot(\phi + u - \beta_0)]}{\cot\beta_0})R_G(E, 4° + \beta_0 - \phi - u) \tag{7}$$

This equation treats the blaze-angle effect as a simple shadowing term. Figure 16 displays the effect of the gratings on horizontal uniformity.

In essence, the beam leaving the exit slit at any energy is simply an inverted image of the nonuniformly illuminated grating, focussed at different magnifications by the two optics M1 and M2. Because the edge of the grating limits the beam in the horizontal direction, the beam size changes as the grating angle changes. Indeed, the north edge of the beam crosses the north BND detector (FPC_HN) over a range of energies with the SA grating, rendering that detector useless in that range. We further discuss this effect below.

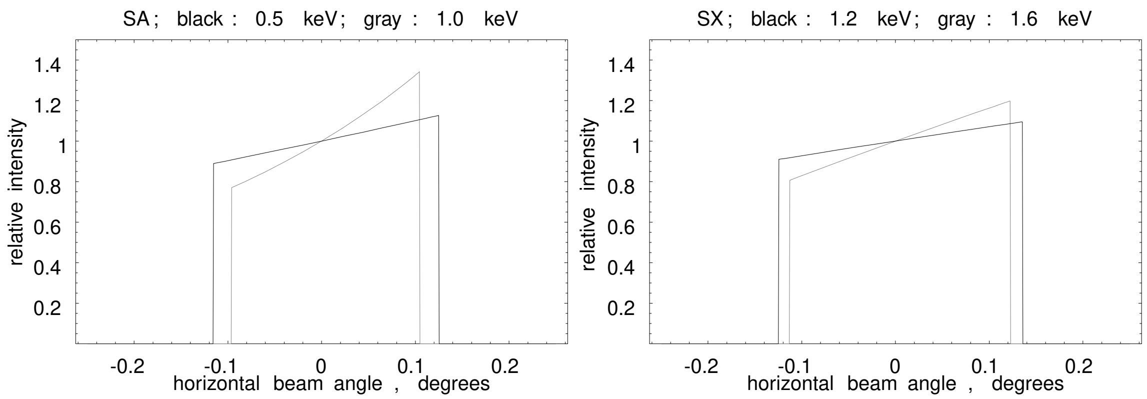

Figure 16: Nonuniformity due to grating factors affecting the horizontal beam profile, for best-fit values of blaze and Au bulk density. Left panel is for the SA grating, at 0.5 and 1.0 keV; right, SX grating, at 1.2 and 1.6 keV, Blaze angles are 0.69° for SA and 1.0° for SX. Note that the beam narrows for higher energy settings, because the projection of the grating in the direction of the beam narrows.

3.2.6 Overall model

We now combine the 3 components described above, to produce an overall beam-uniformity model:

$$\begin{aligned} I(u, v, E, P, \beta_0) &= V_{M1}(v) \times R_{M1}(E, \alpha(v)) \times V_{M2}(u_{M2}(u, \phi(E, P))) \times \\ & \quad R_{M2}(E, u_{M2}(u, \phi(E, P))) \times G(E, \phi(E, P), \beta_0, u) \end{aligned} \tag{8}$$

Here, u and v are, respectively, the horizontal and vertical angular coordinates of the output beam. These relate to the XRCF-Y and XRCF-Z coordinates through $Y = r(u - u_0)$ and $Z = r(v - v_0)$, where u_0 and v_0 are the angular offsets corresponding to the aim of the HIREFS, and r is the distance from the HIREFS to the location of interest.

3.2.7 Beam-uniformity map data

The calibration included a number of beam-uniformity measurements for the HIREFS SA and SX gratings. Section 2 describes the spectral fits for these measurements, which employed the (mapping) monitor detector FPC_5, approximately 40 m from the source. Depending upon the source flux, the tests used one of 2 different apertures and mapping patterns shown in Figure 17.

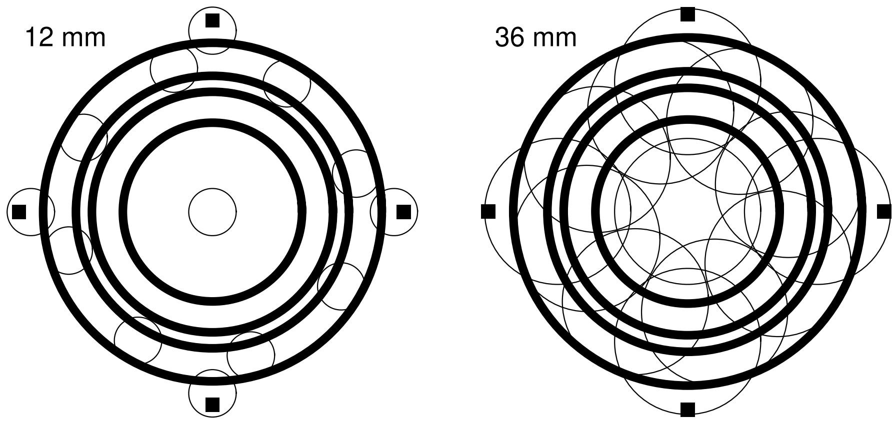

Figure 17: Pattern for beam maps using FPC_5 with 12 mm and 36 mm apertures. The large concentric rings represent the 4 HRMA shells and the 4 out-board squares indicate the FPC_H locations.

The low fluxes from the HIREFS, combined with time constraints for beam mapping, limited our ability to sample the outer regions of the beam. If we had centered the large aperture radially at the outermost edge of the HRMA, it would have been only partially illuminated because of baffling and the extent of the beam, and thus would not have provided useful data about the flux entering the HRMA. Consequently, we must extrapolate the spatial map to the edge, resulting in significant uncertainty, discussed further below.

Table 10 lists the maps that were used for the parameter fitting process described below.

Table 10: HIREFS beam-uniformity maps used for this analysis.

RUNID	Date	Grating	Energy	RUNID	Date	Grating	Energy
113323	970314	SA	0.539	113346	970314	SX	1.250
113319	970313	SA	0.625	113348	970314	SX	1.280
113320	970313	SA	0.640	113357	970315	SX	1.384
113321	970313	SA	0.785	113354	970314	SX	1.546
113311	970313	SA	1.046	113336	970314	SX	1.569
113313	970313	SA	1.078	113338	970314	SX	1.569
113315	970313	SA	1.177	113340	970314	SX	1.616
				113341	970314	SX	1.616

3.2.8 Ensemble fit of beam maps to model

We compared the data with relative fluxes obtained by spectral fits, as described in Section 2, of the beam-uniformity measurements. We simultaneously fit beam maps at a number of energies, for a given grating, using the following procedure:

1. Iteratively fit the M1 radius of curvature r_{0M1}, the vertical aim angle v_0, and coating bulk density ρ_{M1}, to minimize χ^2 for all SA beam maps, maintaining constant initial values for all other parameters. We obtain the model values by integrating Equation 8 over the appropriate aperture size and then normalizing to the average of all map points in the model; we then likewise normalize the data.

2. Iteratively fit the M2 radius of curvature r_{0M2}, the horizontal aim angle u_0, and coating bulk density ρ_{M2}, to minimize χ^2 for all SA beam maps, maintaining constant initial values for grating parameters, and using the M1 parameters found in step 1.

3. Iteratively fit the SA-grating blaze angle β_{0SA} and coating bulk density ρ_{SA}, to minimize χ^2 for all SA beam maps, using the M1 and M2 parameters found in steps 1 and 2.

4. Iterate steps 2 and 3 to obtain the final M2 and SA parameters.

5. Iteratively fit the SX grating blaze angle β_{0SX} and coating bulk density ρ_{SX}, to minimize χ^2 for all SX beam maps, using the M1 and M2 parameters found in steps 1 and 4.

We used the SA beam maps in steps 1 and 2, because the SA tests sample a much larger range of grating angles than do the SX. This facilitates distiguishing the mirror parameters from the grating parameters.

Although the fits of the model to the SA and SX data are statistically poor, the model does predict the qualitative characteristics of the monochromator's output beam. This is especially true for the SA grating, where the model correctly predicts the sign reversal of the horizontal beam gradient. Table 11 lists parameters derived for the two grating cases, using the specific tests listed and adopting the known values $r_{iM1} = 1131$ mm and $r_{iM2} = 871$ mm.

Table 11: Fit model parameters.

parameter	value	parameter	value	parameter	value	parameter	value
v_0	$0.093°$	u_0	$0.031°$	ρ_{SA}	0.19	ρ_{SX}	1.00
r_{0M1}	$32.3m$	r_{0M2}	$21.0m$	β_{0SA}	$0.69°$	β_{0SX}	$0.99°$
ρ_{M1}	0.22	ρ_{M2}	0.95				

3.2.9 Treatment of grating blaze angle for fine adjustment

The residuals of the ensemble fits described in § 3.2.8 show clear systematic trends which permit further refinement of the model. Through trial-and-error we found that it was possible to improve the fit substantially by allowing the blaze angle to vary by a small amount over the surface of the grating. For each point we predict a blaze correction, $\Delta\beta$, which is the change in blaze angle required to adjust the relative beam intensity to the required value. We also calculate the location on the grating,(y_g, z_g), corresponding to each map point. We then perform a 2-dimensional least-squares polynomial fit for the surface function, $\Delta\beta(y_g, z_g)$. Achieving a good fit required a 4^{th}-order by 4^{th}-order polynomial.

As discussed in § 3.2.7, various constraints prevented the beam maps from extending to the edge of the spatial region of interest, which includes the FPC_H detectors. To prevent the polynomial from diverging inside this region we generate additional extrapolated points and perform the final fit using both the data points and extrapolated points.

In order to obtain the extrapolated points, we first evaluate the unextrapolated polynomial at 4 radial positions in (y_g, z_g) space inside the range where the polynomial begins to diverge, and then fit those points to a line. Finally, we evaluate the linear fit at a radial position outside the data-constrained region. Repeating this process every 15° produces an adequate set of extrapolated points. A polynomial fit to the data plus the extrapolated points results in the surface functions shown in Figure 18.

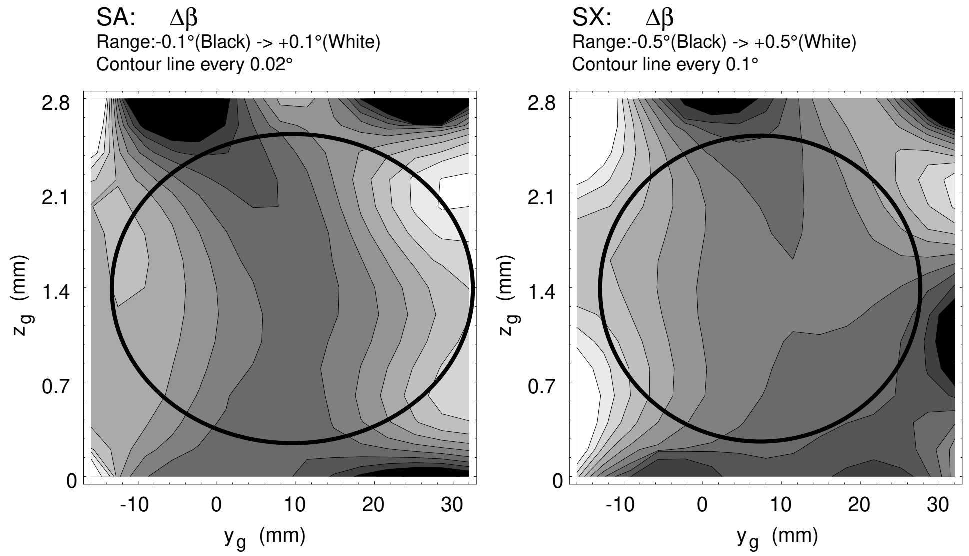

Figure 18: Adjustment to blaze angle, as a function of position on the grating, required for agreement of the model with beam-map data. The encircled region corresponds to the part of the grating producing the observable part of the beam. Extreme variations correspond to ±0.08° for SA and ±0.25° for SX.

3.2.10 Beam edge and aim effects

The spatial width of the HIREFS beam is a function of energy, because the grating edges define the north and south extent of the beam, and the grating angle changes to select the energy. As is evident in the FPC_H data, the north detector FPC_HN is near this edge and, for the higher energies, is in fact partially out of the beam. In addition, during different calibration phases, the edge was in a different location (Fig. 19) due to variation in the aim of the HIREFS from one installation to another.

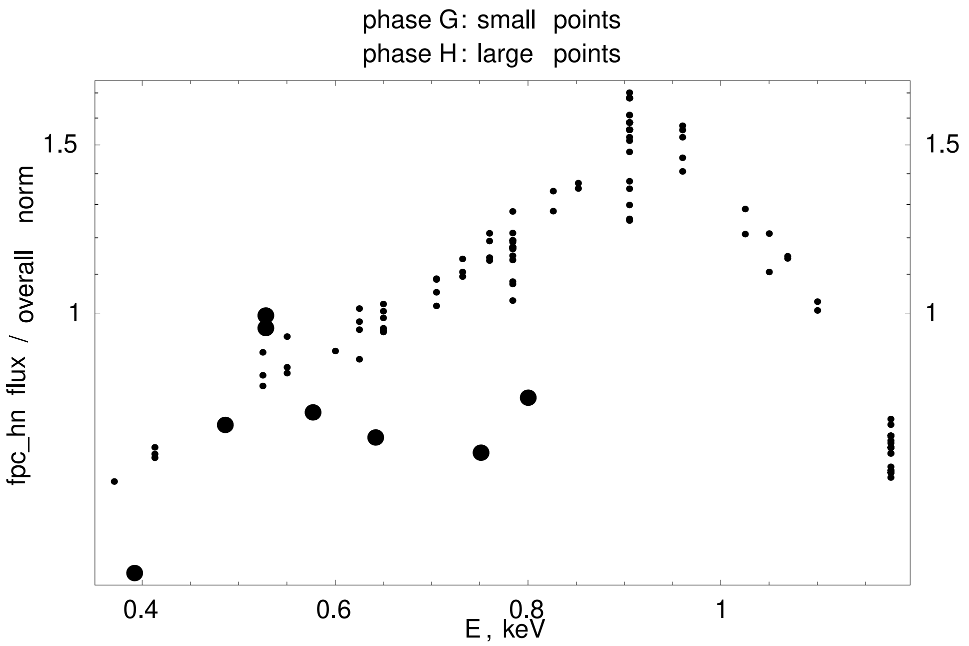

Figure 19: Difference in FPC_HN flux between Series-G and Series-H measurements. The drop indicates that the beam edge intersects the FPC_HN aperture. Clearly the drop occurred at a much lower energy for Series H than it for Series G.

We include the grating edge in the HIREFS model, as well as a parameter for the aim which is simply an angular offset, u_0. Although we treat the edge as a sharp cutoff in the model, it is more complex. Hence, we recommend ignoring data from the north detector for tests meeting the criteria in Table 12.

Table 12: Measurements with HIREFS beam vignetted in FPC_HN.

CMDB Series	HIREFS Grating	Maximum energy for FPC_HN validity
G	SA	0.9 keV
H	SA	0.54 keV

3.2.11 Effects of spectral features

The tungsten rotating-anode source for the HIREFS emits several features — including W-M, O-K, N-K, and C-K lines — which can unpredictably affect the beam. If the input spectrum is changing such that the flux is significantly different over an energy range comparable to the energy resolution of the monochromator, then vignetting effects can produce a substantially different beam uniformity. Furthermore, these effects may be sensitive to the precise grating angle at a scale finer than the repeatability of the HIREFS stage, which implies a reduction in repeatability of the beam's spatial characteristics at the line energies. The model implements no correction for these effects, which result in larger estimated errors and a larger variations in the norms between different tests, at energies near lines (§ 3.3.3). Table 13 lists detectable lines which may alter beam uniformity, when they arise in *any* grating order.

Table 13: Spectral lines affecting HIREFS.

Line	**Energy**	**Relative strength**
W-M$\alpha_{1,2}$	1.775 keV	1.0
W-Mβ	1.835 keV	0.12
W-Mζ_1	1.380 keV	0.06
W-M $M_{III}N_I$	1.684 keV	0.02
W-M $M_{IV}N_{III}$	1.446 keV	0.015
W-Mγ	2.035 keV	0.01
O-Kα	0.525 keV	0.01
C-Kα	0.277 keV	0.01
N-Kα	0.392 keV	< 0.01

3.2.12 Higher orders

In that the model employs the physical geometry of the HIREFS and accounts for reflectivity separately, we predict the uniformity for higher orders by simply calculating the reflectance at the energy of the higher order and leaving all geometric terms unchanged. The resulting model agrees well with the data (Figure 20). Often, the higher order flux errors are large due either to low statistics or to overlapping detector response between neighboring orders. However, the later modeling errors are probably much smaller for the *relative* values than the error bars indicate, due to systematic similarities in the fits. Nevertheless, the model does qualitatively reproduce the changes in the beam indicated by the data.

3.2.13 Scattering

The 3 brightest tungsten lines (§ 3.2.11) appear in most PHA spectra, even when the line does not correspond to the HIREFS selected energy or to a higher order. We attribute these lines to scattering from the optical elements in the HIREFS. Because the grating is the last optical element, it is the most probable source of scattering. Figure 21 shows the flux in the strong lines versus HIREFS energy setting. Because the intensity of the tungsten lines is hundreds of times that of the continuum at the HIREFS resolution, these $< 1\%$ effects are not surprising.

Figure 22 compares beam uniformity for a test where the W-Mα, β lines are reasonably distinct from the other orders (0.784 keV), with one where the 3$^{\mathrm{rd}}$ order is close to W-Mα, β (0.625 keV). We have not yet attempted to model the scattering, so we cannot account for this difference. In future versions, we shall need a more physically accurate description of the grating to account for these effects. However, we achieve some agreement with data away from higher order peaks, if we use the model to produce a scattering prediction by removing all reflectivity effects and assuming that only geometry defines the beam profile. We do this by setting the order value in the model to a small fraction — 0.1, say. Near high orders, the discussion of § 3.2.12 applies. The scattering complicates analysis in the following ways:

1. As shown above, beam uniformity of scattered flux differs from that of a higher order. When the energy of a higher order is near that of a scattered line, features in the PHA spectrum blend, errors in each feature become large, and the fit is poorly constrained.

2. There are 3 detectable scattered features — 1.77, 1.83, and 1.38 keV. For spectral fits, we ignored the 1.38-keV line (§ 2.4.2). Consequently, the agreement between the beam model and the data is poor in this range.

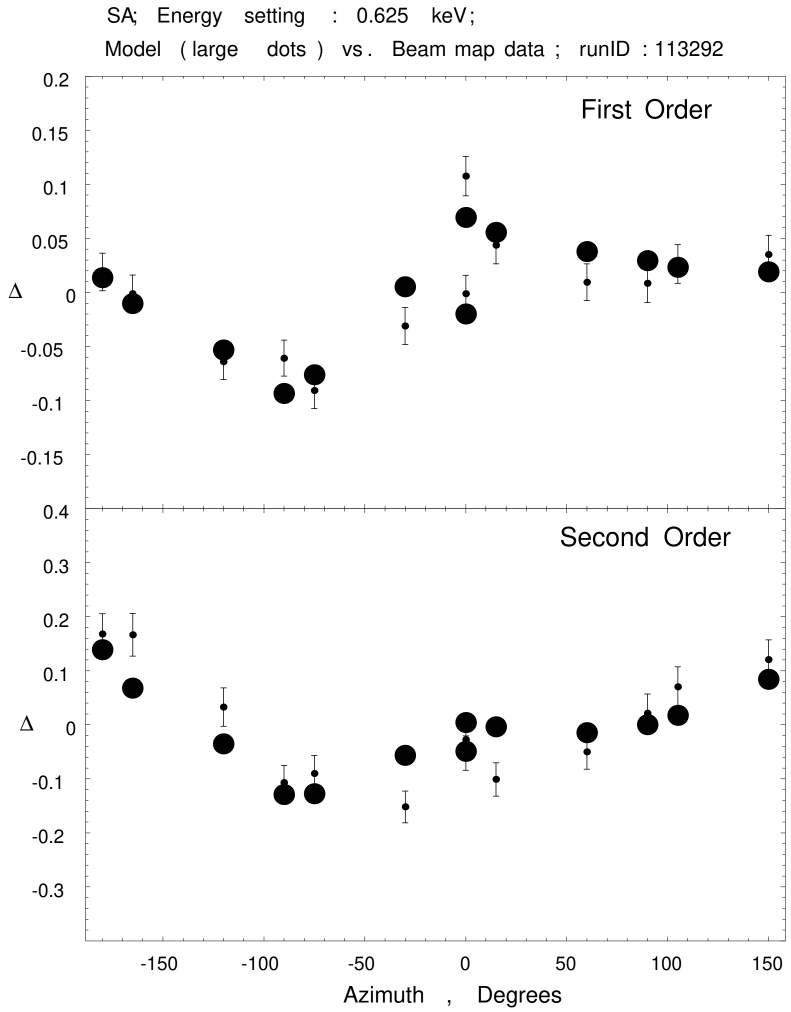

Figure 20: Fractional change Δ from mean flux versus azimuthal angle, for 1^{st} and 2^{nd} order of a 0.625-keV beam map. The azimuth is relative to a south pointing direction from beam center with '+' going toward the top of the beam. Note that the model agrees with the 2^{nd} order reasonably well (RMS error $\approx 5\%$), even though determination of the model ignores 2^{nd}-order data.

3. At high energy settings ($>$ 1.65 keV) for SX, scattering from the 1.77 keV complex so dominates the PHA spectrum that the fitted detector gain falls off consistent with a constant energy for all such tests (§ 2.4.3). Furthermore, the beam is more consistent with a scattered beam, as described above, than with the 1^{st}-order model. Consequently, the normalization for HIREFS-SX measurements above 1.65 keV is poorly determined. It is probably more accurate to treat them as tests at 1.77 keV and apply the beam model for the scattered feature alone.

These complications arise due to limitations in the spectral fitting — specifically, allowing width and gain parameters to be unconstrained. With an improved fitting strategy, we may better separate adjacent spectral features and thus improve the accuracy of the model. However, item 3 above inevitably limits the value of those tests: Because we used the total count rate to determine the integration time and because scattering dominates, the statistical significance of the 1^{st}-order flux is less than desired.

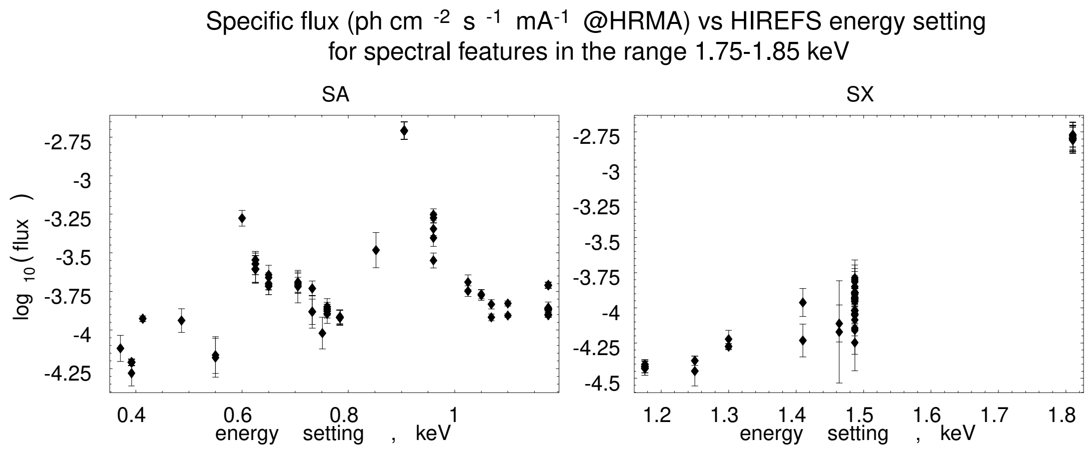

Figure 21: Specific flux in the strong W-Mα,β lines versus HIREFS energy setting. Peaks at 1.8, 0.9, 0.6 and 0.45 keV correspond to orders m = 1, 2, 3, and 4, respectively. Flux at other energies results from internal scattering.

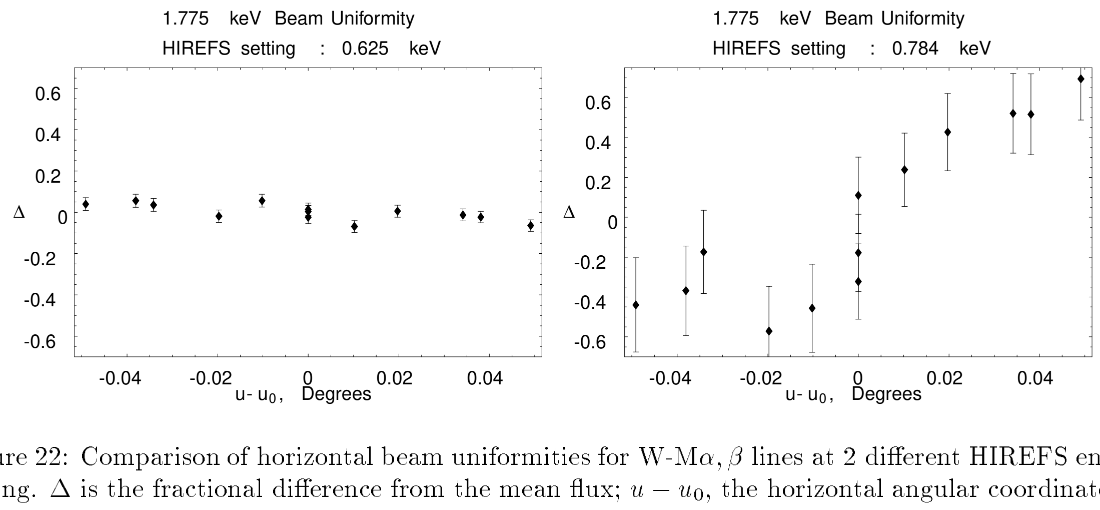

Figure 22: Comparison of horizontal beam uniformities for W-Mα,β lines at 2 different HIREFS energy setting. Δ is the fractional difference from the mean flux; $u - u_0$, the horizontal angular coordinate.

3.2.14 Model comparison with beam maps

In summary, the beam model agrees with the data fairly well for 1^{st} and higher orders, but less well for scattered lines. Figures 23 and 24 compare beam maps to the model. The χ^2 for the fit using only 1^{st}-order data was 113 on 57 degrees of freedom for SA; 129 on 73, for SX. We calculated χ^2 for SA, excluding the partially vignetted points at the north edge for 1.046, 1.078 and 1.117 keV. The χ^2 values indicate that the data are not completely consistent with the model: However, by adding another parameter for the relative aim of the HIREFS, which may be as much as 6 mm, we can easily produce an acceptable χ^2. Because these 2–3% fit errors are usually much smaller than the normalization errors (§ 3.3), we view such an exercise as moot.

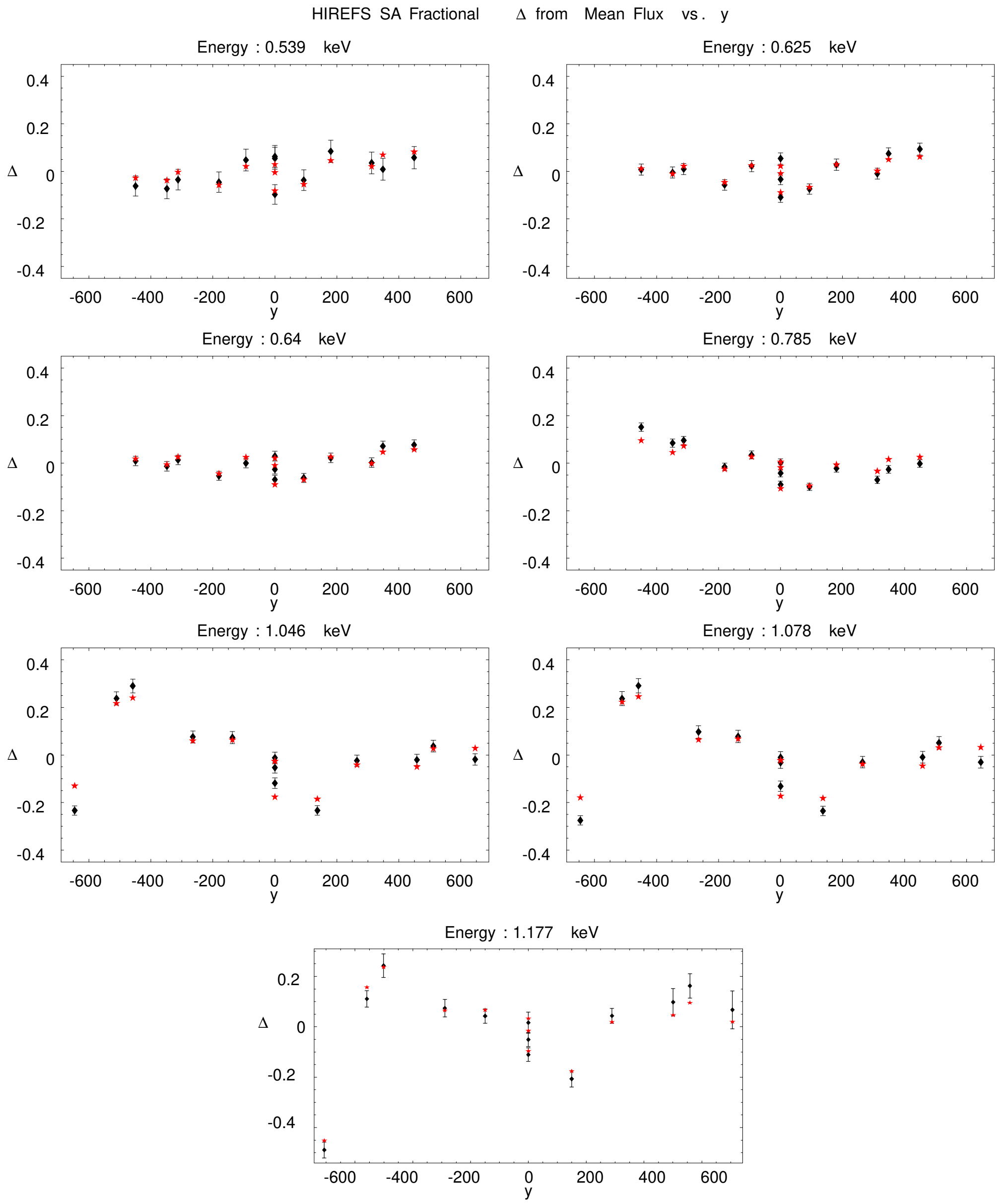

Figure 23: Comparison of fractional difference from the mean flux between map data (diamonds) and beam model (stars) versus XRCF $-Y$ (in mm) at the HRMA for tests using the HIREFS-SA grating.

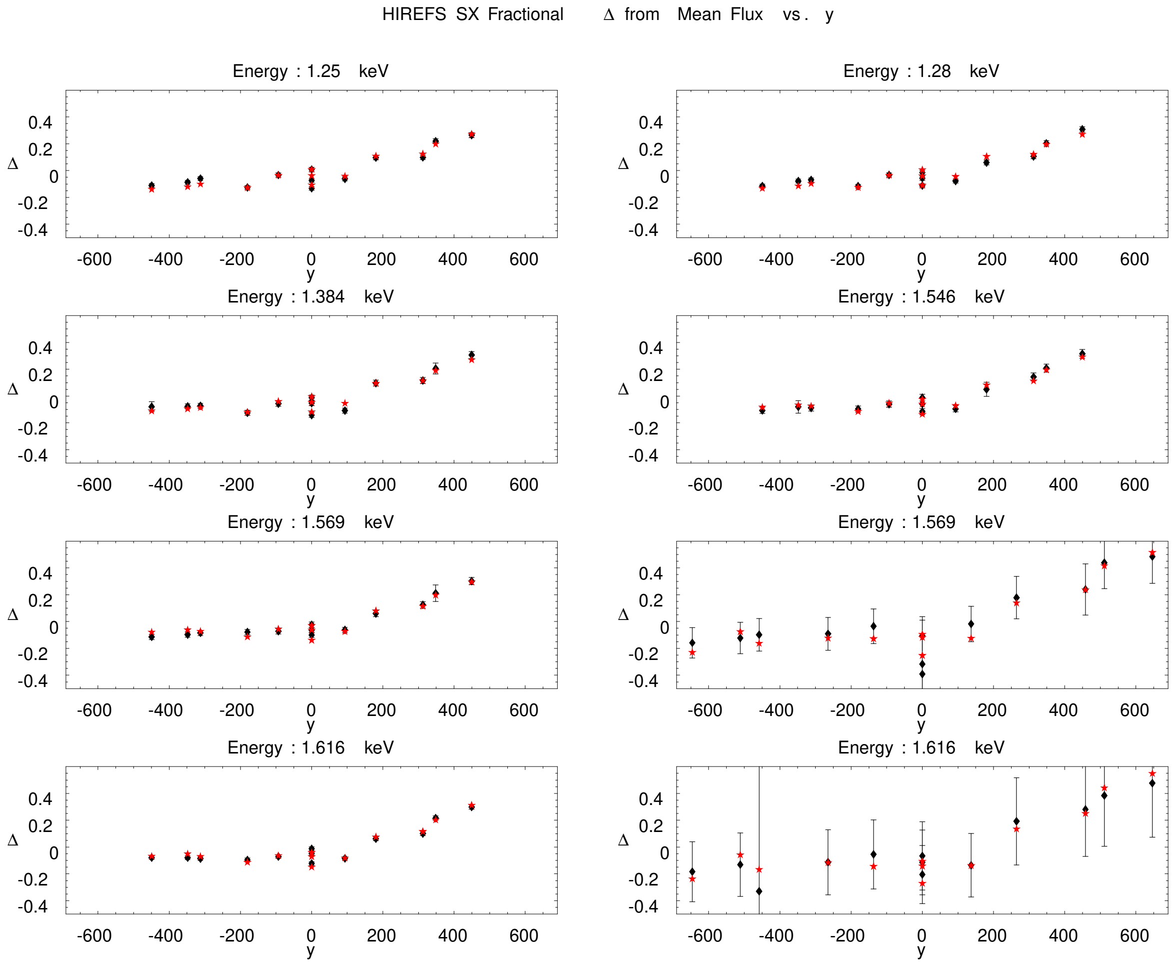

Figure 24: Comparison of fractional difference from the mean flux between map data (diamonds) and beam model (stars) versus XRCF $-Y$ (in mm) at the HRMA for tests using the HIREFS-SX grating.

3.3 Results

We analyzed nearly all tests using the HIREFS, in terms of beam uniformity. Table 14 summarizes the distribution of the 401 tests with grating and energy. Because we had no contemporaneous maps for the 4 SB tests, we excluded them from the analysis. Also, the spectral fit error bars for these 4 tests are enormous compared to the beam non-uniformity, due to the many unresolved spectral orders.

3.3.1 Normalization

We relate the beam uniformity to the measured fluxes in the FPC_H detectors to derive the beam normalization for each test. Because HIREFS count rates are were, FPC_H data for individual measurements typically have relatively poor statistics. Hence, we averaged data over many measurements when they were consistent with a constant flux. Tests within an interval were grouped together when all FPC_H fluxes fit to a constant. This trend analysis and the specific normalization parameters produced are described further in § 3.3.2.

The only parameter of the model that changes among all the tests is the horizontal aim, u_0, which clearly changed between Series G and H as discussed above in § 3.2.10. As a result, the model-derived beam normalization parameters are a function of only energy, grating, and series (G or H). We elected to apply spectral fit results from all the AXAF calibration tests in order both to more thoroughly evaluate the results and associated errors and to provide a product in usable form for groups who elect not to

Table 14: Number of HIREFS tests for each grating and energy.

Grating	keV	# of tests	Grating	keV	# of tests	Grating	keV	# of tests
SA	0.371	1	SA	0.784	48	SX	1.25	2
SA	0.392	56	SA	0.8	1	SX	1.3	3
SA	0.413	3	SA	0.826	2	SX	1.41	2
SA	0.486	1	SA	0.852	2	SX	1.464	2
SA	0.525	3	SA	0.905	48	SX	1.487	61
SA	0.528	2	SA	0.96	5	SX	1.53	2
SA	0.55	3	SA	1.025	2	SX	1.568	2
SA	0.577	1	SA	1.05	2	SX	1.621	2
SA	0.6	1	SA	1.069	2	SX	1.652	2
SA	0.625	4	SA	1.1	2	SX	1.704	2
SA	0.642	1	SA	1.176	47	SX	1.739	2
SA	0.65	6	SB	0.277	1	SX	1.81	48
SA	0.705	4	SB	0.311	1	SX	1.855	3
SA	0.732	3	SB	0.371	1	SX	1.876	2
SA	0.751	1	SB	0.392	1	SX	1.96	2
SA	0.76	4	SX	1.176	3	SX	2.	2

perform their own spectral fits.

Figs. 25 and 26 show plots of all overall norms, as defined in § 3.3.2, vs. energy for the various orders. The enhancement in flux between 1.65 and 1.85 keV in Fig. 25 is the result of a blending of the 1st order with a large scattered component at 1.774 keV. The scattering appears to be $\sim 50\%$ of the total in this range. The drop at $\sim$1.85 keV is caused by a drop in the HIREFS 1st-order efficiency, which implies that the three highest energy SX points are incorrectly identified and should be labeled 1.775 keV, since almost all the flux is a result of the scattered W-L line as discussed in § 3.2.13. A similar effect is evident in the 2nd order data in fig. 26 above energy settings $\sim$0.65 keV. This is the result of scattering from the 1.38 keV W-Mζ line at an intensity level of $\sim 10-20\%$ of the total flux. Likewise, the scattered fluxes plotted in fig. 21 are likely to have a small contribution from higher orders with energies > 1.6 keV. We have elected not to include these necessary corrections in the data products at this time, to avoid inconsistency with the spectral fit products. However, we recommend that users account for these effects in their future analyses.

Figs. 27 and 28 show how the ratio of average incident HRMA flux to average BND flux varies with energy. While this is an indicator of the importance of nonuniformity in a given test's overall normalization, it may not be an accurate scaling factor for the reasons outlined in § 3.1. The energies where this ratio deviates most substantially from 1 are the energies where the FPC_HN detector was partially out of the beam and therefore should not be used as mentioned in § 3.2.10.

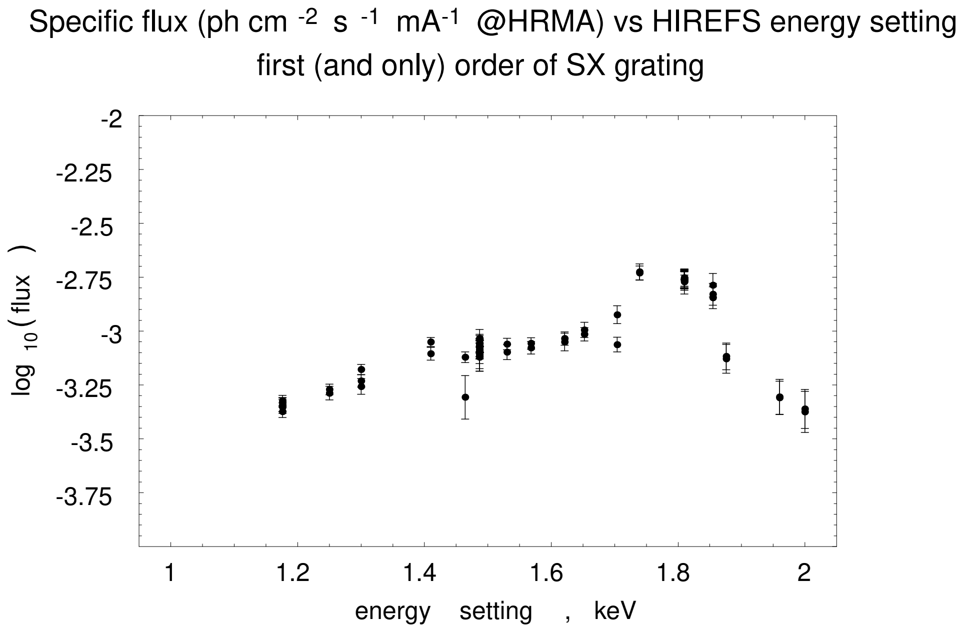

Figure 25: 1st order flux vs energy for all HIREFS tests using the SX grating. The flux is the aperture-weighted average over all HRMA shells with the unrealistic assumption of azimuthal symmetry in each shell. The factor of 2 increase at 1.65 keV is the result of the unresolved scattered 1.77 keV line. The decrease at 1.85 keV appears to be the result of a drop in the 1st-order flux based on the change in detector gain observed in the spectral fits in this range. A weaker enhancement in the 1.35-1.55 keV range is caused by the 1.38 keV scattered line.

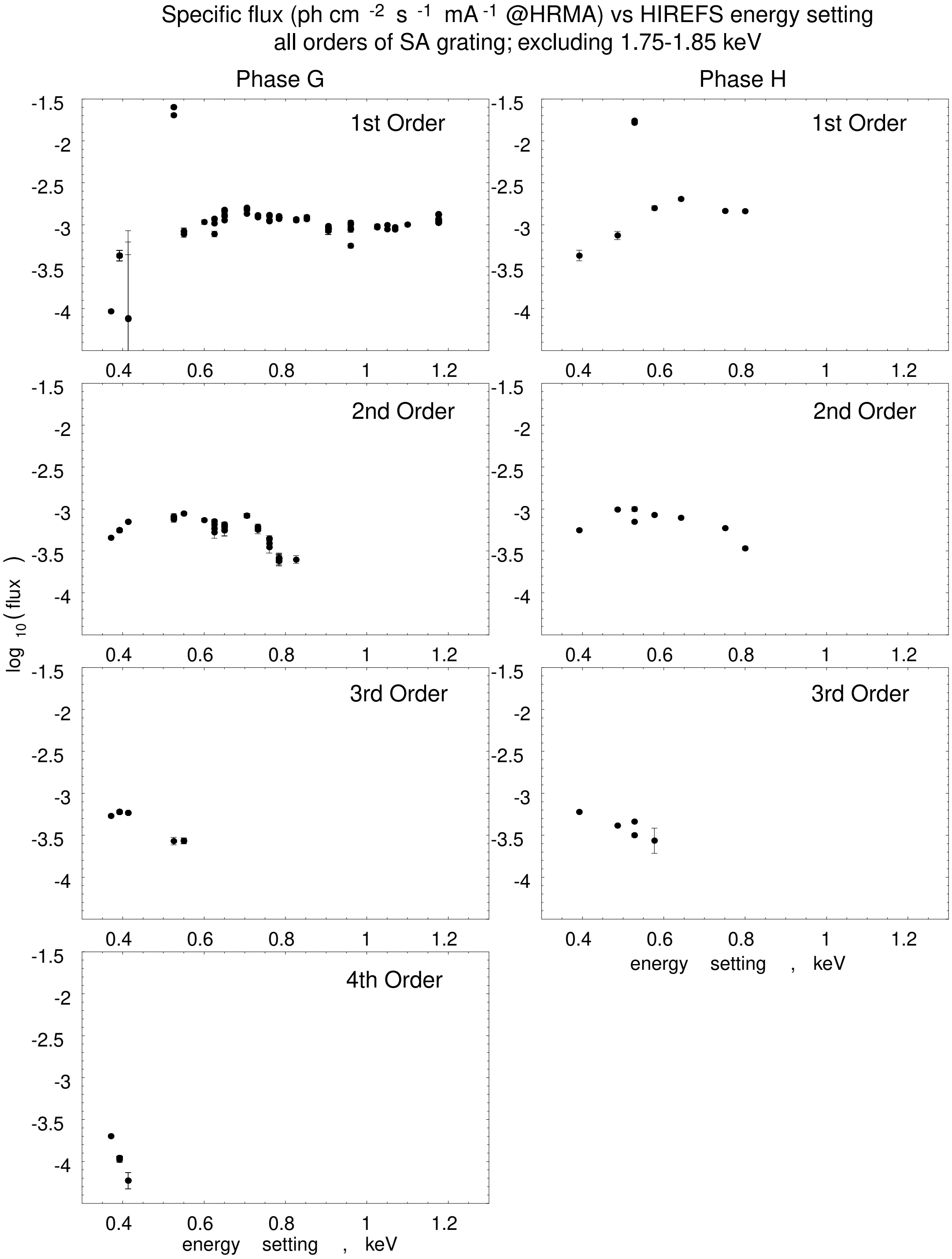

Figure 26: First order flux vs energy for all HIREFS tests using the SA grating. The flux is the aperture-weighted average over all HRMA shells with the unrealistic assumption of azimuthal symmetry in each shell. Spectral lines from anode contamination at O-K and N-K are apparent. The flux increases above 1.35 keV (energy setting $\times$ grating order) in higher orders because of 1.38 keV contamination at the $10-20\%$ level.

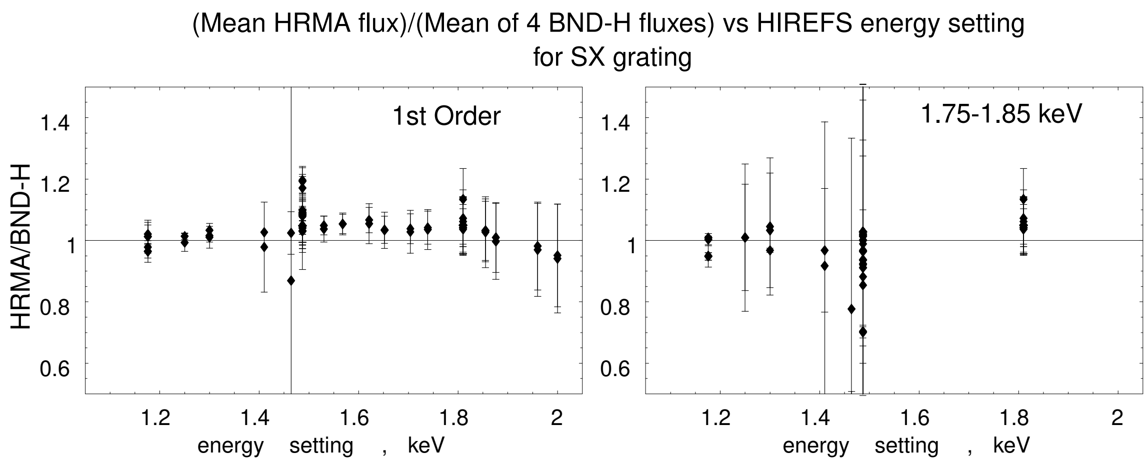

Figure 27: Ratio of the HRMA to FPC_H flux for tests using the SX grating. The ratio is the HRMA aperture-weighted average flux divided by the average flux in those FPC_H detectors which are fully illuminated by the beam.

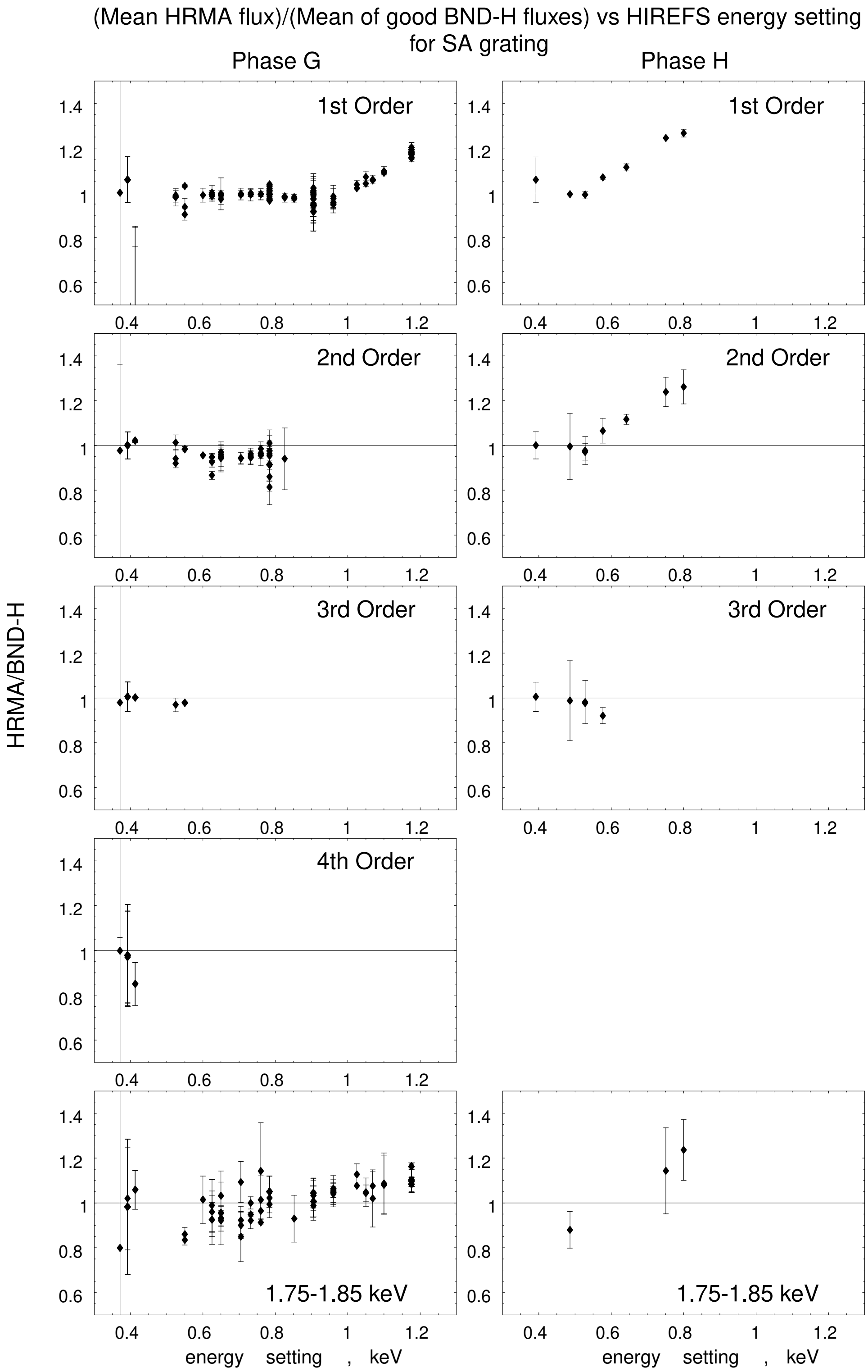

Figure 28: Ratio of the HRMA to FPC_H flux for tests using the SX grating. The ratio is the HRMA aperture-weighted average flux divided by the average flux in those FPC_H detectors which are fully illuminated by the beam. The significant increases above 0.9 keV in Series G, and 0.54 keV in Series H are the result of FPC_HN being partially out of the beam and therefore excluded. The model properly accounts for the significantly higher flux on the north side of the HRMA which is not observed in FPC_HN because of this out-of-beam condition.

3.3.2 Data Product Summary

The data product is a table in *rdb* format. The contents are summarized in the Figs. 29 which reproduces part of the *rdb* header. Again we emphasize the column "goodBNDH" which lists which BNDs are used in the analysis is critical to avoiding significant systematic errors resulting from FPC_HN being outside of the beam.

A block of data is provided for each of up to 5 "lines" as identified in the spectral fits. The key elements of each block include:

1. measured absolute FPC_H fluxes and errors
2. modeled relative fluxes at the FPC_H locations
3. modeled relative fluxes in each HRMA shell and quadrant
4. an overall normalization factor and error.

These items are described in more detail below.

The columns labeled qFlux$i$ and qFluxErr$i$ contain the values for absolute specific flux ($ph\ cm^{-2}\ s^{-1}\ mA^{-1}$) and error in the FPC_H detectors. q identifies the FPC_H detector (t-top, n-north, b-bottom, s-south) and i identifies the spectral "line" with energy defined in the column labeled energy$i$. The column qFluxBOCi contains an integer identifier which specifies how the flux and error were derived, a "based-on code" (BOC).

As mentioned in § 3.3.1, we performed a trend analysis on HIREFS data in order to improve the statistical accuracy. The BOC value specifies how the resulting fluxes were derived within the trend analysis framework as follows:

-1	-	anomalous
0	-	spectral fit
1	-	constant trend
2	-	constant trend; fit errors larger than standard deviation
3	-	constant trend; some anomalous tests
4	-	stepwise variable trend
5	-	stepwise variable trend; some anomalous tests

The analysis was performed on each set of tests for each detector with the same "setEnergy" and "grating" values and proceeded as follows for each spectral order or line at energy$i$:

1. If a set consisted of $n = 3$ or fewer tests then no trend analysis was performed. The flux values,Ψ and errors, σ_Ψ were set to the spectral-fit values, (Ψ_s ,$\sigma_{\Psi,s}$), and BOC was set to 0.

2. If $n > 3$, a 1-parameter χ^2 fit for the specific flux, Ψ_t, was performed and an associated confidence level (c. l.) was calculated from the standard χ^2 distribution.

3. If the c. l. from step 2 was in the range 0.05-0.95, the fit was considered acceptable. A 1σ error, $\sigma_{\Psi,t}$, was derived by varying Ψ_t to achieve an increase in χ^2 of 1. We set $\Psi = \Psi_t$, $\sigma_\Psi = \sigma_{\Psi,t}$, and $BOC = 1$ for any test where $\sigma_{\Psi,t} < \sigma_{\Psi,s}$. Each test where $\sigma_{\Psi,s} < \sigma_{\Psi,t}$ was treated as in step 1.

4. If the c. l. from step 2 was < 0.05, the implication is that the errors are overestimated. In this case, we compute the standard deviation, Δ_t of the spectral-fit specific fluxes. For tests where $\Delta_t < \sigma_{\Psi,s}$ we assigned $\Psi = \Psi_t$, $\sigma_\Psi = \Delta_t$, and $BOC = 2$. Each test in the set with $\sigma_{\Psi,s} < \Delta_t$ was treated as in step 1.

5. If the c. l. from step 2 was > 0.95, we first considered the possibility that a small fraction of the tests are anomalous either because of bad spectral fits or some anomalous test event that has not yet been identified. We identify candidate anomalous tests based on the criterion that they have less than a 50% probability of occurring in a sample of n tests assuming values are distributed normally.

6. If the number of anomalous candidates, n_a, is $< 15\%$ of n, we remove them from the trend-analysis set. For these we assign, $\Psi = \Psi_s$, $\sigma_\Psi = \sigma_{\Psi,s}$, and $BOC = -1$. It remains for future work to determine if they are really anomalous. If $n_a > 0.15n$, then we proceed to step 8, abandoning the constant flux hypothesis. The set remaining after removing the anomalous candidates was reanalyzed following steps 1 and 2.

7. If the c. l. from step 6 was in the range 0.05-0.95, the fit was considered acceptable. A 1σ error, $\sigma_{\Psi,t}$, was derived by varying the specific flux parameter to achieve an increase in χ^2 of 1. We set $\Psi = \Psi_t$, $\sigma_\Psi = \sigma_{\Psi,t}$, and $BOC = 3$ for any test where $\sigma_{\Psi,t} < \sigma_{\Psi,s}$. Each test where $\sigma_{\Psi,s} < \sigma_{\Psi,t}$ was treated as in step 1. The c. l. from step 6 was never < 0.05.

8. If the c. l. from step 6 was still > 0.95, we considered the possibility the flux may have changed on long time scales, > 12 hours. We break a set of tests into groups, according to time, so that no two tests in a group are separated by more than 12 hours. Tests at the same energy were usually clustered together in time so typically 4 to 5 groups of 8-12 tests were formed at the frequently tested energies listed in table 14. The temporal midpoint between tests separated by more than 12 hours is chosen as the transition point between steps in a stepwise variable trend model.

9. A process analogous to steps 1, 2, 4, 5, 6 and 7 is performed on the groups with a free parameter for the specific flux in each time step. If in the end no acceptable fit can be found, then we conclude that the errors from the spectral fits are the best that can be achieved and treat each test individually as in step 1.

Fig. 30 compares spectral-fit vs. trend-fit fluxes and errors. Beam uniformity results can be applied without using these trend-fit flux values. The following paragraphs describe how to derive normalization parameters from these or user-derived FPC_H fluxes.

The columns labeled qFluxMod$i$ are the modeled relative fluxes in the FPC_H detectors with energy defined in the column labeled energy$i$. These are derived from evaluation of eq. 8 for $I_{q,i}$ at each detector location, $(q = t, n, b, s)$. The values are normalized by the parameter, k_i, given by:

$$k_i = \frac{\sum_q I_{q,i}}{n_q}. \tag{9}$$

where the sum is over only the detectors specified in column "goodBNDH" and n_q is the number of such detectors. The values are then simply:

$$q\text{FluxMod}i = \frac{I_{q,i}}{k_i}. \tag{10}$$

which implies that $\sum_q q\text{FluxMod}i = 1$. The value of qFluxMod$i$ for any detector excluded from column "goodBNDH" is 0.

The columns labeled ssHRMAqqi are the modeled relative fluxes in HRMA shell s, quadrant q, with energy defined in the column labeled energy$i$. These are also derived from evaluation of eq. 8 at 10 equally spaced points for each quadrant of each shell. The each average of these points, $I_{s,q,i}$, is normalized by the parameter, k_i from eq. 9, such that:

$$\text{s}s\text{HRMAq}qi = \frac{I_{s,q,i}}{k_i}. \tag{11}$$

The resulting values were found to agree with numerical integration over the subapertures to $< 1\%$, except in the case where the beam edge impinges on the outer HRMA shell. In these cases the average may differ by as much as 10% from the integration value. However, error due to uncertainty in the true location of the beam edge is equally large in these cases. There were only 2 tests where the HRMA was not fully illuminated: H-HAS-EA-10.005 and H-HAS-EA-10.006.

The columns labeled norm$i$ and normErr$i$ contain the values for an absolute specific flux normalization factor and error which convert the relative fluxes described above into absolute fluxes $(ph\ cm^{-2}\ s^{-1}\ mA^{-1})$

with the associated error. To derive each norm$i = \Phi$, take $y_q = q$Flux$i$ and $\sigma_q = q$FluxErr$i$, or similar user-derived FPC_H absolute fluxes and errors. Also, let $x_q = q$FluxMod$i$. We minimize χ^2 where:

$$\chi^2 = \sum_q \frac{(y_q - \Phi x_q)^2}{\sigma_q^2}. \tag{12}$$

We assign $a = \sum_q y_q^2/\sigma_q^2$, $b = \sum_q x_q y_q/\sigma_q^2$, and $c = \sum_q x_q^2/\sigma_q^2$. The solution is:

$$\Phi = \frac{b}{c}, \tag{13}$$

and

$$\chi^2_{min} = a - \frac{b^2}{c}. \tag{14}$$

The 1σ error, σ_Φ, derived from the fit is:

$$\sigma_\Phi = \sqrt{\frac{\chi^2_{min}}{c(n_q - 1)}}. \tag{15}$$

In the equations above the sum is over only the detectors specified in column "goodBNDH" and n_q is the number of such detectors.

To obtain the counting rate in a focal plane detector from the source component at energy$i$, $R_{fp,i}$ use the following equation:

$$R_{fp,i} = \text{norm}i \times A_{eff,all} \times j \times \sum_{q,s} (\text{s}s\text{HRMAq}qi \times \frac{A_{eff,q,s,i}}{A_{eff,all}} \times QE_{q,s,i}), \tag{16}$$

where $A_{eff,q,s,i}$ is the combined HRMA/grating effective area (cm^2) at energy$i$ in shell-s, quadrant-q, $A_{eff,all}$ is the combined HRMA/grating total effective area (cm^2) at energy$i$, $QE_{q,s,i}$ is the average detector quantum efficiency for energy$i$ photons coming from the solid angle of shell-s, quadrant-q, and j is the beam current (mA). For reference only, we have included the sum from eq. 16 in the table column labeled allHRMAi. These values are based on an unrealistic HRMA model where A_{eff} is independent of quadrant and energy and varies only as the geometric aperture area of each shell, and $QE = 1$. The products of values in column allHRMAi times corresponding ones in column norm$i$ were used to generate the data for figs. 21, 25, 26, 27 and 28.

We did not provide error estimates for the relative shell fluxes, ssHRMAqqi. These errors could be useful to calculate, for example, the error in the ratio in the flux between two shells or quadrants. Relative fluxes for the inner 3 HRMA shells are well determined by the beam maps and we estimate the errors from the RMS error of the model fit to be 3% for 1^{st} and higher orders and $\sim$ 6% at scattered lines. The outer shell error is dominated by extrapolation uncertainty as discussed in § 3.2.7. The ability of the model to gauge the flux in the FPC_H detectors is a measure of the extrapolation error and this is supplied in column normErr$i$. We suggest using the conservative value $\sqrt{n_q}$normErr$i$/norm$i$ as an estimate of the relative flux error for shell-1 quadrants.

The .rdb file is available at the project science ftp site as hrf_bu1_out.rdb. Summaries of the analysis at each energy are available in the subdirectory ~/hrfBUResults in the form of Mathematica notebooks. These can be read by a free, downloadable application called MathReader from www.wolfram.com.

3.3.3 Summary of Current Limitations and Potential Improvements

Using the beam uniformity model, we are able to reproduce the HIREFS beam map data at the $2-3\%$ level for 1^{st} and higher orders. The following are known limitations of the HIREFS beam uniformity and normalization results:

1. SX tests at energies above 1.6 keV are highly contaminated with unresolved 1.77 keV scattering, above 1.85 keV almost all the flux is from this line.

2. 1.77 keV line flux probably includes a small amount of unresolved higher orders in the range 1.6-1.85 keV.

3. Higher orders in the range 1.35-1.6 keV are contaminated with 1.38 keV scattering at the $10-20\%$ level.

4. The scattered lines are not well described by the beam uniformity model resulting in RMS errors of $10-15\%$.

5. FPC_HN is partially out of the beam above 0.9 keV for Series G and above 0.54 keV for Series H for SA tests.

6. Beam uniformity maps did not sample the edges of the beam well, requiring extrapolation and associated error.

The following areas may be explored to further reduce uncertainties resulting from nonuniformity in the HIREFS beam:

1. If another spectral fitting iteration is performed with constrained gain and Polya h parameters, it may be possible to include the 1.38 keV scattering feature. This may also improve resolvability of relative fluxes of nearby lines or orders. Another iteration on the beam uniformity model would then be warranted to incorporate these improvements.

2. A detailed grating dispersion efficiency model is needed to explain the scattering shown in fig. 21. This model may help describe the beam uniformity in the scattered lines more accurately than the current model.

3. Currently, we only use FPC_5 data to constrain the model because it was developed before absolute efficiencies for FPC_5 were available, and we had no direct way of relating FPC_H data to the beam maps. FPC_5 efficiencies are now available and may help to reduce the extrapolation errors discussed in § 3.2.7 and § 3.3.2.

4. An alternative approach to the trend analysis would be to sum spectra from similar tests and perform the spectral fit on the combined spectrum. The higher statistics may reduce the systematic errors described in § **??**. The result could either be used to constrain parameters for individual fits, or produce a single set of fluxes for the whole test ensemble.

5. Based on the results of figs. 25 and 26 an absolute flux model of the HIREFS appears feasible and could reduce normalization errors further.

6. If deemed necessary, additional beam maps could be performed to reduce extrapolation errors.

```
#trwid:      trwid
#irig:decimal irig start time (fpchb) of test in days
#grating:    HIREFS grating
#setEnergy:  HIREFS energy setting in keV
#rasI:X-ray  source current in mA
#goodBNDH:   which fpcs are used to obtain the normalization
#energy1:    energy of line in keV1
#norm1:      normalization factor of line;1
#normErr1:   error in normalization factor of line 1
#tFlux1:     fpcht flux ph cm^-2 s^-1 mA^-1 @HRMA in line 1
#tFluxErr1:  error in tFlux1
#tFluxBOC1:  code to indicate basis of tFlux1
#tNormMod1:  model relative fpcht flux in line 1
#nFlux1:     fpchn flux ph cm^-2 s^-1 mA^-1 @HRMA in line 1
#nFluxErr1:  error in nFlux1
#nFluxBOC1:  code to indicate basis of nFlux1
#nNormMod1:  model relative fpchn flux in line 1
#bFlux1:     fpchb flux ph cm^-2 s^-1 mA^-1 @HRMA in line 1
#bFluxErr1:  error in bFlux1
#bFluxBOC1:  code to indicate basis of bFlux1              Repeated
#bNormMod1:  model relative fpchb flux in line 1           for each of
#sFlux1:     fpchs flux ph cm^-2 s^-1 mA^-1 @HRMA in line 1   5 energies
#sFluxErr1:  error in sFlux1
#sFluxBOC1:  code to indicate basis of sFlux1
#sNormMod1:  model relative fpchs flux in line 1
#allHRMA1:   relative whole HRMA flux in line 1
#s1HRMAqt1:  relative HRMA shell-1 quad-t flux in line 1
#s1HRMAqn1:  relative HRMA shell-1 quad-n flux in line 1
#s1HRMAqb1:  relative HRMA shell-1 quad-b flux in line 1
#s1HRMAqs1:  relative HRMA shell-1 quad-s flux in line 1
#s3HRMAqt1:  relative HRMA shell-3 quad-t flux in line 1
#s3HRMAqn1:  relative HRMA shell-3 quad-n flux in line 1
#s3HRMAqb1:  relative HRMA shell-3 quad-b flux in line 1
#s3HRMAqs1:  relative HRMA shell-3 quad-s flux in line 1
#s4HRMAqt1:  relative HRMA shell-4 quad-t flux in line 1
#s4HRMAqn1:  relative HRMA shell-4 quad-n flux in line 1
#s4HRMAqb1:  relative HRMA shell-4 quad-b flux in line 1
#s4HRMAqs1:  relative HRMA shell-4 quad-s flux in line 1
#s6HRMAqt1:  relative HRMA shell-6 quad-t flux in line 1
#s6HRMAqn1:  relative HRMA shell-6 quad-n flux in line 1
#s6HRMAqb1:  relative HRMA shell-6 quad-b flux in line 1
#s6HRMAqs1:  relative HRMA shell-6 quad-s flux in line 1
#energy2:    energy of line in keV2
  •
  •
  •
```

Figure 29: HIREFS Beam uniformity *rdb* table header. Column headings in the box are repeated 5 times for each of up to 5 orders or scattered lines in the spectral fits.

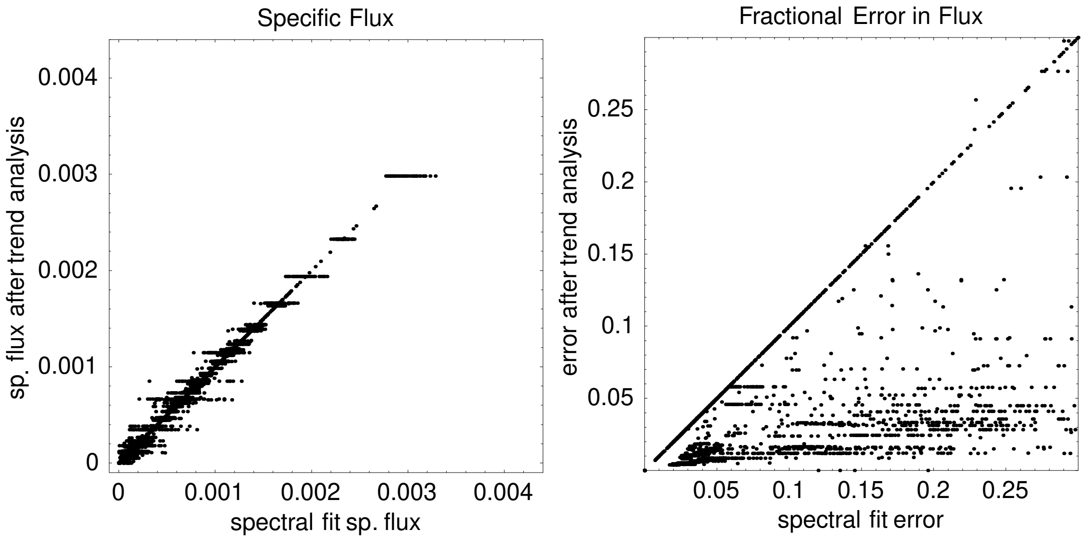

Figure 30: Scatter Plot comparing specific flux ($ph\ cm^{-2}\ s^{-1}\ mA^{-1}$) and fractional error in flux after applying a trend analysis with results of spectral fitting alone.

4 SSD internal calibrator

4.1 Objectives

This section describes the analysis of spectra taken with the BND Solid-State Detector (SSD_5) when the ^{244}Cm calibration source was in place. The goal is to determine variations of detector parameters (gain and resolution) with time and measure efficiency changes due to accumulation of ice on the detector. The following subsections describe the data and the procedures used to analyze the spectra (§ 4.2) and provide an overview of current results (§ 4.3).

During and preceding calibration of the AXAF observatory, we obtained more than 3500 raw PHA files containing ^{244}Cm spectra. For contemporaneous spectra — i.e., those taken within a few hours of one another — we inspected the light curve for anomalies, excluded those anomalous data, and channelwise added the contemporaneous data to create $\sim$ 120 XSPEC-readable FITS PHA d Excluded anomalous data fall into the following categories:

- One measurement used a 2 μsec shaping time; all others used 10 μsec.
- The detector warmed during one measurement, temporarily degrading the energy resolution.
- Spectral lines had a 'shoulder' in some of the early (pre-calibration) data.
- During one iteration, the count rate dropped inexplicably.

4.1.1 Gain and energy scale

The photon energy E is related to the SSD offset, gain G, and channel through

$$E(\mathrm{eV}) = \mathrm{offset} + G \times \mathrm{channel}\ ; \tag{17}$$

the resolution function is

$$\sigma(\mathrm{eV}) = [C + P \times E(\mathrm{eV})]^{1/2}\ . \tag{18}$$

The following table shows how to relate the COD model parameters to JMK model parameters.

```
JMK     COD
---     ---
ch_off= -((p1+p2+3)/p2)
mu    = 3/p2
broad = sqrt(p3)/p2
fano  = p4/3
```

Where P1=offset, P2=G, P3=C and P4=P. The fano factor comes from eqns. 2.47, 2.1, 2,45 in the JMKMOD version 7.0 manual, and assuming 1/h=0, E¿¿E0, and w=3 eV. It is worth noting that the pulser peak location is given in the JMKMOD version 7.33 by pulsepos+ch_off+1 whereas in v7.0 it was at pulsepos.

Figures 31 and 32 show the temporal variation in the model's (§ 4.2) gain and offset parameters. Figure 33 displays the resolution parameters, C and P, against time.

4.1.2 Icing

Figures 34, 35, and 36 show temporal variations of several of the more important model (§ 4.2) fitted line strengths.

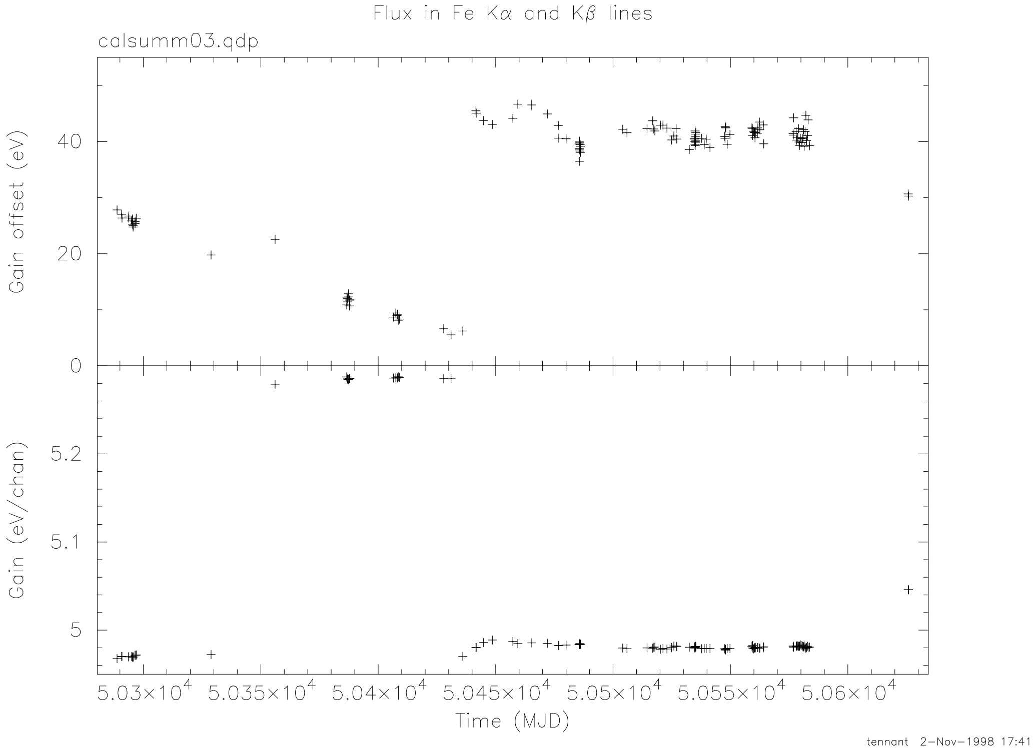

Figure 31: Temporal dependence of model gain and gain offset parameters.

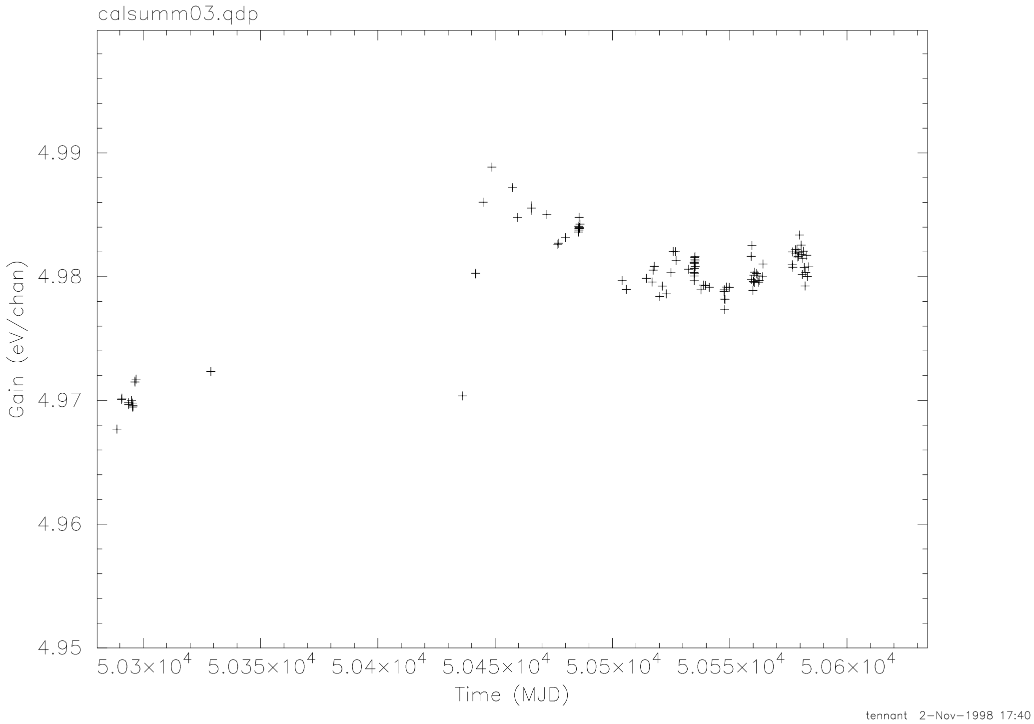

Figure 32: Temporal dependence of model gain parameter excluding high-gain interval from MJD $\sim$ $50350 - 50430$.

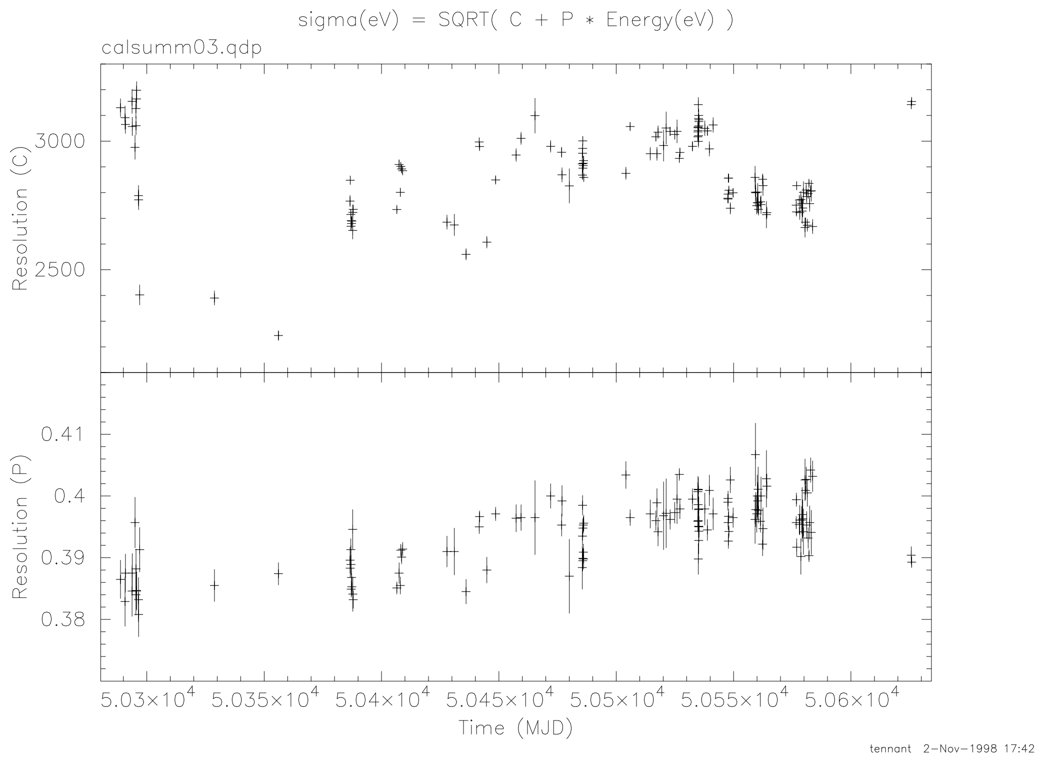

Figure 33: Temporal dependence of model resolution parameters.

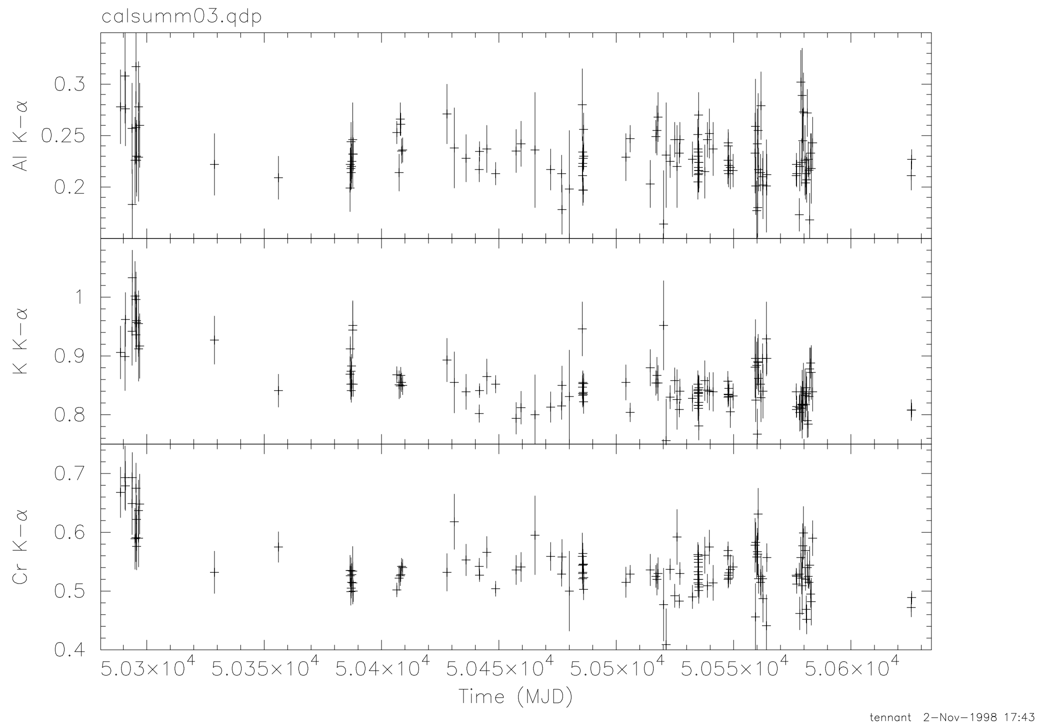

Figure 34: Temporal dependence of modeled line strengths for several lines. There is no significant time dependence.

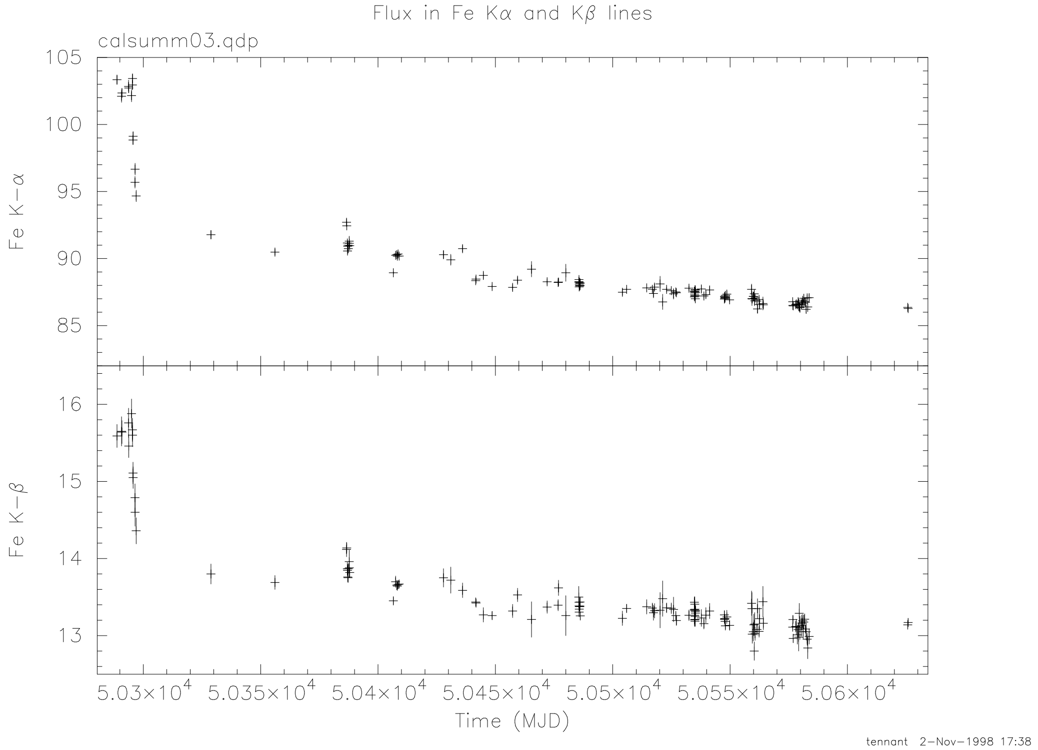

Figure 35: Temporal dependence of modeled line strengths for the Fe-K complex of lines.

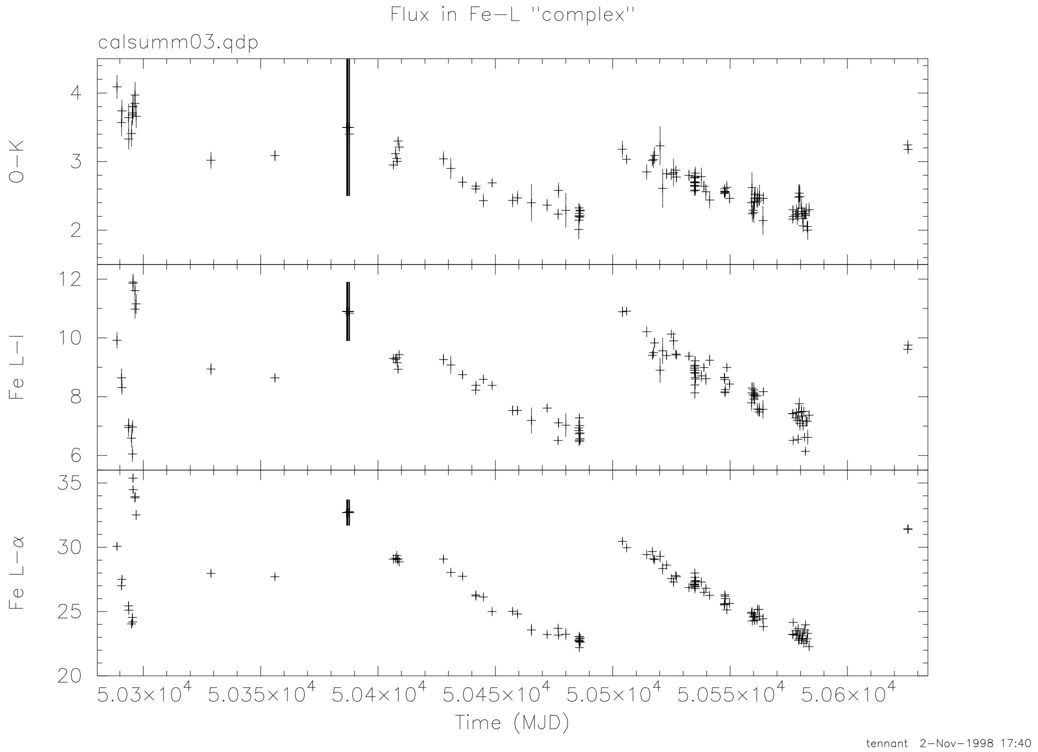

Figure 36: Temporal dependence of modeled line strengths for the Fe-L and O-K complex of lines.

4.2 Procedures

To fit the PHA spectra, we employed a model defined with the following PLT/COD function, using line energies from Reference [18]:

```
! calsp03.cod, Used to fit 244 Cm SSD calibration spectra.
!**********************************************************************
! 1998-10-25 Include both Ge K escape lines
! 1998-10-22 Add Pu Lb2, Lb5 and Lb4 lines
! 1998-08-12 Include Fe a2 in model, and average energies for K and Cr.
!**********************************************************************
! P1,P2 gain offset slope
! P3,P4 resolution parameters
! p5  norm of O K
! p6  norm of Fe LIII-l
! p7  norm of Fe LIII-alpha
! Line energies:
VAR eOK        524.9 eOK     STO
VAR eFeL3l     615.2 eFeL3l  STO
VAR eFeL2e     628.  eFeL2e  STO
VAR eFeL3a     705.0 eFeL3a  STO
VAR eFeL2b1    718.5 eFeL2b1 STO
VAR eFeL1b3    792.  eFeL1b3 STO
VAR eAlKa     1486.6 eAlKa   STO
VAR eKKa      3312.9 eKKa    STO
VAR eCrKa     5411.7 eCrKa   STO
VAR eFeKa2    6390.84 eFeKa2 STO
VAR eFeKa1    6403.84 eFeKa1 STO
VAR eFeKb1    7058.0 eFeKb1  STO
!VAR eFeKb2    7108.1 eFeKb2  STO
!VAR eNiKa1    7460   eNiKa1  STO
!VAR ePbLa2   10449.5 ePbLa2  STO
!VAR ePbLa1   10551.5 ePbLa1  STO
VAR ePuLa2   14084.2 ePuLa2  STO
VAR ePuLa1   14278.6 ePuLa1  STO
VAR ePuLe    16333   ePuLe   STO
VAR ePuLb6   16498.3 ePuLb6  STO
VAR ePuLb2   17255.3 ePuLb2  STO
VAR ePuLb4   17556.0 ePuLb4  STO
VAR ePuLb7   17705.0 ePuLb7  STO
VAR ePuLb5   17950.6 ePuLb5  STO
VAR ePuLb1   18293.7 ePuLb1  STO
VAR ePuLb3   18540.5 ePuLb3  STO
VAR ePuLg1   21417.3 ePuLg1  STO
!VAR ePuLg2   21725.1 ePuLg2  STO
VAR ePuLg3   21982.4 ePuLg3  STO
VAR ePuLg6   22150.2 ePuLg6  STO
! Ge K edge is at 11.104
VAR eGeKa2    9855.3 eGeKa2  STO
VAR eGeKa1    9886.4 eGeKa1  STO
! Best single escape energy is about 2/3's of distance from K-a2 to K-a1.
!VAR eGeKesc   9874.  eGeKesc  STO
!VAR eGeLesc   1090.  eGeLesc  STO
! General variable
var Energy
```

```
!*********************************************************************
! Subroutines:
! push channel on stack, return the Energy
! Assumes E=p1+chan*p2
: gain
p2 * p1 +
;
!*************
! Returns gaussian, push norm, width, energy onto stack
: ngaus
Energy RCL - over / dup * 2 / neg exp swap / * 2.50663 / P2 *
;
!*************
! Assume Energy is on stack, return SSD resolution
! Uses sigma = SQRT(P4*E+P3)
: ssdres  P4 * P3 + SQRT ;
!*********************************************************************
: calsp
x gain Energy STO
0.0
 P5  eOK     RCL DUP ssdres SWAP ngaus +
 P6  eFeL3l  RCL DUP ssdres SWAP ngaus +
 P7  eFeL3a  RCL DUP ssdres SWAP ngaus +
 P8  eAlKa   RCL DUP ssdres SWAP ngaus +
 P9  eKKa    RCL DUP ssdres SWAP ngaus +
P10  eCrKa   RCL DUP ssdres SWAP ngaus +
P11  eFeKa2  RCL DUP ssdres SWAP ngaus .33333 * +
P11  eFeKa1  RCL DUP ssdres SWAP ngaus .66667 * +
P12  eFeKb1  RCL DUP ssdres SWAP ngaus +
P13  ePuLa2  RCL DUP ssdres SWAP ngaus +
P14  ePuLa1  RCL DUP ssdres SWAP ngaus +
P15  ePuLe   RCL DUP ssdres SWAP ngaus +
P16  ePuLb6  RCL DUP ssdres SWAP ngaus +
P17  ePuLb2  RCL DUP ssdres SWAP ngaus +
P18  ePuLb4  RCL DUP ssdres SWAP ngaus +
P19  ePuLb7  RCL DUP ssdres SWAP ngaus +
P20  ePuLb5  RCL DUP ssdres SWAP ngaus +
P21  ePuLb1  RCL DUP ssdres SWAP ngaus +
P22  ePuLb3  RCL DUP ssdres SWAP ngaus +
P23  ePuLa2  RCL eGeKa1 RCL - DUP ssdres SWAP ngaus .66667 * +
P23  ePuLa2  RCL eGeKa2 RCL - DUP ssdres SWAP ngaus .33333 * +
P24  ePuLa1  RCL eGeKa1 RCL - DUP ssdres SWAP ngaus .66667 * +
P24  ePuLa1  RCL eGeKa2 RCL - DUP ssdres SWAP ngaus .33333 * +
P25  ePuLe   RCL eGeKa1 RCL - DUP ssdres SWAP ngaus .66667 * +
P25  ePuLe   RCL eGeKa2 RCL - DUP ssdres SWAP ngaus .33333 * +
P26  ePuLb6  RCL eGeKa1 RCL - DUP ssdres SWAP ngaus .66667 * +
P26  ePuLb6  RCL eGeKa2 RCL - DUP ssdres SWAP ngaus .33333 * +
P27  ePuLb2  RCL eGeKa1 RCL - DUP ssdres SWAP ngaus .66667 * +
P27  ePuLb2  RCL eGeKa2 RCL - DUP ssdres SWAP ngaus .33333 * +
P28  ePuLb5  RCL eGeKa1 RCL - DUP ssdres SWAP ngaus .66667 * +
P28  ePuLb5  RCL eGeKa2 RCL - DUP ssdres SWAP ngaus .33333 * +
P29  ePuLb1  RCL eGeKa1 RCL - DUP ssdres SWAP ngaus .66667 * +
P29  ePuLb1  RCL eGeKa2 RCL - DUP ssdres SWAP ngaus .33333 * +
P30  ePuLg1  RCL eGeKa1 RCL - DUP ssdres SWAP ngaus .66667 * +
```

```
P30  ePuLg1  RCL eGeKa2 RCL - DUP ssdres SWAP ngaus .33333 * +
P31  ePuLg3  RCL eGeKa1 RCL - DUP ssdres SWAP ngaus .66667 * +
P31  ePuLg3  RCL eGeKa2 RCL - DUP ssdres SWAP ngaus .33333 * +
P32  ePuLg6  RCL eGeKa1 RCL - DUP ssdres SWAP ngaus .66667 * +
P32  ePuLg6  RCL eGeKa2 RCL - DUP ssdres SWAP ngaus .33333 * +
! Pulser parameters (ngaus in channel space)
P35 P34 P33 X - over / dup * 2 / neg exp swap / * 2.50663 /  +
! Line at specified energy
!P37  P36         DUP ssdres SWAP ngaus +
;
```

Figures 37 through 41 display sample ^{244}Cm spectra, with line identifications.

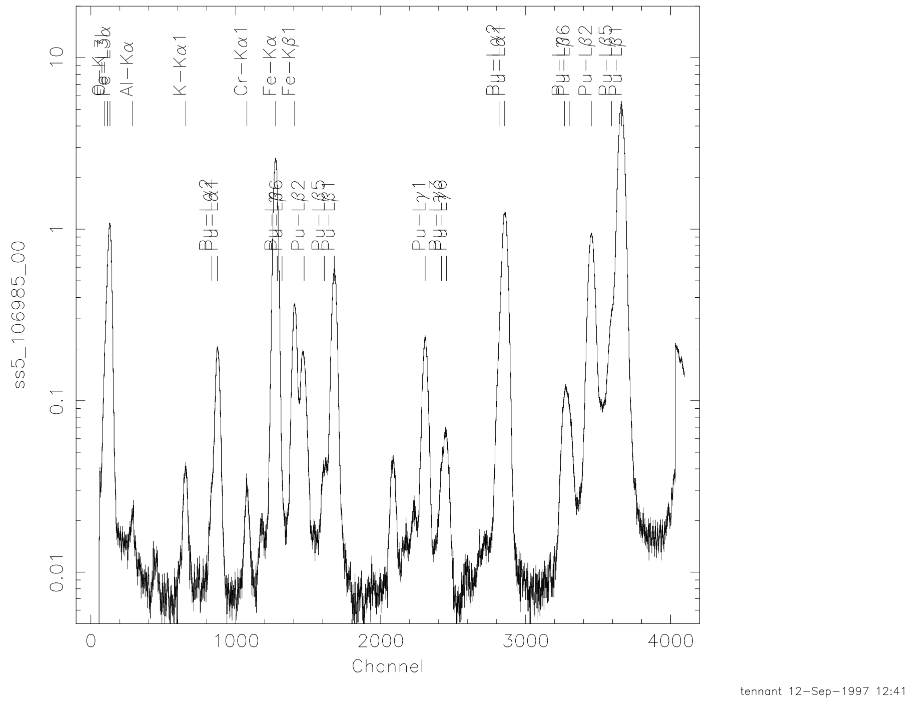

Figure 37: Spectrum of ^{244}Cm source obtained with SSD_5.

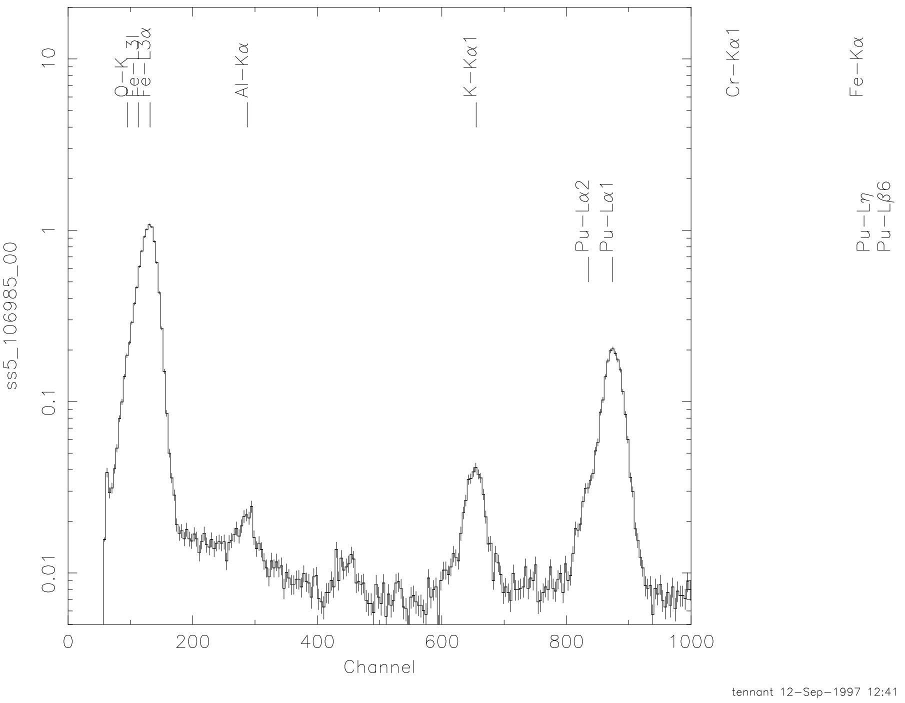

Figure 38: Low-energy spectrum of ^{244}Cm source obtained with SSD_5.

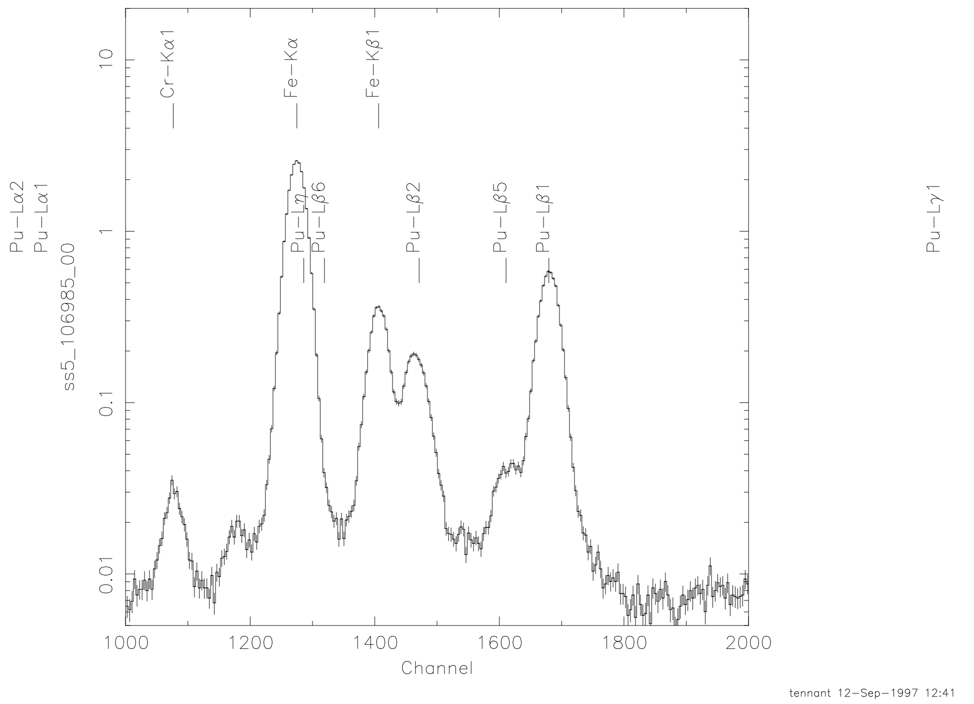

Figure 39: Spectrum near Fe-K lines of ^{244}Cm source obtained with SSD_5.

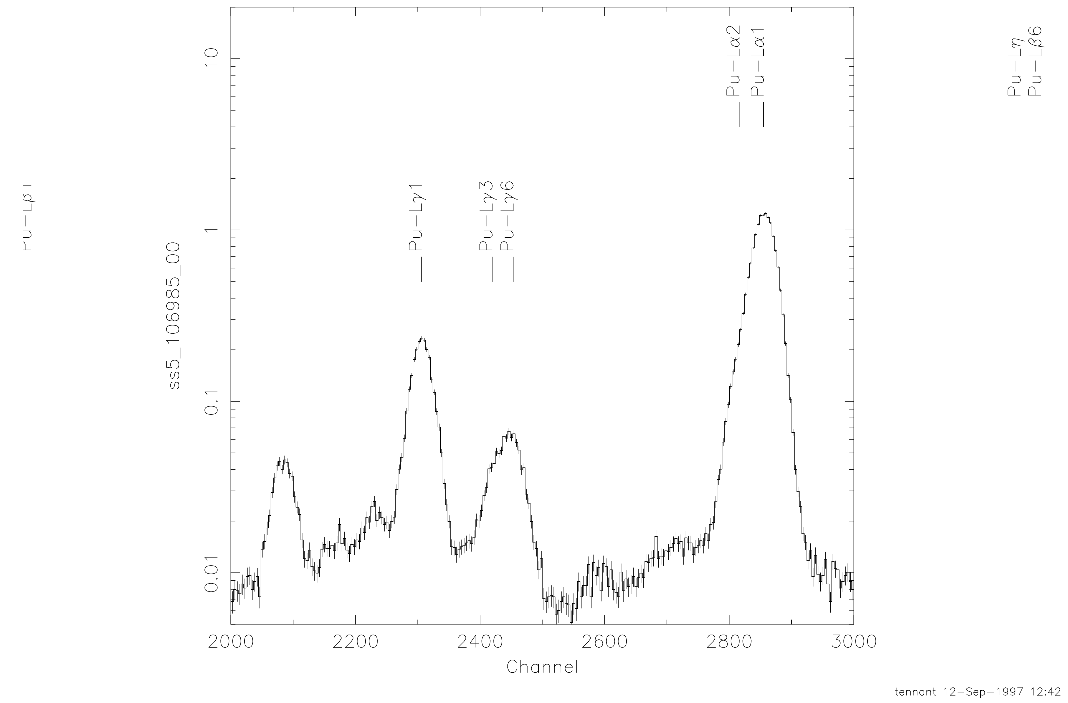

Figure 40: Medium-energy spectrum of ^{244}Cm source obtained with SSD_5.

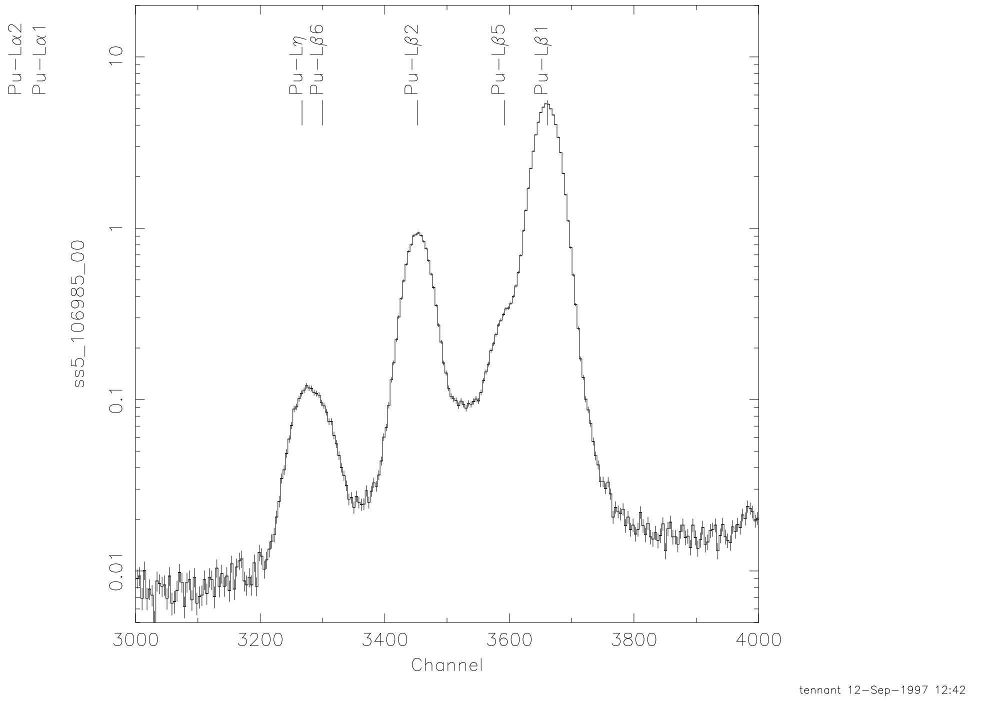

Figure 41: High-energy spectrum of ^{244}Cm source obtained with SSD_5.

4.3 Status

The most recent version, dated 1998-11-02, is currently in the QDP file `calsumm03.qdp`.

Since the Preliminary Calibration Report, we have imnplemented the following improvements in the model:

1. The Fe K-alpha line is now modeled as two lines with the line at the alpha-2 energy fixed to be half the flux of the line at alpha-1. The weaker K lines (from Cr, K, and Al) are still modeled as single line but at the flux weighted average energy. These changes cause a minor change to the gain and offset parameters.

2. The Pu L beta-4 and beta-7 lines have been added which fills in the gap between the beta-1 and beta-2 lines. For completeness the beta-3 line was also added. This tends to make the beta lines slightly narrower and since the beta lines occur at the highest energies, the net effect is to reduce the fano factor slightly. It is likely that there is a slight shelf/tail that the new lines partially fill in, and hence these lines are filling in more than they should.

3. The Ge escape lines are modeled with two lines, with energies corresponding to the Ge K alpha-1 and K alpha-2, with the alpha-2 strength fixed at half the alpha-1 level. Previously only a single escape energy was used at the flux weighted average energy. Other than burning up more computer time, this change had little impact on the model parameters.

4. All fits are now done using the likelihood statistic.

5. Most spectra are fit in the channel range 71 to 4000. During the period from MJD 50350 to 50432 when the gain parameter was near 5.28 eV/chan the channnel range was changed to 67 to 3750. Thus all spectra are now fit over approximately the same energy range.

Although the original model with the above refinements account for a large fraction of the spectrum, it is worth noting that there are still unexplained and unmodeled features. The remainining problems are these:

1. The most serious problem is that there is an unidentified feature between the Fe K-beta and the Ge K escape line from Pu L beta-1. Since this feature is blended with lines in the model, the fitting routine will adjust the model paremeters to attempt to fill in this feature. This will slightly bias the energy scale and resolution parameters.

2. The most obvious problem (but one that has little impact on the fit parameters) is there is an unmodeled line near channel 2100. This line is consistent with Pb L alpha-2 energy but inconsistent with alpha-1 and therefore remains unidentified. Since there are no lines in the model near this feature, the only impact to bias the background level.

3. The pulser amplitude was changed a few times but often seemed to land on top of an existing line. I've seen the pulser blended with the O K line, Fe K, and the Ge escape from Pu L gamma-3. This last location is the most common location for the pulser at XRCF. Although the Pu line is weak the fitting routine is free to (and does!) trade flux between the Pu gamma line and the pulser. This of course increases the uncertainties of both features.

4. There is a continuum present which is at least partly due to unresolved lines and the unmodeled shelf/tail components of existing lines. Currently the continuum is modeled with a low energy exponential and a constant term. This is a rather poor model, but since the continuum is weak and does not vary much in time, should not represent a major problem. The error in the continuum rate is less than 0.01 ct/sec/channel which implies that absolute line fluxes can be in error by 0.4 ct/sec. Of course the relative errors from one spectrum to another will be smaller.

4.4 Data products

Currently, the data products for analysis of the SSD_5 internal calibration data are the QDP files `calsumm03.qdp` and `calsumm03.pco`. The latter (optional) file contains useful labels and a sensible default starting plot.

5 SSD continuum measurements

5.1 Effective area

5.1.1 Objectives

For calibrating the effective area, there are two complementary approaches:

1. Use a monochromatic source with no constraints on the detector's spectral resolution. Low-spectral-resolution detectors are adequate for this approach. However, it requires knowledge of the source's spectral purity (because a real source is not totally monochromatic) and samples only at discrete energies (thus requiring a model or interpolating scheme to span the spectral range).

2. Employ a continuum source with a detector having adequate spectral resolution. This approach simultaneously samples the entire spectrum at a spectral resolution proportionate to that of the detector. However, it requires knowledge of the detector's response matrix (because a real detector does not have a delta-distribution response).

5.1.2 Procedures

In principle, the methodology for calibrating effective area is straightforward. Expose two identical detectors, one a beam-normalization detector and the other a focal-plane detector at the focus of the optic, to a uniform beam of radiation. At a photon energy E, the effective area $A_{\rm eff}(E)$ of the optic's limiting aperture is approximately the following:

$$A_{\rm eff}(E) \approx \frac{C_{\rm fpd}(E) D_{\rm optic}^2}{C_{\rm bnd}(E) D_{\rm bnd}^2} A_{\rm bnd} \ . \tag{19}$$

Here, $C_{\rm fpd}(E)$ and $C_{\rm bnd}(E)$ are, respectively, the count rates (at energy E) in the focal-plane detector and the beam-normalization detector; $D_{\rm optic}$ and $D_{\rm bnd}$, the distances to the optic and BND; and $A_{\rm bnd}$, the area of the BND's aperture. Ideally, this approach would not need calibrated detectors, because the efficiencies of the *identical* detectors cancel in the count-rate ratio: Only the distance ratio and the area of the beam-normalization detector's aperture require absolute calibration. Of course, the accuracy of this approximation (Eq. 19) depends on the extent to which the detectors' response matrices are identical (or cross-calibrated) and upon knowledge of the beam's uniformity. Furthermore, the approximation is accurate only if (a) the radiation is spectrally pure or (b) the detector's spectral resolving power is high.

The ultimate calibration of the absolute effective area will not use the simple ratio in Equation 19. Instead, parameter optimization through forward fitting measured pulse-height-amplitude (PHA) spectra with simulated spectra will determine the effective area. *The model is the calibration.*

Here we use Equation 19 for a preliminary calibration of the effective area of HRMA mirror shells, using measurements of continuum spectra with the HXDS's BND and focal-plane SSDs — SSD_5 and SSD_X. For these effective-area measurements, the EIPS (§1.1.1) served as an x-ray-continuum source, with a C target at 15 kV and a Be transmission filter. Because the detectors' gains are not perfectly matched, it is necessary to fine-tune the energy scale: The presence of weak lines facilitates this minor adjustment, made before taking the ratio of the PHA spectra.

Figure 42 exemplifies data used for shell 6. To the extent that SSD_5 and SSD_X are identical, the shell-6 effective area at the XRCF is simply the ratio of the SSD_X PHA spectrum to that of the SSD_5, appropriately scaled for distance ratio and BND's aperture (Eq. 19). Figure 43 summarizes the results for all 4 HRMA shells. One of the great advantages of this approach is apparent: A single measurement determines the effective area at all energies above about 1 keV, at the spectral resolution of the SSDs. Below about 1 keV, the data are unreliable, owing to a steep decline in SSD efficiency and to expected differences between SSD efficiencies resulting from slightly different windows and from differential accumulation of ice on the SSD windows.

To predict the effective area of each HRMA shell at the XRCF, we employ the MSFC Project Science ray-trace code. This code includes thermal pre- and post-collimators, central aperture plate, and as-built mirror element and shell parameters (SAO/ T. Gaetz, private communication), but no figure-error or

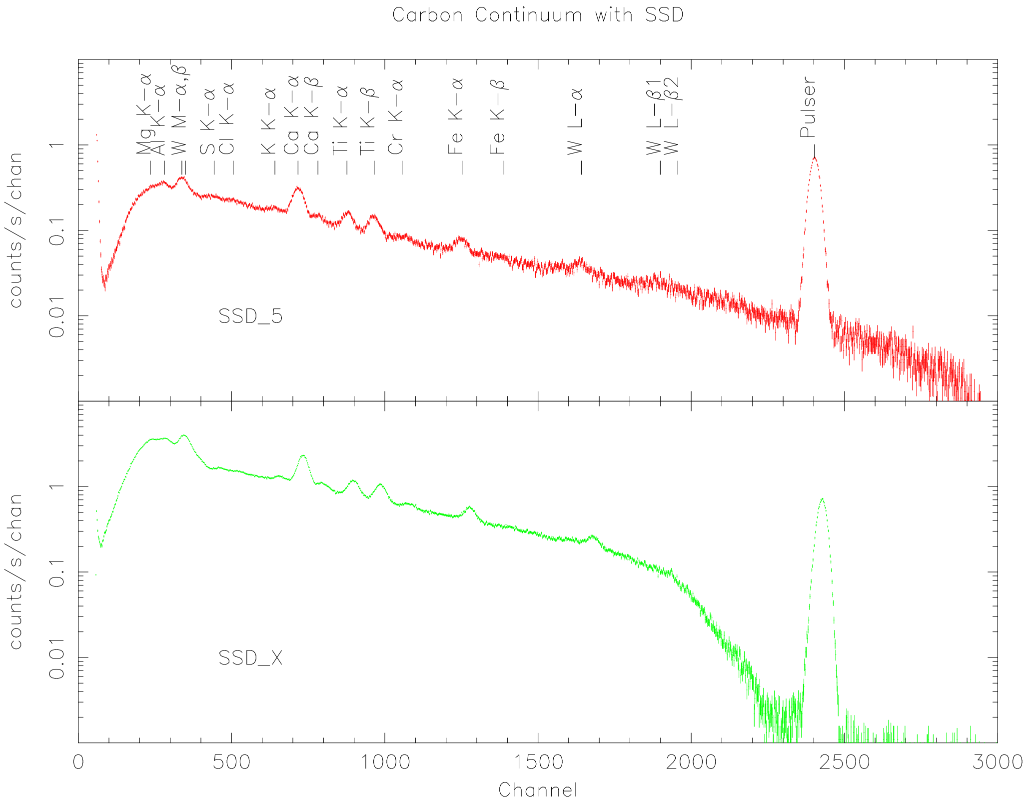

Figure 42: SSD-measured spectra for a carbon target at 15 kV, exhibits a smooth continuum with some relatively weak, atomic fluorescence lines from contaminants in the target. Top panel is the pulse-height-amplitude (PHA) spectrum for SSD_5; bottom, the PHA spectrum for SSD_X at the focal plane of shell 6. Each PHA spectrum shows the pulser (near channel 2400); the bottom one also displays a discrete drop at the (iridium) Ir-M_V edge (near channel 400) and a roll-over at the critical energy (near channel 2000) for the mirror-shell's mean grazing angle. (The energy scale is approximately 5 eV per channel.)

surface-roughness effects. Using a Monte-Carlo simulation, it records the position and direction of each ray at the nominal focal plane, plus the grazing angle upon reflection at each mirror surface. In post processing, a second program calculates the reflectance at each interface, for each ray stored during the Monte-Carlo simulation, using the optical constants of the mirror coating (iridium). Above 2 keV, we use constants [19] derived from synchrotron studies [20, 21] (SAO/ D. Graessle, private communication); below 2 keV, we employ tabulated values [17] (see `http://www-cxro.lbl.gov/optical_constants`). Away from edges, the synchrotron data reproduce the Henke et al. [17] data above 2 keV, after adjusting the latter to an iridium density of 0.9725 bulk. Thus, the reflectance computations below 2 keV assume this density for a uniform iridium coating. The MSFC code gives effective-area results in agreement with those from the independent SAO ray-trace model (SAO/ D. Jerius, private communication).

To compare with the effective area empirically determined through continuum measurements with the SSDs, we next convolve the ray-trace-model effective areas with a gaussian of 0.21 keV Full-Width at Half-Maximum (FWHM), representative of the SSD's spectral resolution. Furthermore, because the focal-plane SSD measurements employed a 2-mm-diameter aperture, we decrease the predicted effective areas (over the entire focal plane) by the expected fraction of flux scattered outside the aperture. To calculate this fraction, we use the spatial power spectral densities, determined from pre-coating metrology, averaged over axial and azimuthal position for each mirror (SAO/ T. Gaetz, private communication). For shells 3, 4 and 6, this procedure gives excluded flux fractions similar to those predicted by the SAO

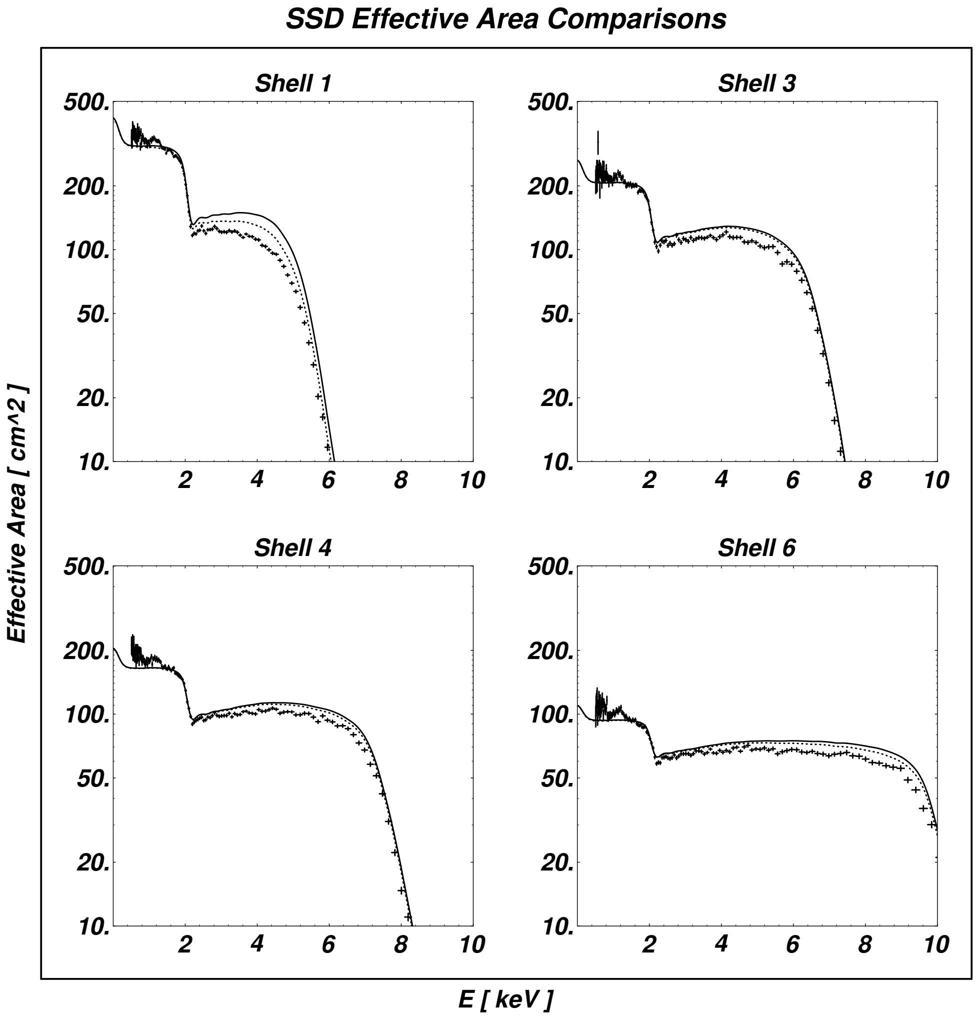

Figure 43: Comparison of measured with predicted effective area of each HRMA shell shows a discrepancy of about 10%. Data are the quotient of the focal-plane detector's pulse-height-amplitude (PHA) spectrum by the corresponding beam-normalization detector's PHA spectrum, scaled by the distance-ratio squared and the BND's aperture area. The solid line denotes the model prediction for the effective area over the entire focal plane; the dotted, over a 2-mm-diameter (40-arcsec) focal-plane aperture.

scattering model (SAO/ D. Jerius, private communication). However, for shell 1 this procedure predicts an excluded flux fraction that rises more sharply with energy than that predicted by the SAO model.

Even after the correction for scattering, the predicted effective areas exceed the SSD-measured values (Fig. 43) by about 10%. These results are preliminary: A full analysis awaits complete characterization of the SSD response and completion of the SAO synchrotron reflectivity program [20]. In addition, we are exploring the consequences of lower iridium densities [22], finite thickness for the iridium and (binding-layer) chromium coatings (unimportant at or below the critical energy), density gradients at the surface of the iridium layer, and surface roughness. We shall also include effects due to molecular [23, 24] or particulate [25, 26] contamination; however, based on AXAF's very stringent contamination-control program and analyses of optical witness samples, we do not expect these effects to be significant.

5.1.3 Status

Owing to the extensive analyses of the continuum data performed by the MST, we have not updated our contribution from the Preliminary Report. However, we intend to repeat the analysis using information from the SSD calibration at BESSY and performing a forward-modeling analysis on the carbon continuum data.

5.1.4 Data products

Figure 43 shows both measured and predicted results. Corresponding data will be accessible from the Project Science Calibration web page `http://wwwastro.msfc.nasa.gov/xray/xraycal/cat.html`.

5.2 Alignment

5.2.1 Objectives

Five ground-support actuators provide fine positioning of the HRMA (§1.1.3) in the XRCF Instrument Chamber (IC): The specified precision for controlling pitch and yaw is 10 arcsec. A laser system enables initial alignment of the HRMA Alignment Reference Mirror (ARM) to the XRCF Facility Optical Axis (FOA), to a tolerance of 10 arcsec. Although the HRMA's effective area and point-response function are insensitive to misalignment on these scales, it is nonetheless necessary to verify the alignment in x rays, particularly for examining off-axis effects. Here, we describe an effective and efficient x-ray alignment test, discuss its sensitivity, and report results of the test.

We note that x-ray verification of alignment was not routine. Initial attempts to confirm alignment, by comparing line count rates through opposite shutters, failed due to an unanticipated small decenter of each HRMA hyperboloid relative to its corresponding paraboloid. However, the x-ray-continuum alignment test, described here, is relatively insensitive to decenter, thus allowing an unequivocal verification of the HRMA's alignment to the XRCF FOA.

5.2.2 Procedures

The HRMA ground-support equipment included a shutter system, shown schematically in Figure 44, which can isolate any combination of the HRMA's 16 shell quadrants. The principal applications for the shutters were in determining best focus ("shutter focus"), in measuring paraboloid-to-hyperboloid tilt [27], and in performing subaperture measurements of the point spread function (PSF).

A very sensitive test of alignment for grazing-incidence optics is the azimuthal dependence of the critical energy at which the mirror's response plummets. Using the HRMA shutters, we determined this critical energy for each shell quadrant. To do this efficiently, we used the HXDA focal-plane SSD [5], SSD_X (§1.1.5) to measure EIPS [2] continuum radiation (§1.1.1). By comparing the SSD_X spectrum observed through one shell quadrant with that through the opposite quadrant, we establish the alignment of that shell in the plane passing through the quadrant centers. Specifically, we divide the SSD_X PHA spectrum for continuum x rays through one shell quadrant by that through the opposite quadrant.

For estimating this effect, we constructed a simple 2-dimensional model and compared it with predictions from the MSFC Project Science HRMA ray-trace code (5.1.2). Both took into account the finite source distance (528 m at the XRCF), which results in grazing angles for the paraboloid (hyperboloid) being greater (less) than the infinite-conjugate values by 3.6, 2.9, 2.5, and 1.9 arcmin (quadrant averaged) for shells 1, 3, 4, and 6, respectively). Both predict the same sensitivity dependence, which is slightly stronger than that observed. Figure 45 shows that the ratio of PHA spectra from opposite quadrants is quite sensitive to misalignment: E.g., a 1-arcmin misalignment results in a ratio of nearly 2 near the critical energy (9.9 keV for HRMA shell 6).

Figure 46 exhibits the ratio of SSD_X PHA spectra for opposing quadrants, for the other 3 HRMA shells. As shell diameter and, hence, mean grazing angle increase, the critical energy decreases and the sensitivity diminishes. Indeed, HRMA shell 1 requires a 4.5-times-larger off-axis angle than shell 6, to achieve a PHA ratio of 2. This decreased sensitivity occurs (a) because a given misalignment angle is a smaller fraction of the mean grazing angle and (b) because the grazing-angle cut off becomes less steep as the reflectance is more lossy at lower energies.

X-ray verification of HRMA alignment employed data for individual shell quadrants, at several off-axis angles. For ease of analysis, we binned SSD_X's 4096 PHA channels into blocks of 32. To normalize, we summed the SSD_5 PHA spectrum over the range 1.44–7.2 keV and then divided this into the SSD_X

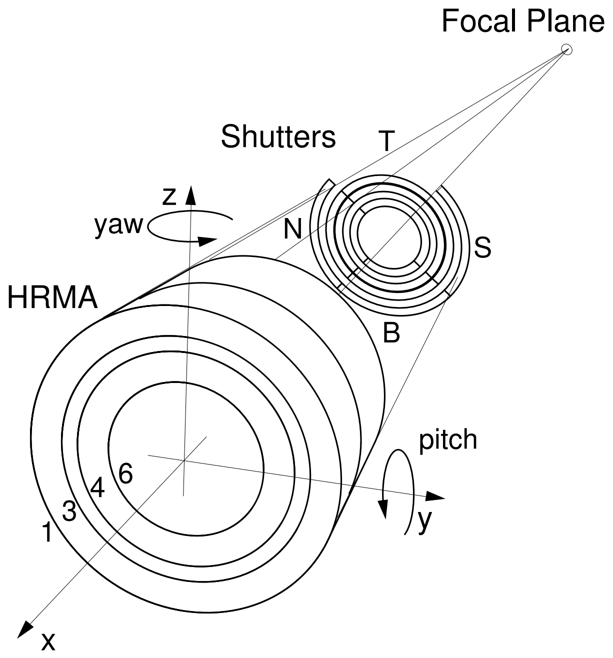

Figure 44: An assembly of 16 independent shutters isolates the converging x-ray beam of each quadrant (T=top, N=north, B=bottom, and S=south) of the HRMA's 4 mirror shells (1, 3, 4, and 6). Arrows indicate positive directions of the XRCF coordinate axes and HRMA pitch θ_y and yaw θ_z. The displayed shutter configuration has the top (T) quadrant of shell 1 open and all others closed.

PHA spectrum. Next, for a given HRMA shell and off-axis angle, we divided bin-by-bin the normalized SSD_X spectrum for one quadrant by that for the opposite quadrant. Using observed atomic lines, we monitored the SSD gain and found no significant variation.

The x-ray alignment verification probed 6 yaw and 3 pitch angles for shell 6. Figure 47 shows that the maximum PHA ratio was well above 3 at the largest yaw angle, but unity at the putative on-axis position. Figure 48 shows similar results for the pitch dependence. These results verify, in x rays, that the laser alignment of the HRMA ARM to the XRCF FOA was correct. Figure 49 exemplify results for the other HRMA shells, displaying results at the extreme yaw for each shell. The decrease in the ratio with larger shells is again consistent with expectations.

For each shell and off-axis angle, we reduced the PHA ratio to a single value, by summing over the region of interest (ROI) for which the response is most sensitive to off-axis angle — namely, 4.8–5.92, 6.24–7.36, 7.04–8.16, and 9.28–10.4 keV, for HRMA shells 1, 3, 4, and 6, respectively. In addition, we summed over a reference ROI (2.4–3.52 keV) and divided this into the sum over the sensitive ROI. Next, we divided the values for opposite quadrants to obtain a single scalar ratio for each measurement pair. Then, we performed the same manipulations for the simple model and compared the measured with model values in a scatter plot (Fig. 50). Finally, we applied a linear fit to $R_{\rm observed} = mR_{\rm model} + b$, resulting in the best-fit curve shown in the Figure 50.

The best-fit parameter values and 1-sigma errors are $m = 0.713 \pm 0.014$ and $b = 0.281 \pm 0.013$. The departure of m from unity, and b from zero indicate the simplicity of the model or the analysis and, for now, prevents this method from quantitatively determining the off-axis positioning accuracy.

The quantity $m+b$ is more interesting, because many sources of systematic errors cancel in the ratios. If the commanded on-axis position is really on-axis, then the observed ratio should be 1 as expected, constraining $m + b$ to unity as well. The best-fit value is $m + b = 0.994$, with a 95% confidence interval ranging from 0.972 to 1.016. This corresponds to a 95% confidence interval for HRMA alignment to the FOA of -2.4 to 4.1 arcsec. We thus infer that the ARM, the HRMA, and the XRCF were all aligned within this angular range when on-axis.

The χ^2 for the fit was 55.0 with 25 degrees of freedom; however, we assumed no uncertainty for the

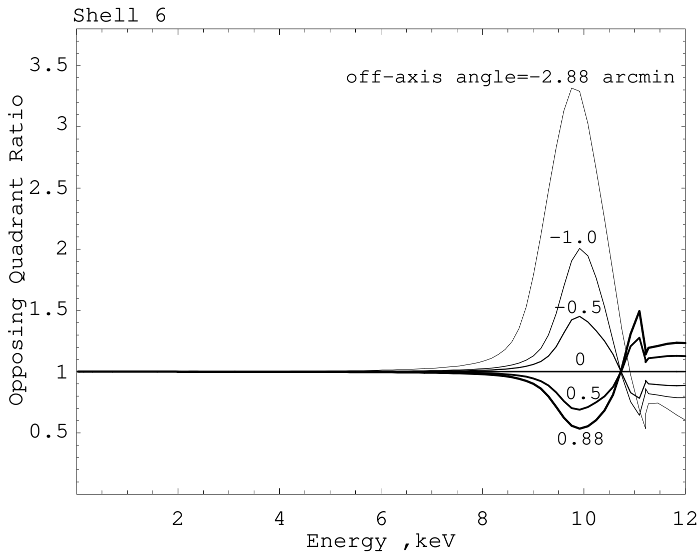

Figure 45: The ratio of quadrant throughput near the critical energy is a sensitive function of off-axis angle. This plot shows that the ratio of SSD_X PHA spectra for opposing quadrants of HRMA shell 6 can detect even relatively small (0.1 arcmin) misalignment.

commanded HRMA position. Applying the formula $\delta R = \delta\theta(dR/d\theta)$, where R is the ratio and θ is the off-axis angle, to each expected value then limits the value of $\delta\theta$. The value of $\delta\theta$ required to obtain a χ^2 which is 50% probable for a linear fit to the data in Figure 50 is 6 arcsec. Under the assumption that errors in the commanded position are the only additional source of error, the 95% confidence interval for $\delta\theta$ ranges from 2 to 11 arcsec.

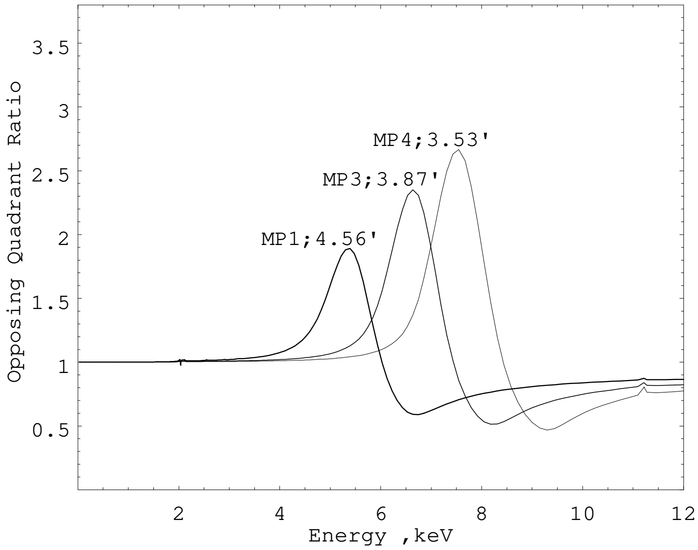

Figure 46: The sensitivity to off-axis angle, of the ratios of PHA spectra for opposing quadrants is smaller for the outer mirror shells. This plot displays expected curves for each shell's extreme off-axis measurements.

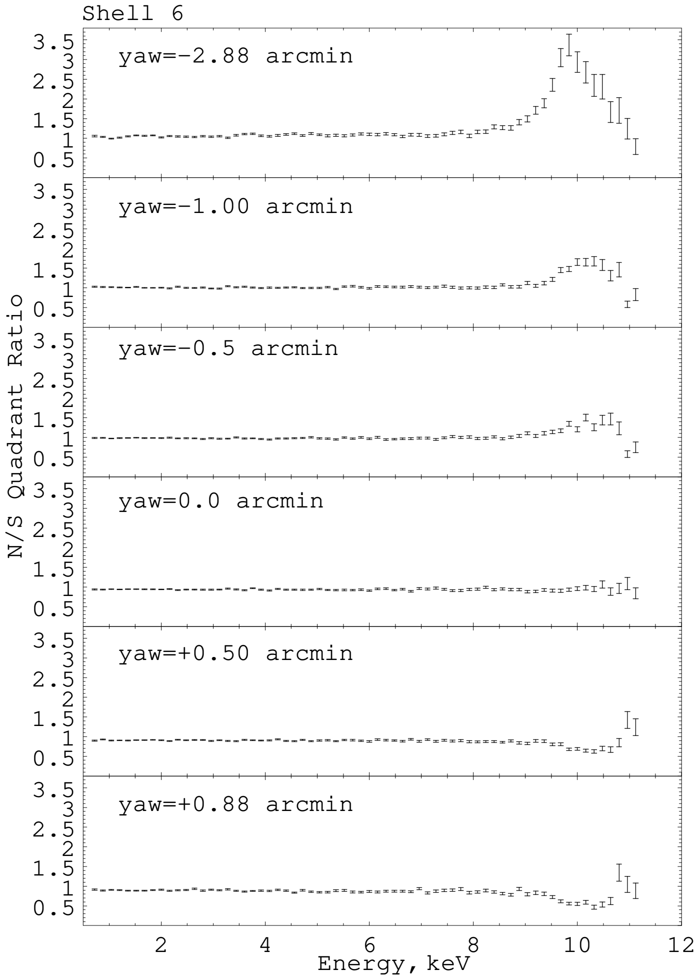

Figure 47: Ratios of normalized, binned PHA spectra for measurements with north (N) and south (S) shell-6 shutters open illustrate test's sensitivity to yaw and verify alignment of HRMA to FOA in yaw.

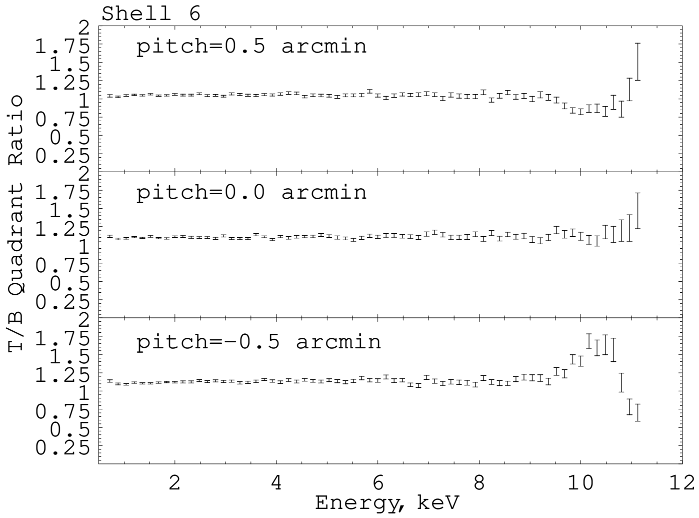

Figure 48: Ratios of normalized, binned PHA spectra for measurements with top (T) and bottom (B) shell-6 shutters open illustrate test's sensitivity to pitch and verify alignment of HRMA to FOA in pitch.

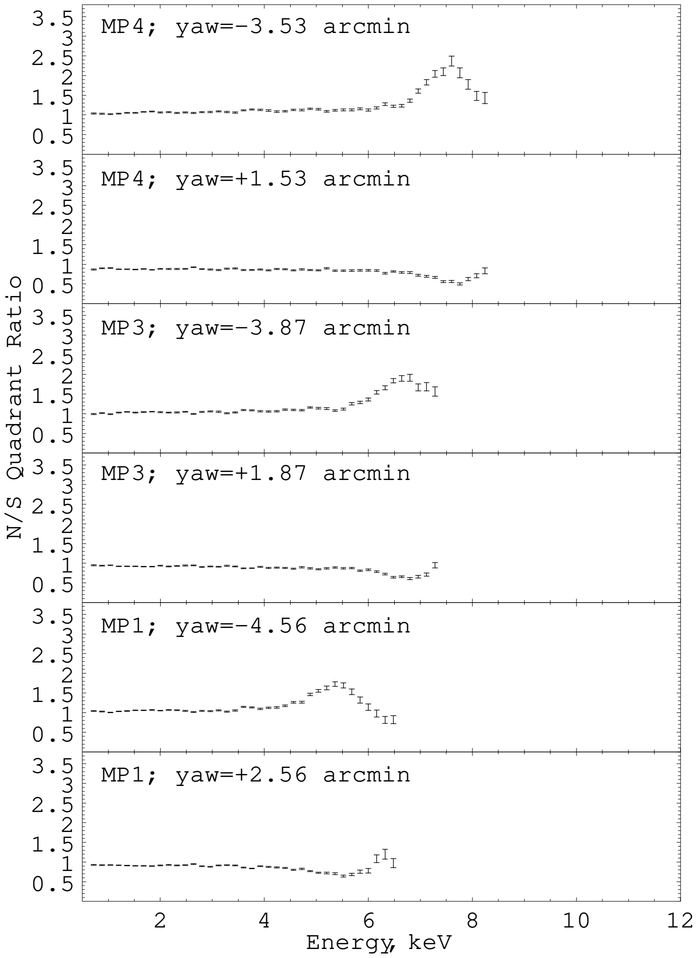

Figure 49: Ratios of normalized, binned PHA spectra for measurements with north (N) and south (S) shutters open illustrate test's sensitivity to yaw for HRMA shells 1, 3, and 4. This plot shows the PHA ratios at the extreme off-axis angles tested for each HRMA shell.

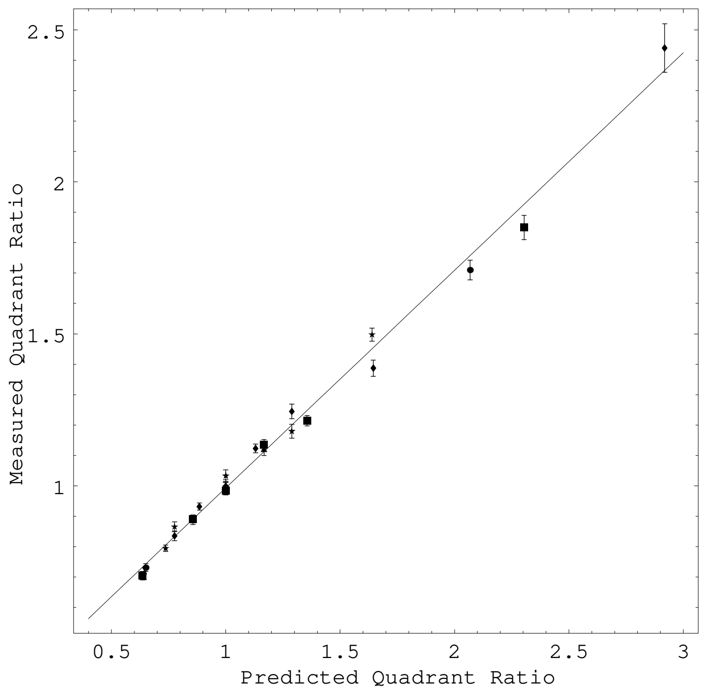

Figure 50: A comparison of measured versus fitted PHA ROI ratios, combining all measurements of pitch and of yaw, for all mirror shells, shows fair agreement with the model predictions, after scaling by about 0.7.

6 Flight Contamination Monitor

6.1 Objectives

The Advanced X-ray Astrophysics Facility (AXAF), the x-ray component of NASA's Great Observatories, underwent the most extensive, by far, system-level calibration program in the history of high-energy astrophysics at the Marshall Space Flight Center (MSFC) X-Ray Calibration Facility (XRCF) during the winter and spring of 1997 [28]. One of the key goals was to determine the absolute flux scale to an accuracy of a few percent or less, and detailed analysis of effective area measurements is continuing in order to achieve this goal for the ground calibration [29]. In addition, a high-fidelity ray trace program, maintained by the AXAF Mission Support Team and designed to model the performance of the High Resolution Mirror Assembly (HRMA) in great detail, will use the ground calibration results to predict the on-orbit performance. However, it is still important to verify the transfer of the ground-level calibration to on-orbit operation, particularly in view of the absence of any well characterized astronomical x-ray standard candles and the sensitivity of the AXAF effective area to changes in molecular (Fig. 51) and particulate contamination [3].

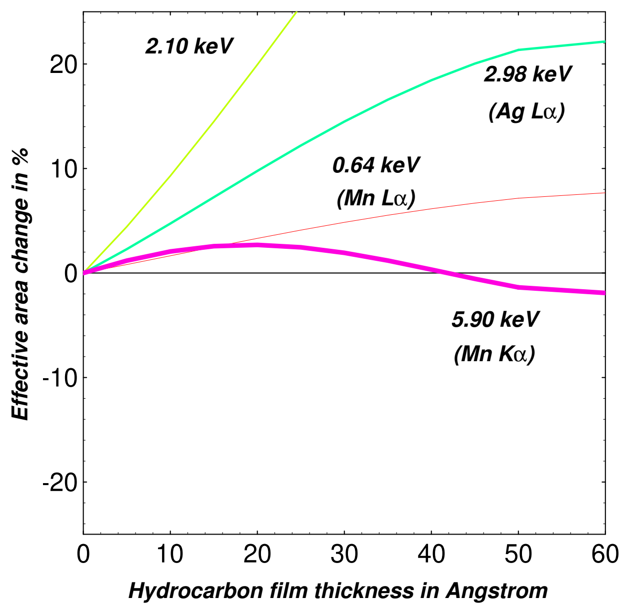

Figure 51: AXAF effective area changes in percent, at selected x-ray energies, as a function of the thickness of a uniform hydrocarbon film over 95% bulk density iridium.

For these reasons, a Flight Contamination Monitor system (FCM), made up of electron-capture radioactive sources emitting x-ray lines, is installed in the Forward Contamination Cover (FCC) of the HRMA (Fig. 52). There are four sources, spaced 90 deg apart, for each HRMA shell, with activities and radii scaled appropriately for that shell's aperture. The two objectives of the ground and in-orbit measurements using the FCM and focal plane detectors are these:

1. Verify the transfer of the HRMA flux scale from the XRCF test phase to the orbital-activation phase.

2. Measure or bound any changes in molecular contamination of the HRMA [3].

The focal plane detectors, the AXAF CCD Imaging Spectrometer (ACIS) and the High Resolution Camera (HRC), also employ their own radioactive calibration sources, in order to monitor any change in detector performance. During ground calibration FCM measurements were taken with ACIS, ACIS-2C

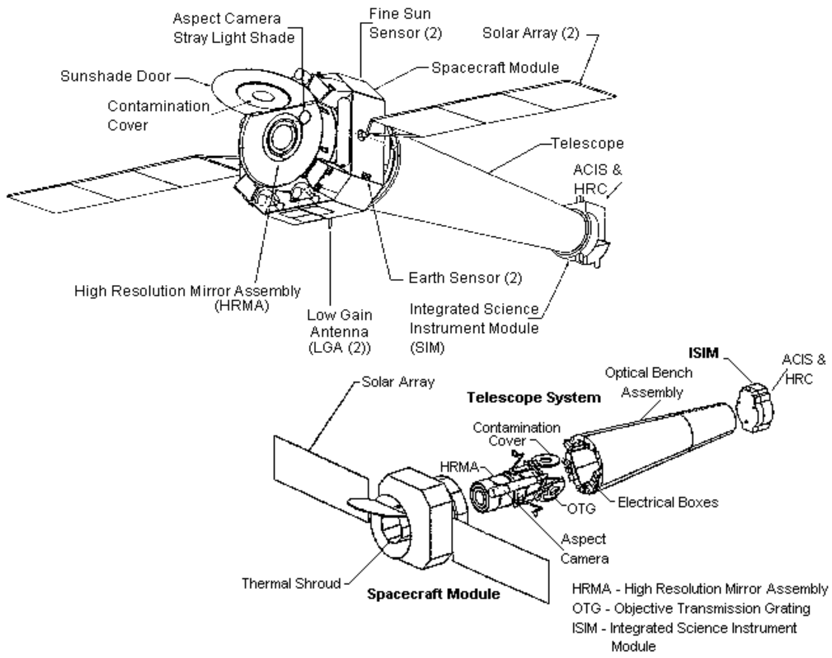

Figure 52: The AXAF spacecraft and components showing the FCC on the front of the HRMA. FCM measurements are taken during the activation phase with the FCC closed.

(an ACIS surrogate), and HRC-I (the imaging readout for HRC). The FCM measurements during the activation phase are the first look at the on-orbit HRMA/ACIS performance. Figure 53 is a schematic of the x-ray optical path for FCM measurements.

Each FCM source images the portion of the paraboloid aperture immediately in front of it, leading to an image of a slightly curved stripe in the focal plane. The FCM source 180 deg away contributes a stripe superimposed on the first one, but with a slight curvature in the opposite direction. The pair of FCM sources at 90 deg with respect to the first two contribute stripes perpendicular to the first two, leading to an image of a cross in the focal plane (Fig. 54). Although the global topology of the image is independent of energy, intensity contours depend slightly on energy due to the differing energy response of the four HRMA shells. Cross-correlation of measured and simulated images provides a measure of any FCC position shifts (§6.4).

Ideally, direct comparison of ground and on-orbit FCM measurements at as many lines as possible would provide a direct transfer of the absolute flux scale calibration from XRCF to orbit, or would provide direct measures of any discrepancies. In practise, some modelling is necessary due to possibly changing positions of the focal plane detector and the FCC relative to the HRMA, thermal contraction of the FCC on-orbit, and radioactive decay of the FCM sources. Finally, interpretation of any discrepancies with the HRMA model derived from the ground calibration requires ray trace simulations, for which we use the Project Science ray trace code (see Appendix A).

In the following subsections, we describe the characterization of the flight FCM radioactive sources (§6.2), the spectral analysis of FCM measurements taken at XRCF (§6.3), the registration analysis necessary to determine any positional shifts of the FCC relative to its nominal position (§6.4), and the continuing efforts to prepare for the FCM measurements to be taken during the activation phase after launch of the AXAF (§6.5).

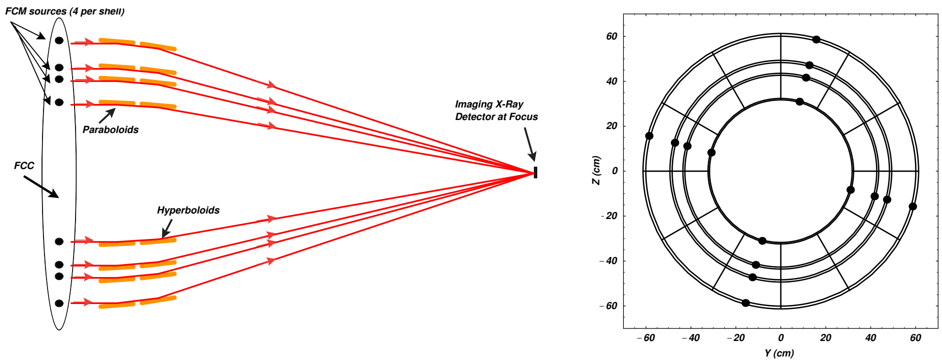

Figure 53: Left: The x-ray optical path for FCM measurements showing the FCM sources in the FCC, reflections of the paraboloids and hyperboloids of the four HRMA mirror shells, and collection by a focal plane detector (ACIS and, on the ground only, ACIS-2C and HRC-I). Right: Positions of the FCM sources projected on the paraboloid apertures midway between support struts for the baffle plates in the thermal pre-collimator, central aperture plate, and thermal post-collimator.

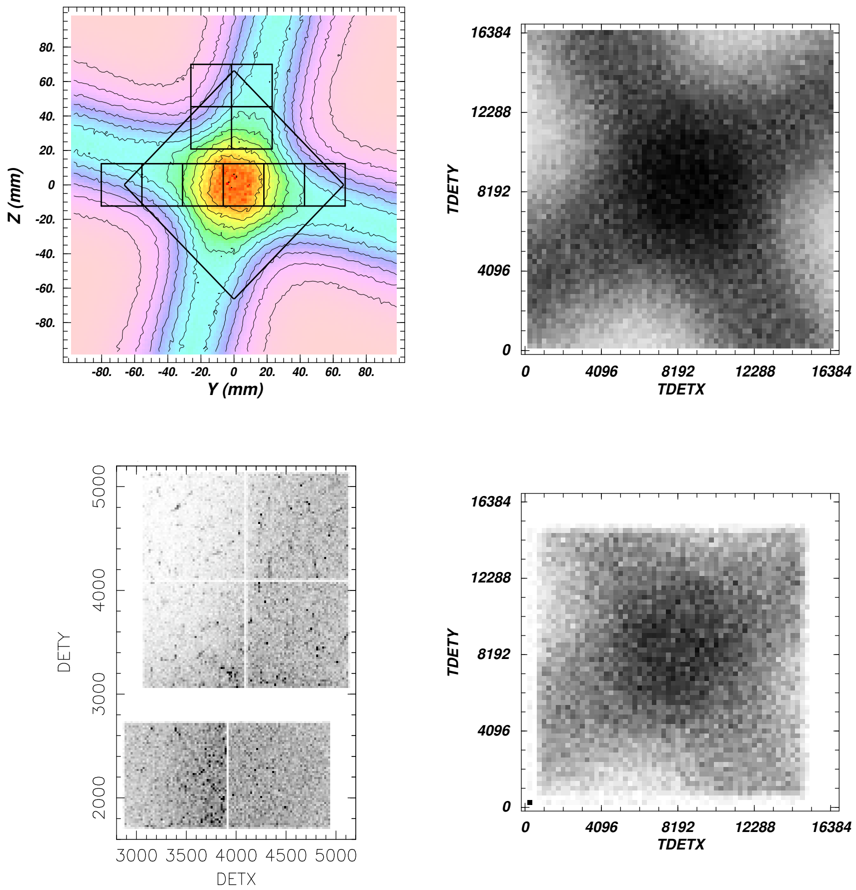

Figure 54: Simulated (top) and XRCF (bottom) FCM images. The simulated image in the top left shows the cross pattern generated in the focal plane by the FCM system, with outlines of the focal plane detectors ACIS and HRC-I superimposed. The image in the bottom left is a short ACIS exposure from XRCF. On the right are HRC-I images in HRC detector coordinates. On top is a simulation and on the bottom is an exposure from XRCF.

6.2 Radioactive sources

The FCM comprises sixteen (one per shell per quadrant) electron-capture sources positioned midway between baffle plate support struts (Fig. 53), containing ^{109}Cd and ^{55}Fe prepared at Isotope Products, Inc., packaged by MSFC, and mounted on the FCC. Due to leakage, MSFC sealed each source assembly with a 100-μm-thick Be window, eliminating the detectability and utility of the Mn Lα line at 0.64 keV. MSFC measured the individual FCM flight source activities (Table 15), with corroborating measurements by the US Army Redstone Arsenal. Dominated by systematic effects, the estimated errors in the measured absolute activities are $\sim$15%. However, activity ratios between sources, dominated by statistical uncertainties, are known with significantly higher precision (< 1 %) than the absolute activities. Statistical uncertainties (1σ) in the ^{55}Fe activities, derived from measurements of the Mn Kα line strength, range from 0.2% (shell 1) to 0.4% (shell 6). Statistical uncertainties (1σ) in the ^{109}Cd activities, derived from measurements of the Ag Kα (22 keV) line strength, range from 0.04% (shell 1) to 0.1% (shell 6). However, the lower energy ($\sim$3 keV) lines in the Ag L series are significantly affected by the overlying material in the source assemblies. The internal configuration, from the substrate up, is ^{109}Cd ($\sim$0.3 μm), a gold buffer layer ($\sim$0.05 μm), ^{55}Fe ($\sim$0.1 μm), a gold sealing layer ($\sim$0.05 μm), and finally the beryllium window (100 μm). These layers absorb $\sim$60% of the 3 keV Ag L series x-rays emitted from the ^{109}Cd. The range over which the actual layer thicknesses vary about their nominal values is unknown.

Ray trace simulations for the registration analysis (§ 6.4 below) use the activities given in Table 15. The radioactive half-lives of ^{109}Cd and ^{55}Fe are 1.2665$\pm$0.0011 and 2.73$\pm$0.03 yr [30], respectively, so compensation for radioactive decay is necessary in the data analysis.

MSFC also mapped source uniformities (Figs. 55, 56, 57 and 58). These uniformity maps are included in the ray trace simulations of the FCM sources. The uncertainty, which we assume is systematic, in the position of the uniformity map centers relative to the centers of the individual source buttons is $\pm$0.2 mm in Y and Z. The tolerance on the position of the source buttons in the source holders is $\pm$0.12 mm in Y and Z, while the tolerance on the position of the source holders on the FCC is $\pm$0.08 mm in Y and Z. Assuming these tolerances are systematic errors, the systematic uncertainty in the position of the centers of the FCMs on the FCC is $\pm$0.2 mm in Y and Z. Fig. 59 shows the measured PHA spectra for each shell 1 source, summed over its surface. PHA spectra for the other shells look very similar to these, but shifted down as the activities decrease for the inner shells.

Table 15: Nominal FCM source activities (mCi) on 1997 Mar 5* and radii (mm).

Shell	-15	75	165	255	Average	**Source radius**
1	(4.03,1.20)	(3.53,0.84)	(4.03,0.93)	(3.61,0.84)	(3.8,0.95)	4.500
3	(2.44,0.73)	(2.21,0.79)	(2.44,0.79)	(2.12,0.85)	(2.3,0.79)	3.625
4	(1.56,0.47)	(1.49,0.47)	(1.56,0.48)	(1.40,0.51)	(1.5,0.48)	3.200
6	(0.78,0.26)	(0.61,0.24)	(0.73,0.24)	(0.61,0.23)	(0.68,0.24)	2.380

* The first number is for ^{109}Cd and the second for ^{55}Fe.

MSFC used Monte-Carlo simulation of the source assemblies to determine fluxes in the forward direction. Predicted absolute fluxes for electron-capture lines are no more accurate than the absolute activity measurements, but relative fluxes should be as accurate as the tabulated branching ratios - a few % [30]. Predicted fluxes, absolute or relative, for fluorescent lines produced in the assemblies (primarily by the Ag Kα line at 22 keV) are much less secure due to the complexity of the simulations and the number of interaction pathways.

<placeholder>

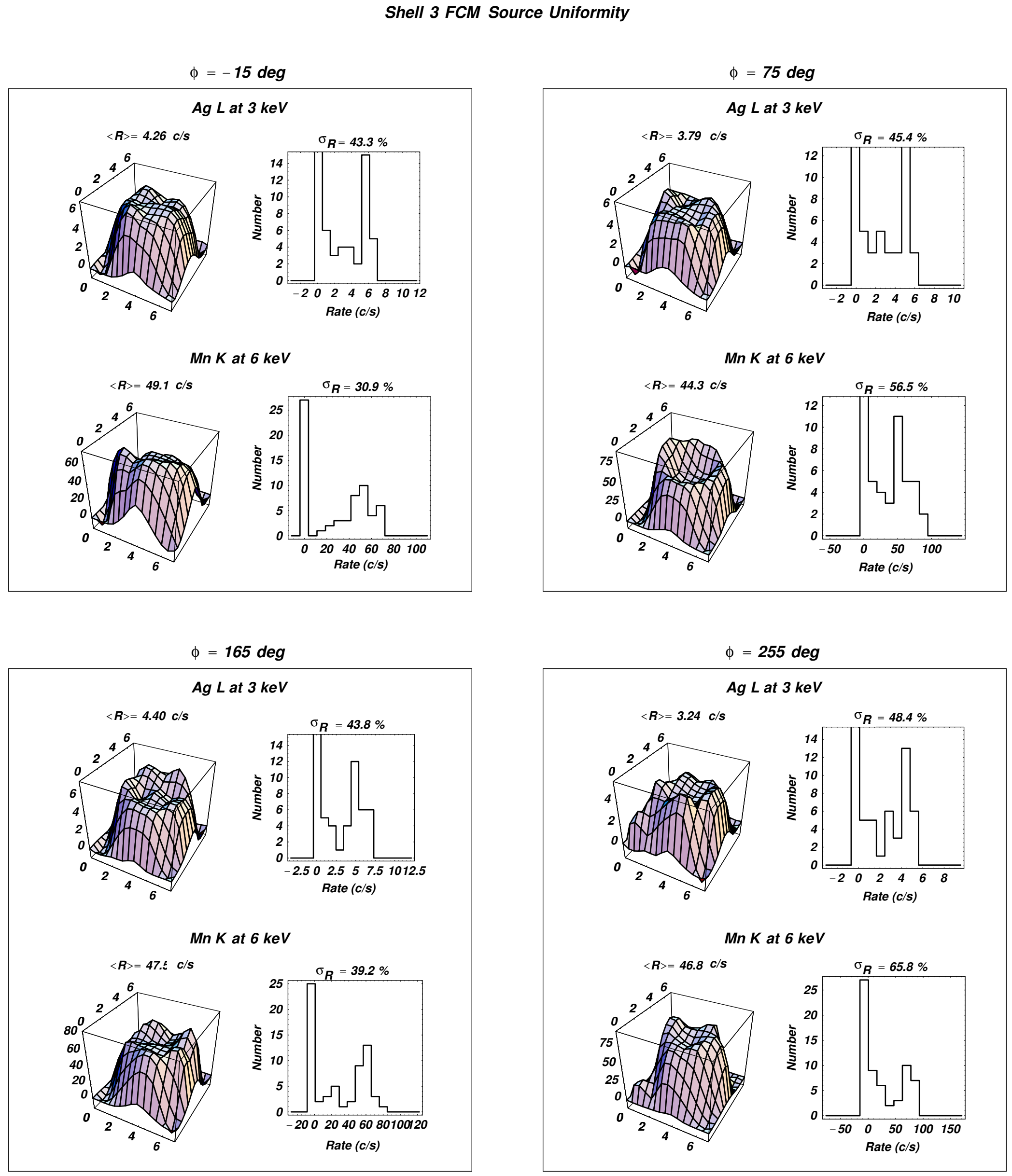

Figure 56: Uniformity measurements for the shell 3 FCM sources at each of the 4 azimuths. Within each panel are uniformity results at 3 keV (top, ^{109}Cd source) and 6 keV (bottom, ^{55}Fe source). At each energy are a surface plot of rate (left, and a histogram of rates (right). $< R >$ is the mean rate in c/s and σ_R is the rms dispersion about $< R >$ in %. These measurements were made with a CZT detector and a 1 mm diameter pinhole.

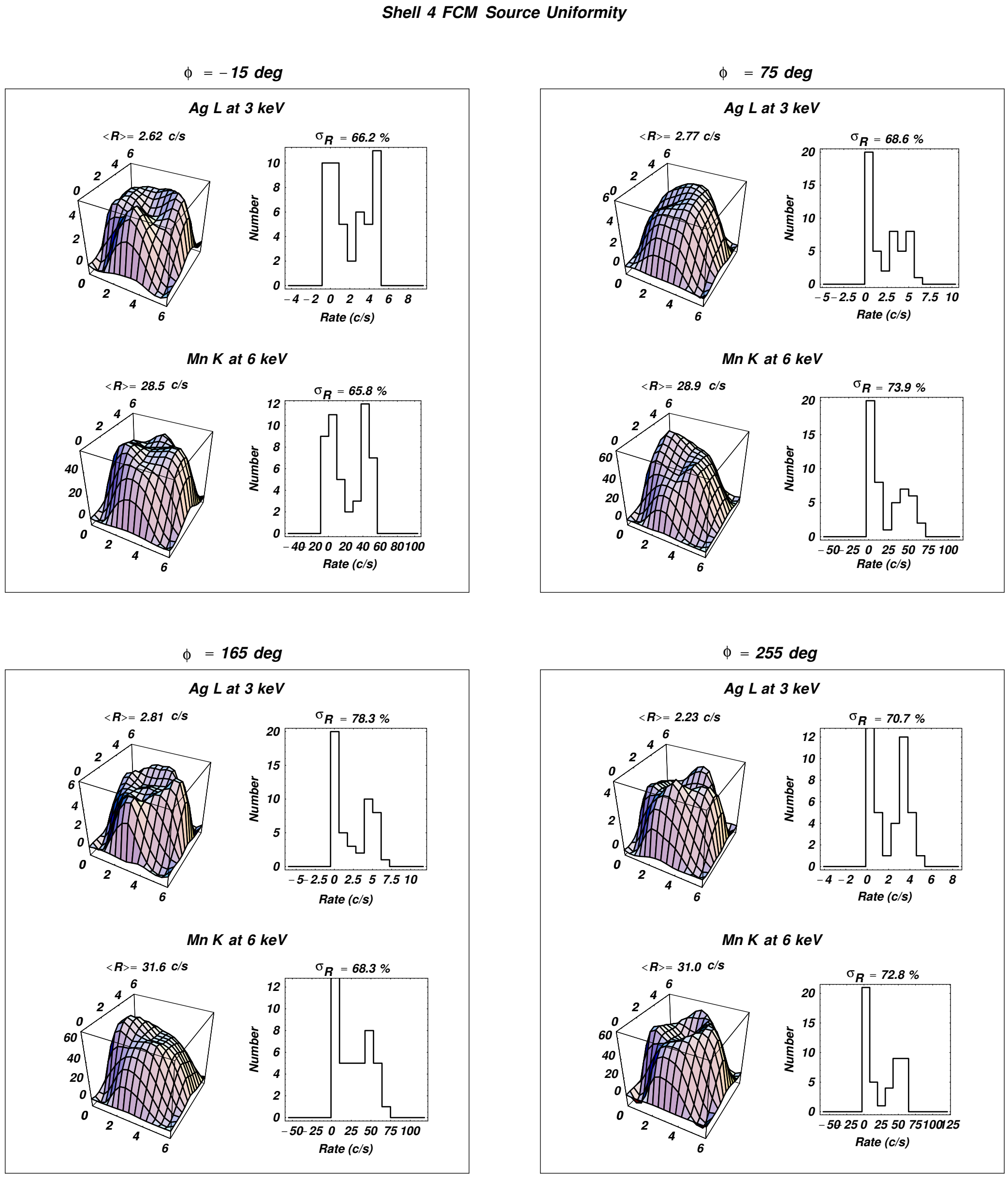

Figure 57: Uniformity measurements for the shell 4 FCM sources at each of the 4 azimuths. Within each panel are uniformity results at 3 keV (top, ^{109}Cd source) and 6 keV (bottom, ^{55}Fe source). At each energy are a surface plot of rate (left, and a histogram of rates (right). $< R >$ is the mean rate in c/s and σ_R is the rms dispersion about $< R >$ in %. These measurements were made with a CZT detector and a 1 mm diameter pinhole.

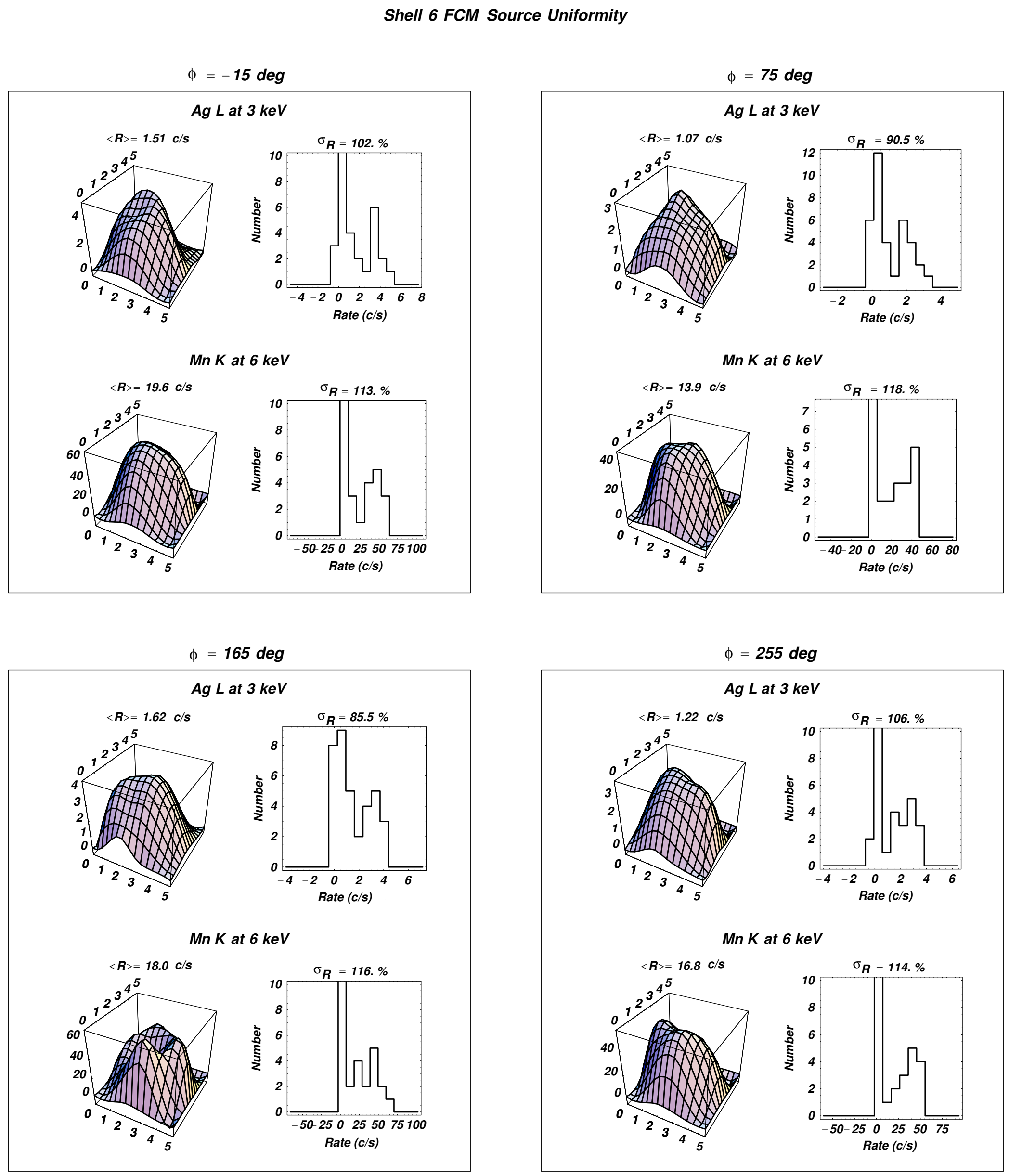

Figure 58: Uniformity measurements for the shell 6 FCM sources at each of the 4 azimuths. Within each panel are uniformity results at 3 keV (top, ^{109}Cd source) and 6 keV (bottom, ^{55}Fe source). At each energy are a surface plot of rate (left, and a histogram of rates (right). $< R >$ is the mean rate in c/s and σ_R is the rms dispersion about $< R >$ in %. These measurements were made with a CZT detector and a 1 mm diameter pinhole.

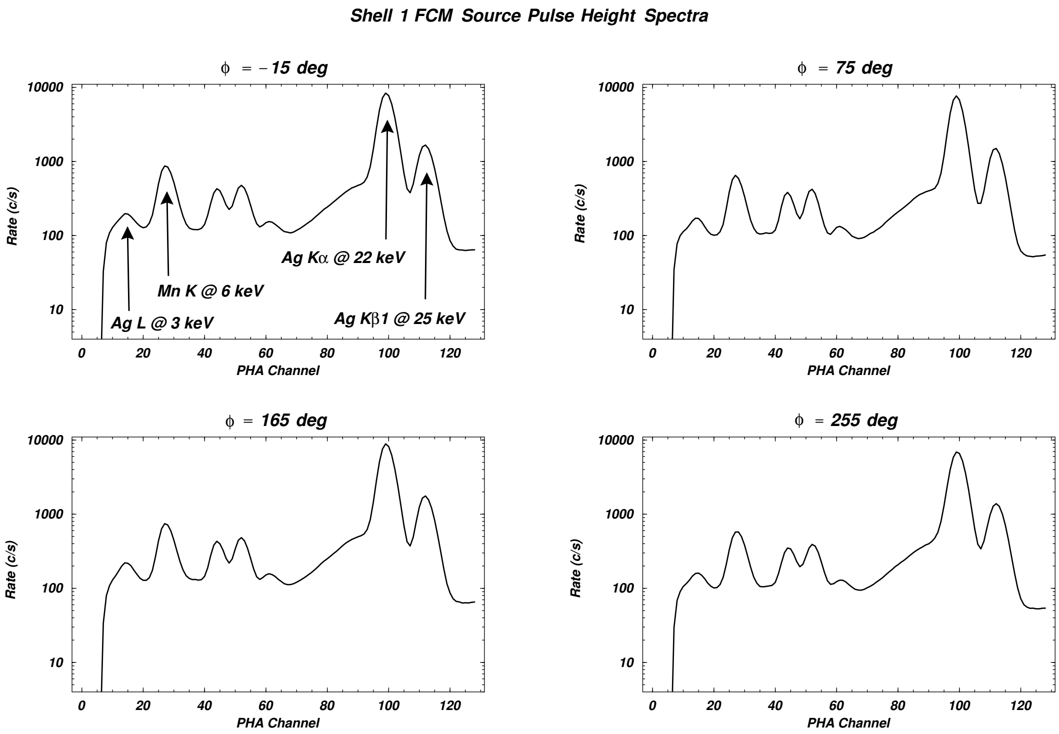

Figure 59: PHA spectra, summed over the source, for the shell 1 FCM sources at each of the 4 azimuths. The prominent Ag K lines at 22 and 25 keV do not reflect from the HRMA and so are not detected by ACIS. PHA spectra for the other shells are very similar, but shifted down as the activities decrease for the inner shells.

6.3 Spectral analysis

So far analysis of FCM data has focused almost exclusively on one data set (TRW ID H-IAS-RC-1.001), which has by far the most data (12,900 s of good time), and was taken with the ACIS detector at a position along the optical axis closest to the expected on-orbit position (~190 mm in front of the finite conjugate focus at XRCF). The position of the optical axis in ACIS detector coordinates was placed near the nominal position for the S array (Fig. 60), and was determined *a posteriori* from an appropriate ACIS boresight position provided by the ACIS team and from the Five Axis Mount (FAM) logs to be (DETX = 4148 pixels, DETY = 2214 pixels). DETX is in the dispersion direction (Y) and DETY is in the SIM motion direction (Z). This position is accurate to within an estimated 10 pixels which we believe is sufficient for purposes of FCM analysis. The six readout CCDs were all four I array front-side-illuminated CCDs and the two S array CCDs S2 (front-side-illuminated) and S3 (back-side-illuminated).

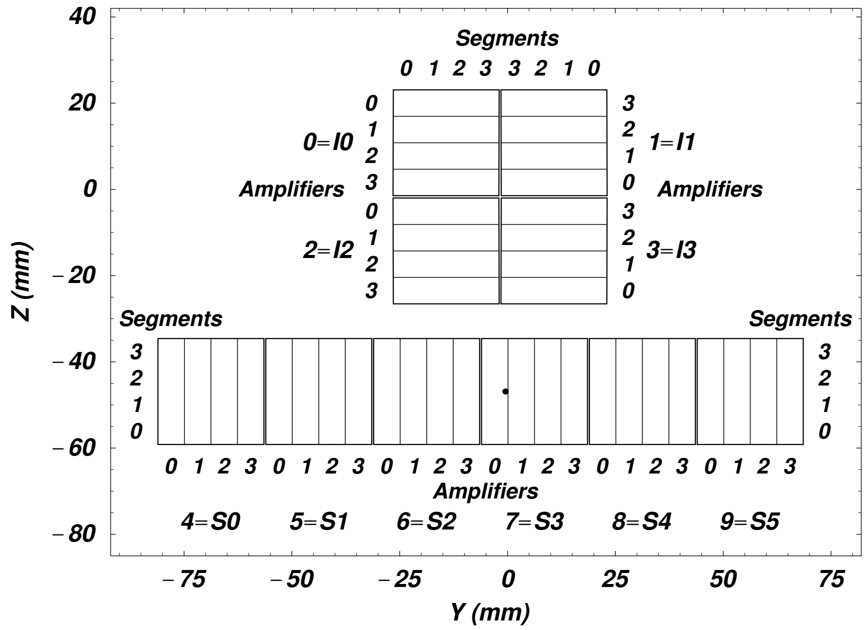

Figure 60: ACIS detector layout showing CCD, amplifier, and segment identifiers. The amplifiers are read out individually, and run horizontally for the I array CCDs and vertically for the S array CCDs. For the spectral and FCC position registration analysis, each amplifier was divided into 4 segments. Also shown by the black dot in amplifier 0 of CCD S3 is the position of the optical axis for the XRCF FCM measurement described in this paper.

ASCA grades 0, 2, 3, 4 and 6 were selected for further analysis. Using resolution curves appropriate for the front-side- and back-side-illuminated CCDS, the spectral content of the detected counts was determined by fitting gaussian lines to the line list [18] given in Table 16 using the following PLT/COD function:

```
! P1,P2 gain offset slope
! P3,P4 resolution parameters
! P5    tail
! Line energies:
VAR eSiKa    1739.8 eSiKa   STO
VAR eSiKb    1835.9 eSiKb   STO
VAR eAuMa    2121.3 eAuMa   STO
VAR eAuMb    2205.0 eAuMb   STO
```

```
VAR eAgLl    2633.7 eAgLl   STO
VAR eAgLn    2806.1 eAgLn   STO
VAR eAgLa    2982.3 eAgLa   STO
VAR eAgLb1   3150.9 eAgLb1  STO
VAR eAgLb4   3203.5 eAgLb4  STO
VAR eAgLb3   3234.5 eAgLb3  STO
VAR eAgLb6   3256.0 eAgLb6  STO
VAR eAgLb2   3347.8 eAgLb2  STO
VAR eAgLg1   3522.6 eAgLg1  STO
VAR eAgLg2   3743.2 eAgLg2  STO
VAR eMnKa    5895.1 eMnKa   STO
VAR eFeKa    6400.0 eFeKa   STO
VAR eMnKb1   6490.4 eMnKb1  STO
VAR eNiKa    7472.4 eNiKa   STO
VAR eCuKa    8041.1 eCuKa   STO
VAR eAuLl    8493.9 eAuLl   STO
VAR eAuLa    9713.0 eAuLa   STO
VAR eSiKEd   1840.0 eSiKEd  STO
! General variable
var Energy
var Shelf
!************************************************************************
! Subroutines:
! push channel on stack, return the Energy
! Assumes E=p1+chan*p2
: gain
p2 * p1 + DUP eSiKEd RCL < IF
P31 -
THEN
;
!*************
! Returns gaussian, push norm, width, energy onto stack
: ngaus
DUP Energy RCL > IF
3 PICK P5 * Shelf RCL + Shelf STO
THEN
Energy RCL - over / dup * 2 / neg exp swap / * 2.50663 / P2 *
;
!*************
! Assume Energy is on stack, return SSD resolution
! Uses sigma = SQRT(P4*E+P3)
: ssdres  P4 * P3 + SQRT ;
!************************************************************************
: calsp
x gain Energy STO
0.0 Shelf STO
0.0
 P6  eSiKa   RCL DUP ssdres SWAP ngaus +
 P7  eAuMa   RCL DUP ssdres SWAP ngaus +
 P8  eAuMb   RCL DUP ssdres SWAP ngaus +
 P9  eAgLl   RCL DUP ssdres SWAP ngaus +
 P10 eAgLn   RCL DUP ssdres SWAP ngaus +
 P11 eAgLa   RCL DUP ssdres SWAP ngaus +
 P12 eAgLb1  RCL DUP ssdres SWAP ngaus +
```

```
 P13 eAgLb4  RCL DUP ssdres SWAP ngaus +
 P14 eAgLb3  RCL DUP ssdres SWAP ngaus +
 P15 eAgLb6  RCL DUP ssdres SWAP ngaus +
 P16 eAgLb2  RCL DUP ssdres SWAP ngaus +
 P17 eAgLg1  RCL DUP ssdres SWAP ngaus +
 P18 eAgLg2  RCL DUP ssdres SWAP ngaus +
 P19 eMnKa   RCL DUP ssdres SWAP ngaus +
 P20 eFeKa   RCL DUP ssdres SWAP ngaus +
 P21 eMnKb1  RCL DUP ssdres SWAP ngaus +
 P22 eAuLa   RCL DUP ssdres SWAP ngaus +
 P23 eNiKa   RCL DUP ssdres SWAP ngaus +
 P24 eCuKa   RCL DUP ssdres SWAP ngaus +
 P25 eAuLl   RCL DUP ssdres SWAP ngaus +
! Escapes
 P26 eAgLa   RCL eSiKa RCL - DUP ssdres SWAP ngaus +
 P27 eAgLb1  RCL eSiKa RCL - DUP ssdres SWAP ngaus +
 P28 eMnKa   RCL eSiKa RCl - DUP ssdres SWAP ngaus +
! Line at specified energy
P30  P29         DUP ssdres SWAP ngaus +
Shelf RCL +
;
```

Fits were first carried out for each amplifier on each of the six readout CCDs (Fig. 60). Holding line widths frozen at their best fit values for each amplifier, fits were then carried out for each segment in order to determine rates in each line. The 96 data points per line resulting from this procedure are sufficient for determining FCC position shifts. Figure §61 shows the fitted spectra for a selected segment on the front-side-illuminated CCD I3 and one on the back-side-illuminated CCD S3. These segments lie near one another and above the optical axis (Fig. 60). The strongest lines in these spectra are the electron-capture lines Ag Lα, the Ag Lβ series, Mn Kα, and Mn Kβ1. The superior energy resolution of the front-side-illuminated CCDs is apparent. Appendix B lists fitted rates for Ag Lα, the sum over the Ag Lβ series, Mn Kα, and Mn Kβ1 in each segment, amplifier and CCD. Comparison of these XRCF line rates with those measured on orbit, corrected for radioactive decay and FCC position shifts, comprises the verification of the AXAF absolute flux calibration transfer and provides the basis for the search for any possible changes in molecular contamination.

Table 16: Line list for spectral fits.

Line	**Energy (keV)**	**Line**	**Energy (keV)**
Si K escape peak for Ag Lα	1.2425	Ag Lγ1	3.5226
Si K escape peak for Ag Lβ1	1.4111	Ag Lγ2	3.7432
Si Kα	1.7398	Si K escape peak for Mn Kα	4.1553
Au Mα	2.1213	Mn Kα	5.8951
Au Mβ	2.2050	Fe Kα	6.4000
Ag Lℓ	2.6637	Mn Kβ1	6.4904
Ag Lη	2.8061	Ni Kα	7.4724
Ag Lα	2.9823	Cu Kα	8.0411
Ag Lβ1	3.1509	Au Lℓ	8.4939
Ag Lβ6	3.2560	Au Lα	9.7130
Ag Lβ2	3.3478		

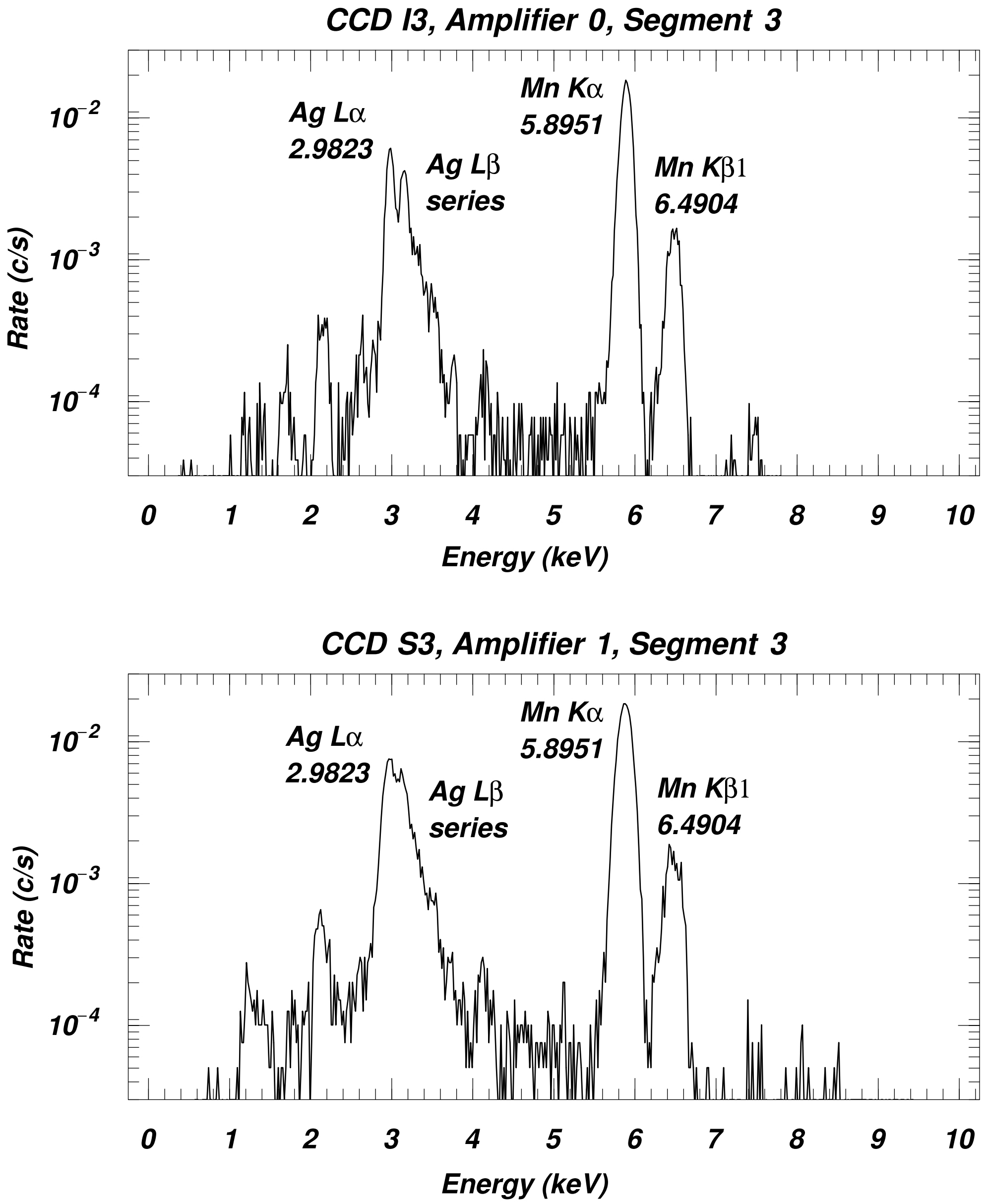

Figure 61: FCM/HRMA/ACIS spectra for a selected segment on the front-side-illuminated CCD I3 (top), and one on the back-side-illuminated CCD S3 (bottom).

6.4 FCM registration analysis

Because the on-orbit positions of the FCM sources relative to the optical axis will change with respect to their XRCF positions due to thermal contraction of the FCC about an off-axis fixed point, as well as launch vibrations, it is necessary to register the FCM images at XRCF and on-orbit by comparing them to simulated images, and to search for positional shifts of the axis of the FCC relative to the optical axis. Eastman-Kodak measured FCM source positions on the FCC with respect to its nominal axis [31]. During XRCF testing, the FCC V-groove-block and cup-cone positioning mechanism was not aligned, and the magnitude of the resulting displacement, while visually estimated at <1 mm mostly in Z, is not known accurately. Simulated images for cross-correlation with the data are generated using the ray trace code written by MSFC Project Science, described in Appendix A, with the as-built HRMA mirror parameters and mirror figure deviations provided by the AXAF Mission Support Team [32]. Table 17 lists the expected displacements of the FCM sources from the centers of the paraboloid apertures assuming the nominal FCC axis was aligned with the optical axis of the P3 mirror. The systematic error in these nominal positions is ±0.2 mm in Y and Z (see §6.2). If these numbers correctly represented reality, the registration procedure should find little if any FCC displacement (*i.e.* $\Delta Y \simeq \Delta Z \simeq 0$). FCM source non-uniformity (§6.2) is included in the ray trace. Nominally the centers of the uniformity maps lie on the centers of the FCM sources; however, there is a systematic uncertainty of ±0.2 mm in Y and Z in the relative positions of these points.

Table 17: Expected FCM displacements (mm) from centers of paraboloid apertures*.

Shell/Azimuth	-15	75	165	255
1	(0.258,-0.051)	(-0.087,-0.159)	(-0.151,0.059)	(-0.180,-0.505)
3	(0.221,-0.059)	(-0.061,-0.228)	(-0.078,0.021)	(-0.135,-0.505)
4	(0.213,-0.030)	(-0.066,-0.219)	(-0.077,0.048)	(-0.134,-0.475)
6	(0.092,-0.005)	(-0.069,-0.240)	(-0.227,-0.042)	(-0.137,-0.495)

* Assuming the nominal FCC axis aligned with the the optical axis of mirror P3. The first number is for Y and the second for Z.

The ACIS flat fields at Nb Lα (E = 2.165 keV) and Fe Kα (E = 6.400 keV) are very flat (< 1% variations) when all grades are accepted. However, for the back-side-illuminated CCD S3, accepting only ASCA grades 0, 2, 3, 4 and 6, and applying a spectral analysis similar to that described in §6.3, these flat fields do show noticeable variations. For S3, the variation is about 8% and 19% at 2.165 and 6.400 keV, respectively, with the highest response closest to and the lowest response furthest from the readout (Table 18). For the correlation analysis we correct the S3 rates derived from the spectral analysis (§6.3) for this flat field effect by interpolating linearly in energy (Tables 19 and 20). A further small complication, not yet included in the analysis, is the slight difference in vignetting of the first few rows due to frame store shielding for the flat field and FCM measurements. At present, we carry out the cross-correlation registration analysis at the strongest lines, Ag Lα and Mn Kα (E = 2.982 and 5.895 keV, respectively), letting the overall normalization and the relative efficiencies between front-side- and back-side-illuminated CCDs assume values that minimize the value of χ^2 at the various trial positions of the FCC. We also carry out the analysis at the rate weighted average energy of the Ag Lβ series (E = 3.198) and at Mn Kβ1 (E = 6.490 keV).

Although the ray-trace images generated using the Project Science ray trace code appear to adequately reproduce the XRCF images (Fig. 62), in fact the results given in Table 21 show that the best-fits are statistically unacceptable. The left-hand side of Fig. 63 shows error contours established by rescaling χ^2 values to 1 per degree of freedom at the best-fit [33] assuming the nominal positions of the FCM on the FCC and perfect alignment of the uniformity map and FCM centers. For this case the FCC position shift derived at Mn Kα does not agree within the assigned errors with that derived at Ag Lα or at the Ag Lβ series, although the Ag L results are in agreement with each other. Obviously the FCC position shift should not depend on energy.

Possible explanations for this disagreement include, but are not limited to, shifts within tolerances of the FCM positions away from their nominal values on the FCC, and misalignment within tolerances of the uniformity map centers with the FCM centers. It is possible to bring the Mn Kα FCC position shift into better agreement with the Ag L results by appealing to these tolerances, although the fits are still statistically unacceptable. The right-hand side of Fig. 63 shows errors contours calculated as before but assuming:

1. All shell 1 FCM sources are shifted from their nominal positions on the FCC by -0.1 mm in Y and +0.2 mm in Z.
2. All shell 3, 4, and 6 FCM sources are shifted from their nominal positions on the FCC by +0.1 mm in Y and -0.2 mm in Z.
3. All shell 1 uniformity map centers are shifted from their nominal positions relative to the FCM centers by +0.1 mm in Y and -0.2 mm in Z.
4. All shell 3, 4, and 6 uniformity map centers are shifted from their nominal positions relative to the FCM centers by -0.1 mm in Y and +0.2 mm in Z.

The chosen shifts in Z are at the extreme limits of the tolerances. Table 21 lists the registration results for the nominal case and for the case with the shifts described above. Also given are mean values weighted by the assigned errors. Projections of the FCM sources onto the paraboloid apertures shows that these results imply a slight vignetting of the shell 6 source at an azimuth of 75 deg (Fig. 64). The individual FCM sources are securely mounted in the FCC so that we do not expect any change after launch in their relative positions except that due to a slight thermal contraction of the FCC on-orbit.

Table 18: Fitted flat field corrections (ASCA grades 0, 2, 3, 4 and 6), normalized to an average value of unity, for the back-side-illuminated CCD S3 at Nb Lα (E = 2.165 keV) and Fe Kα (E = 6.400 keV).

segment	0	1	2	3	segment	0	1	2	3
amplifier	E = 2.165 keV				amplifier	E = 6.400 keV			
0	1.004	1.008	1.000	0.949	0	1.083	1.052	0.989	0.889
1	1.008	1.024	1.000	0.993	1	1.073	1.058	1.000	0.926
2	0.997	1.028	1.012	0.997	2	1.068	1.047	1.005	0.926
3	1.008	1.012	0.997	0.961	3	1.047	1.010	0.937	0.889

Table 19: Interpolated flat field corrections (ASCA grades 0, 2, 3, 4 and 6) for the back-side-illuminated CCD S3 at Ag Lα (E = 2.982 keV) and the rate weight mean energy for the Ag Lβ series (E = 3.198 keV).

segment	0	1	2	3	segment	0	1	2	3
amplifier	E = 2.982 keV				amplifier	E = 3.198 keV			
0	1.020	1.017	0.998	0.938	0	1.024	1.019	0.998	0.935
1	1.021	1.031	1.000	0.980	1	1.024	1.032	1.000	0.976
2	1.010	1.032	1.011	0.983	2	1.014	1.033	1.010	0.979
3	1.016	1.012	0.985	0.947	3	1.018	1.012	0.982	0.944

Table 20: Interpolated flat field corrections (ASCA grades 0, 2, 3, 4 and 6) for the back-side-illuminated CCD S3 at Mn Kα (E = 5.895 keV) and Mn Kβ1 (E = 6.490 keV).

segment	0	1	2	3	segment	0	1	2	3
amplifier	E = 5.895 keV				amplifier	E = 6.490 keV			
0	1.074	1.047	0.991	0.896	0	1.086	1.053	0.989	0.888
1	1.066	1.054	1.000	0.934	1	1.075	1.058	1.000	0.925
2	1.060	1.045	1.006	0.934	2	1.070	1.047	1.005	0.925
3	1.042	1.010	0.944	0.898	3	1.048	1.010	0.935	0.888

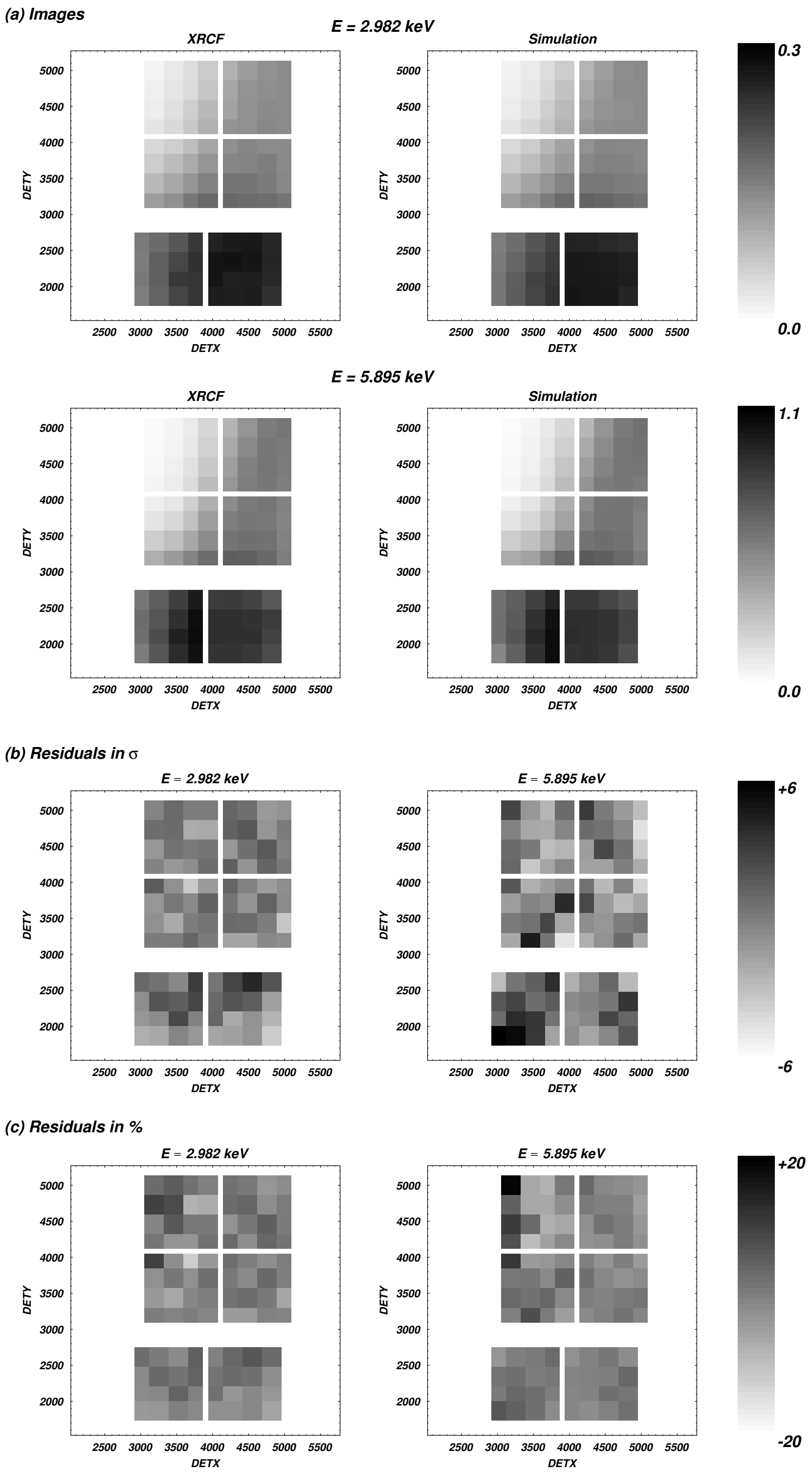

Figure 62: FCC registration results at 2.982 keV and 5.895 keV, for FCM located at their nominal positions on the FCC and for perfect alignment of the uniformity map centers. (a) XRCF images are shown on the left and the best-fit ray-trace images on the right. (b) Residuals in sigma. (c) Residuals in percent.

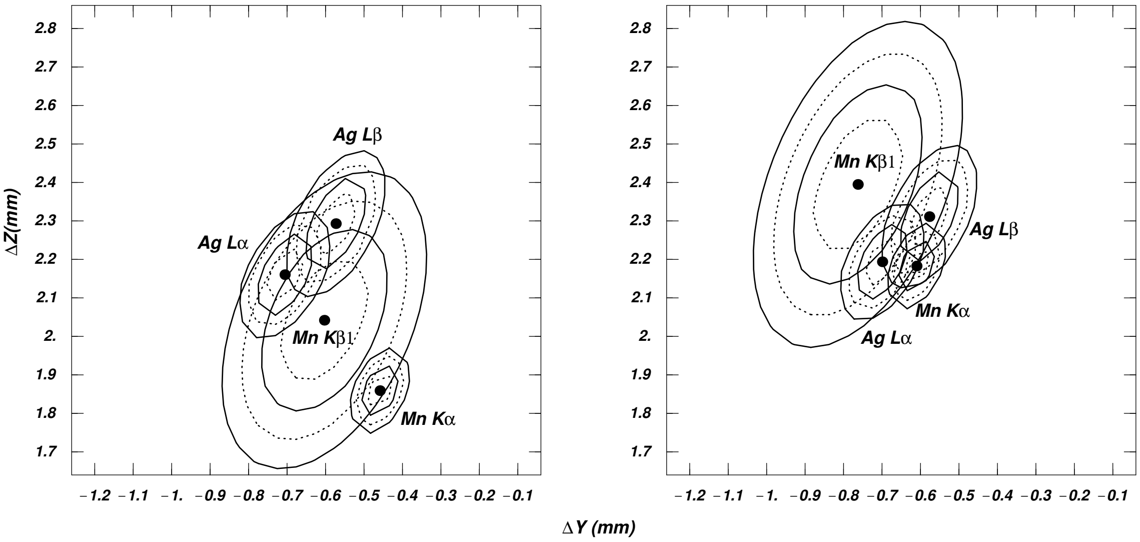

Figure 63: Best-fit values for ΔY and ΔZ and error contours derived by rescaling χ^2 so that $\chi^2_{min} = 94$ and setting $\chi^2 = \chi^2_{min} + \Delta\chi^2$ with $\Delta\chi^2 = 1$, 2.30, 4, and 6.17. Extremes on the $\Delta\chi^2 = 1$ and 4 contours determine the 1σ and 2 σ single parameter errors, while the $\Delta\chi^2 = 2.30$ and 6.17 contours enclose the 68.3% and 95.4% two parameter confidence levels. Left: Results for nominal positions of the FCM on the FCC and for perfect alignment of the FCM and uniformity map centers. Right: Results for a particular choice (see text) of FCM positions shifts on the FCC and misaligned uniformity map centers. The chosen shifts in Z are at the extreme limit of the tolerances.

Table 21: Present status of registration analysis. The values of ΔY and ΔZ are shifts of the FCC center from its nominal position at Y = 0 and Z = 0.

	Nominal				With shifts			
Energy (keV)	χ^2_{min} *	**ΔY† (mm)**	**ΔZ† (mm)**	**Corr.**	χ^2_{min} *	**ΔY† (mm)**	**ΔZ† (mm)**	**Corr.**
2.982	201.5	-0.706±0.041	2.160±0.058	0.52	183.9	-0.699±0.038	2.194±0.053	0.53
3.198	242.2	-0.573±0.044	2.293±0.065	0.48	246.5	-0.577±0.043	2.311±0.064	0.49
5.895	455.2	-0.459±0.029	1.859±0.040	0.70	439.5	-0.610±0.028	2.183±0.040	0.66
6.490	452.5	-0.603±0.097	2.042±0.140	0.59	457.4	-0.763±0.098	2.395±0.150	0.55
Weighted means		-0.550±0.020	2.025±0.029			-0.633±0.020	2.217±0.028	

* These fits are statistically unacceptable.

† Errors are standard (1σ, 1 parameter) errors based on rescaling χ^2_{min} to 1 per degree of freedom.

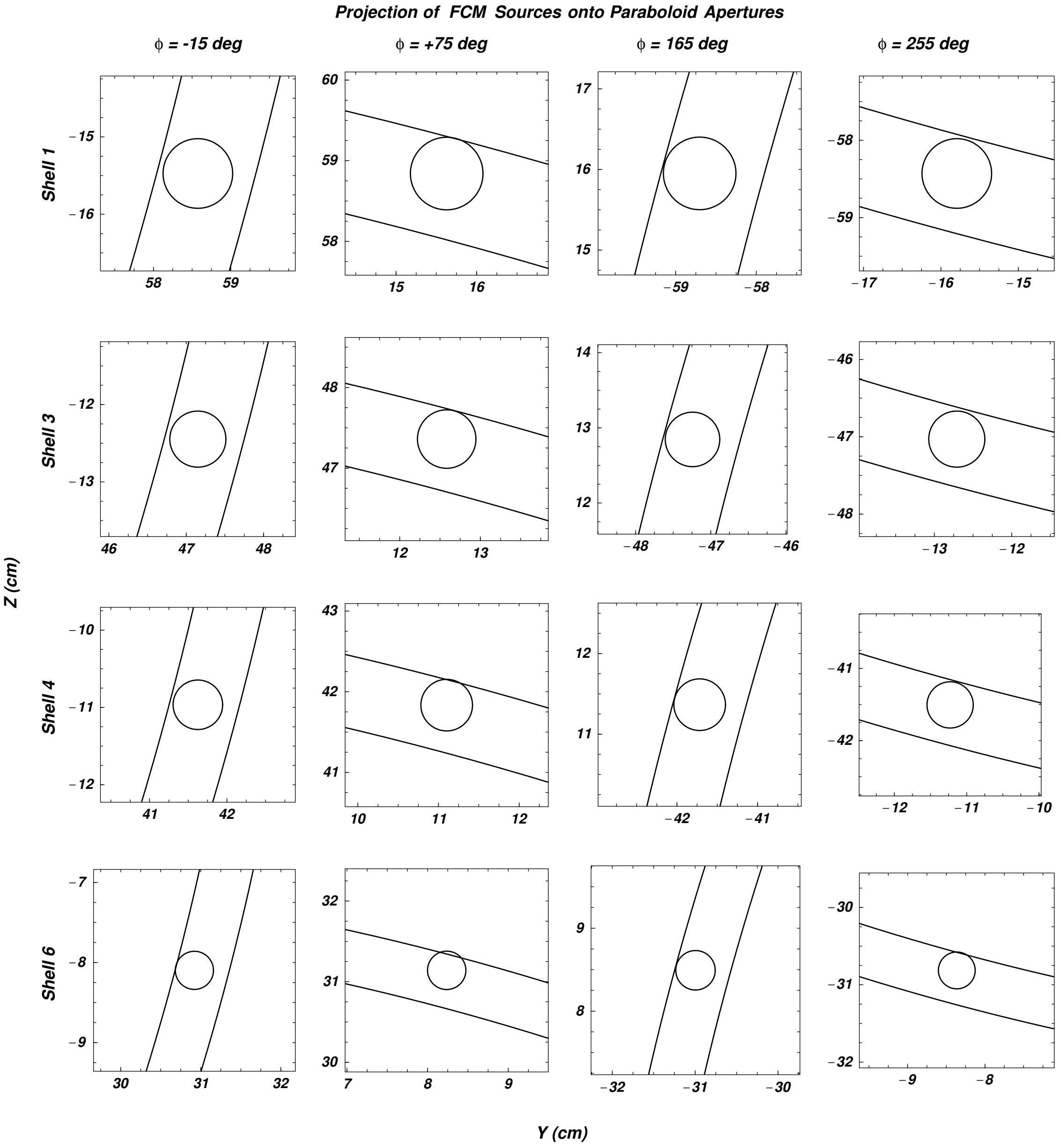

Figure 64: Projections of the FCM sources, including FCC displacement from its nominal position using ΔY = -0.633 mm and ΔZ = +2.217 mm (see the case with shifts in Table 21), onto the aperture of the paraboloids. For shell 6, there is a slight vignetting of the source at an azimuth of 75 deg.

6.5 Future Work

After launch the present plan is for a 30,000 s measurement with the four I array CCDs plus S2 and S3 and a 30,000 s measurement with the six S array CCDs. For both measurements, the ACIS detector will be in its launch-lock position with the optical axis in S3, same as for the XRCF measurement described here. We will:

1. Analyze the on-orbit FCM/HRMA/ACIS data in a manner consistent with the analysis presented here.
2. Register images at as many energies as possible, taking into account thermal contraction of the FCC (Table 22).
3. Compare the on-orbit rates with XRCF rates and model predictions, including the effects of FCC position shifts and FCM source decay.
4. Resolve discrepancies.

Table 22: Expected changes in source ΔY, ΔZ and ΔR, in mm, due to on-orbit thermal contraction about the fixed point Y = 0.9525 cm and Z = 65.438 cm, assuming a temperature change from ground (at XRCF) to orbit of -32 F. The values tabulated here change only slightly if alignment shifts slightly change the position of the fixed point.

ϕ	-15°			75°			165°			255°		
S	ΔY	ΔZ	ΔR	ΔY	ΔZ	ΔR	ΔY	ΔZ	ΔR	ΔY	ΔZ	ΔR
1	-.240	+.338	-.319	-.061	+.028	+.012	+.248	+.207	-.186	+.069	+.516	-.517
3	-.192	+.325	-.270	-.049	+.076	+.061	+.200	+.220	-.137	+.057	+.469	-.467
4	-.169	+.319	-.246	-.042	+.099	+.085	+.177	+.226	-.113	+.050	+.446	-.444
6	-.125	+.307	-.200	-.031	+.144	+.131	+.133	+.238	-.067	+.039	+.401	-.398

Finally, we will work with the AXAF Mission Support Team and the AXAF Science Center to interpret results with respect to absolute flux calibration and to implications for HRMA modelling (*e.g.*, changes in molecular contamination). We hope and expect that there will be none.

7 Limits on HRMA contamination

7.1 Objectives

The principal objective is to measure or establish upper limits on any contamination of the HRMA mirrors.

7.1.1 Molecular contamination

Molecular contamination can significantly alter the reflectance of grazing-incidence optics [23]. Recognition of this led to stringent control of molecular contamination, resulting in very little molecular-film accumulation on optical witness samples accompanying the HRMA mirrors.

7.1.2 Particulate contamination

Particulate contamination clearly degraded the performance of the AXAF's Verification and Engineering Test Assembly – 1 (VETA-1) [25, 26], primarily by producing more scattered x radiation at lower energies than effected by surface roughness. Realization of this led to stringent control of particulate contamination, resulting in very little accumulation of particulates on optical witness samples accompanying the HRMA mirrors. Consequently, we expect to find little x-ray evidence for dust.

7.2 Procedures

7.2.1 Molecular contamination

The primary x-ray means for detecting a molecular film on the HRMA mirrors are effective-area measurements (e.g., §5.1, [34, 22]). A thin molecular film would increase the HRMA's effective area above the Ir-M_V edge near 2 keV and would produce weak absorption features at energies corresponding to atomic edges of the film's constituent materials.

7.2.2 Particulate contamination

The primary x-ray means for detecting particulates on the HRMA mirrors are to measure the scattering through wing-scan and encircled-energy measurements (e.g., [8]). In addition, shutter-focus and ring-focus measurements (e.g., [27]) provide semi-quantitative information. The energy dependence and the out-of-plane component of the scattering distinguish the effects of dust from those of surface roughness.

7.3 Status

Analyses to measure contamination are derivative to other measurements, as mentioned above. Furthermore, neither the optical witness samples nor the x-ray testing showed any evidence for substantial contamination. Consequently, we have assigned analyses of contamination a low priority.

7.3.1 Molecular contamination

As discussed above, we have assigned a low priority to analyses to bound the molecular contamination. In addition, the current inability of models to account for the observed effective area, to within about 10%, limits our ability to use the effective-area measurements to bound the level molecular contamination.

7.3.2 Particulate contamination

As discussed above, we have assigned a low priority to analyses to bound the particulate contamination.

7.4 Data products

Because this analysis is derivative to other analyses, we or others will have presented the primary data products elsewhere. Data products specific to the analysis of contamination will appear as a brief report, to be linked from the Project Science Calibration web page (`wwwastro.msfc.nasa.gov/xray/xraycal/`).

A Project Science ray-trace code

A.1 Purpose

Long, long ago, in a galaxy far, far away,....

Before the VETA-1 test, Project Science decided that it was worthwhile to develop its own ray trace code for the following reasons:

1. To have its own tool for understanding the design of the HRMA, and the effect of design changes.
2. To have an independent code as a check on the codes maintained by the Mission Support Team (MST) and others.

The Project Science ray trace code does not have all the features of the high-fidelity code maintained by the Mission Support Team, but it permits reasonably rapid response when new studies are needed. Most often work can proceed without requests for ray files generated by the MST. It has proven useful in studies of coating materials for the HRMA, the effects of coating properties such as density and density gradients on HRMA throughput, comparison of effective area measurements and predictions, and studies of the FCM system both for design and for predictions to fit to FCM data. While algorithm development was carried out in *Mathematica*$^{\mathrm{TM}}$, the code is in FORTRAN and runs on a SGI ORIGIN computer at MSFC. The code uses the as-built HRMA parameters and mirror figure deviations provided by the AXAF MST [32] (we especially thank Leon Van Speybroeck, Terry Gaetz, Ping Zhao, and Diab Jerius for providing these data and for helpful discussions). The Project Science ray trace code reproduces the effective areas predicted by the MST code [35]. It also reproduces the XRCF focal lengths for individual mirror shells given in the MST preliminary report on HRMA calibration results [32]. The Project Science code predicts on-orbit focal lengths for the four mirror shells that are $\sim 100\mu$m longer than those predicted by MST. This is most probably due to differing methods used for figure error interpolation (MST uses spline interpolation while Project Science uses simple linear interpolation), and the resulting differences in mean grazing angle adjustments. Here we briefly describe the Project Science ray trace code and what it can and cannot do.

A.2 Geometric ray trace

The Project Science ray trace code is primarily a tool for the geometric tracing of rays through a Wolter Type-I paraboloid-hyperboloid x-ray telescope. The main body of the code divides into:

1. Setup.
2. Ray initiation according to chosen source properties.
3. Propagation through the thermal pre-collimator.
4. Propagation through the paraboloid.
5. Propagation through the central aperture plate.
6. Propagation through the hyperboloid.
7. Propagation to a nominal focal plane.
8. Record ray position, direction, and reflection grazing angles to a file.
9. Record summary of run upon completion.

Various tasks are carried out in post-processing programs which we describe in §A.4.

A.2.1 Setup

As one might expect, the setup section of the code defines various constants, sets up arrays, asks the user what type of simulation he wants to run (which shell; with or without figure errors; with or without baffling; number of rays; source type; etc.), and calls subroutines to set the mirror shell and other telescope parameters.

A.2.2 Ray initiation

The initial position and direction of a ray is set according to the type of source chosen by the user. For a point source on the sky, the rays are uniformly distributed in position over the telescope aperture, all with the same off-axis angles (polar and azimuthal) chosen by the user. For a point source at XRCF, rays originate at the source location and are uniformly distributed in direction over an annulus appropriate for the chosen mirror shell. For the FCM, the rays are uniformly distributed in position and direction. The effects of FCM non-uniformity are taken into account in post-processing where individual rays are appropriately weighted according to the FCM uniformity maps (§6.2). In position, the rays originate from within a circle whose radius, chosen by the user, may be larger than the FCM source radius. By noting the recorded initial ray position, the post-processing code can then handle multiple FCC locations using rays from the same run. In direction the rays are limited to a maximum off-axis polar angle chosen by the user. This angle must be large enough to encompass all rays that could reach the region of interest at the detection surface.

A.2.3 Collimators and central aperture plate

Propagation through the thermal pre-collimator, central aperture plate, and thermal post-collimator is handled by straightforward tracing of a straight line along the ray path. Any intersections with plates or struts terminate the ray.

A.2.4 Paraboloid and hyperboloid

Propagation through the paraboloid and hyperboloid are handled by searching for an intersection of ray and mirror, calculating the surface normal and grazing angle at the intersection point, reflecting the ray off the mirror into the appropriate specular direction, and propagating the ray to the end of the mirror. Mirror tilt and despace are applied to the incoming ray before searching for an intersection point, and then removed from the outgoing ray after reaching the end of the mirror. Figure errors are included using a first order perturbation method. First the code finds the intersection with the ideal surface and then corrects to first order in the figure errors. Figure errors are also included in the calculation of the reflected ray direction. Rays that miss either mirror are terminated. The code counts the number of such ghost rays, but does not record them for further analysis. Rays that strike the baffle in the paraboloid of shell 6 are of course also terminated.

A.2.5 Record ray at nominal focus

Doubly reflected rays that pass through the all collimators are propagated to the nominal focus ($X = 0$). Their position, direction, and both grazing angles are then written to a file. In the case of the FCM sources, the initial ray position on the FCC is also written to the file. Upon completion of the run, a summary of the run is recorded.

A.3 Scattering

Scattering from the mirror surfaces in non-specular directions is energy dependent. In order to run large numbers of rays in as short a time as possible, the Project Science ray trace code is designed to carry out energy dependent calculations during post-processing. In principle this procedure should be very accurate for predicting total effective areas and the core of the point-spread-function (PSF), but is less than ideal for scattering which is probably best accounted for during the ray trace run. However, this requires including energy dependences on reflectivity and on scattering through extensive scattering tables, and can be very costly in computer time. Non-specular scattering is important only for the wings of the PSF and for many purposes can be included in post-processing through convolution techniques. For example, it is possible to predict the structure of the PSF wings from knowledge of the high-frequency surface roughness of the mirrors and of the scattering from dust particles without a ray trace [26]. Convolution of the predicted wing and core PSFs then produces a combined predicted PSF.

A.4 Post-processing

A.4.1 FORTRAN

Using the results of the geomtric ray trace to calculate effective areas (without scattering effects) or FCM images (and compare them to FCM data) are post-processing tasks involving extensive numerical calculations of energy dependent reflectivity at two grazing angles for each ray reaching the focal plane. Project Science therefore uses FORTRAN code running on the SGI ORIGIN computer at MSFC to complete these tasks. Reflectivity calculations use an exact recursive algorithm [36], suitable for multilayer coatings, to model the AXAF coatings consisting of $\sim$325 Å of $\sim$95% bulk density iridium on $\sim$100 Å of chromium on zerodur. Above 2 keV, the code uses optical constants for iridium supplied by MST and derived from synchrotron reflectance measurements [19] for iridium coated AXAF witness flats (we especially thank Dale Graessle and his team). All other optical constants come from Henke *et al* [17]. Using the effective area code, it is possible to:

1. Calculate effective areas integrated over the focal plane at large numbers of closely spaced energies.
2. Add a layer of some molecular contaminant (usually a hydrocarbon) on top of the AXAF coatings to study its effects on effective area.
3. Study the effects on effective area of density gradients, in the direction normal to the surface, in the coatings.

Using the FCM code with results from geometric ray traces for each FCM source and each shell, it is possible to:

1. Calculate the expected HRMA/ACIS image of the FCM system as a function of energy and, by noting the initial position of rays, of FCC position.
2. Correlate the predicted images as a function of FCC position with measured images.
3. Study the effects of FCM position tolerances and uniformity map misalignment on the FCC registration results.

A.4.2 *Mathematica*$^{\mathrm{TM}}$

The symbolic mathematics package *Mathematica*$^{\mathrm{TM}}$has proven very useful for a number of tasks, especially:

1. Development of algorithms.
2. Graphical display of results.

For the FCM registration analysis, a *Mathematica*$^{\mathrm{TM}}$notebook is used to refine the correlation results produced by the FORTRAN code by interpolation between grid points, to determine errors, and to display results.

B Fitted FCM line rates at 2.984, 3.198, 5.895, and 6.490 keV

Table 23: Fitted rates for Ag Lα at E = 2.982 keV.

segment	0	1	2	3	segment	0	1	2	3
amplifier	CCD I0				amplifier	CCD I1			
0	0.0139	0.0266	0.0404	0.0611	0	0.136	0.141	0.131	0.127
1	0.0199	0.0314	0.0432	0.0671	1	0.137	0.138	0.129	0.109
2	0.0218	0.0369	0.0583	0.0832	2	0.137	0.133	0.128	0.105
3	0.0320	0.0449	0.0649	0.0933	3	0.136	0.130	0.117	0.0919
	CCD I2					CCD I3			
0	0.0468	0.0583	0.0765	0.106	0	0.162	0.171	0.174	0.177
1	0.0604	0.0790	0.0992	0.125	1	0.141	0.155	0.162	0.162
2	0.0841	0.102	0.126	0.147	2	0.139	0.152	0.145	0.143
3	0.116	0.131	0.159	0.176	3	0.138	0.137	0.142	0.132
	CCD S2					CCD S3			
0	0.152	0.158	0.153	0.156	0	0.271	0.280	0.274	0.245
1	0.183	0.187	0.187	0.173	1	0.269	0.270	0.278	0.264
2	0.218	0.233	0.216	0.198	2	0.268	0.272	0.277	0.266
3	0.236	0.236	0.241	0.234	3	0.245	0.256	0.252	0.242

Table 24: Fitted rates for Ag Lβ series at E = 3.198 keV.

segment	0	1	2	3	segment	0	1	2	3
amplifier	CCD I0				amplifier	CCD I1			
0	0.0146	0.0267	0.0415	0.0694	0	0.136	0.151	0.142	0.128
1	0.0203	0.0295	0.0512	0.0723	1	0.135	0.147	0.140	0.112
2	0.0260	0.0376	0.0567	0.0803	2	0.137	0.145	0.135	0.107
3	0.0328	0.0455	0.0728	0.0997	3	0.140	0.141	0.126	0.0924
	CCD I2					CCD I3			
0	0.0440	0.0643	0.0879	0.109	0	0.163	0.178	0.179	0.180
1	0.0666	0.0810	0.105	0.131	1	0.149	0.153	0.163	0.166
2	0.0922	0.111	0.133	0.154	2	0.148	0.150	0.150	0.152
3	0.117	0.141	0.163	0.174	3	0.138	0.144	0.150	0.134
	CCD S2					CCD S3			
0	0.154	0.166	0.159	0.152	0	0.286	0.275	0.255	0.231
1	0.197	0.190	0.192	0.181	1	0.282	0.283	0.257	0.232
2	0.232	0.231	0.217	0.211	2	0.279	0.276	0.264	0.228
3	0.249	0.244	0.249	0.244	3	0.265	0.259	0.242	0.209

Table 25: Fitted rates for Mn Kα at E = 5.895 keV.

segment	0	1	2	3	segment	0	1	2	3
amplifier	CCD I0				amplifier	CCD I1			
0	0.0221	0.0450	0.0904	0.177	0	0.553	0.586	0.557	0.455
1	0.0245	0.0507	0.107	0.205	1	0.567	0.591	0.550	0.413
2	0.0320	0.0657	0.130	0.240	2	0.575	0.588	0.506	0.373
3	0.0439	0.0788	0.154	0.290	3	0.592	0.567	0.464	0.328
	CCD I2					CCD I3			
0	0.0720	0.111	0.203	0.346	0	0.558	0.652	0.684	0.694
1	0.117	0.170	0.265	0.420	1	0.540	0.608	0.617	0.600
2	0.219	0.276	0.376	0.500	2	0.529	0.576	0.586	0.558
3	0.352	0.431	0.531	0.627	3	0.538	0.592	0.573	0.499
	CCD S2					CCD S3			
0	0.563	0.622	0.631	0.592	0	0.941	0.947	0.890	0.754
1	0.729	0.765	0.729	0.694	1	0.935	0.942	0.900	0.790
2	0.910	0.956	0.892	0.829	2	0.910	0.937	0.887	0.758
3	1.03	1.05	1.04	0.982	3	0.807	0.823	0.793	0.648

Table 26: Fitted rates for Mn Kβ1 at E = 6.490 keV.

segment	0	1	2	3	segment	0	1	2	3
amplifier	CCD I0				amplifier	CCD I1			
0	0.00116	0.00185	0.00420	0.0137	0	0.0510	0.0545	0.0528	0.0372
1	0.00205	0.00419	0.00682	0.0161	1	0.0591	0.0553	0.0497	0.0327
2	0.00139	0.00420	0.00910	0.0160	2	0.0568	0.0581	0.0452	0.0277
3	0.00340	0.00551	0.0123	0.0206	3	0.0575	0.0566	0.0393	0.0222
	CCD I2					CCD I3			
0	0.00533	0.00676	0.0134	0.0276	0	0.0495	0.0588	0.0604	0.0621
1	0.00638	0.0107	0.0187	0.0343	1	0.0498	0.0580	0.0579	0.0527
2	0.0163	0.0197	0.0277	0.0406	2	0.0477	0.0629	0.0553	0.0500
3	0.0275	0.0299	0.0402	0.0532	3	0.0513	0.0550	0.0548	0.0410
	CCD S2					CCD S3			
0	0.0431	0.0548	0.0632	0.0575	0	0.0993	0.0847	0.0718	0.0554
1	0.0559	0.0663	0.0791	0.0605	1	0.101	0.0922	0.0780	0.0554
2	0.0828	0.0847	0.0788	0.0738	2	0.0983	0.0890	0.0709	0.0552
3	0.0918	0.0932	0.0964	0.0912	3	0.0848	0.0717	0.0609	0.0488

References

[1] M. C. Weisskopf and S. L. O'Dell, "Calibration of the AXAF observatory: Overview," in *Grazing Incidence and Multilayer X-Ray Optical Systems*, R. B. Hoover and A. B. Walker, eds., *Proc. SPIE* **3113**, pp. 2–17, 1997.

[2] J. J. Kolodziejczak, R. A. Austin, R. F. Elsner, M. K. Joy, M. E. Sulkanen, E. M. Kellogg, and B. J. Wargelin, "X-ray source system at the Marshall Space Flight Center X-Ray Calibration Facility," in *X-Ray and Extreme Ultraviolet Optics*, R. B. Hoover and A. B. Walker, eds., *Proc. SPIE* **2515**, pp. 420–435, 1995.

[3] R. F. Elsner, M. K. Joy, S. L. O'Dell, B. D. Ramsey, and M. C. Weisskopf, "Ground-to-orbit transfer of the AXAF-I flux scale: In-situ contamination monitoring of x-ray telescopes," in *Multilayer and grazing incidence X-ray/EUV optics for astronomy and projection lithography*, R. B. Hoover and A. B. Walker, eds., *Proc. SPIE* **2279**, pp. 332–342, 1994.

[4] B. J. Wargelin, J. P. Hughes, E. M. Kellogg, and T. J. Norton, "Ground calibration of AXAF: The HRMA X-ray Detection System," *Bull. Am. Astron. Soc.* **187**, p. 7703, 1995.

[5] W. C. McDermott, E. M. Kellogg, B. J. Wargelin, I. N. Evans, S. A. Vitek, E. Y. Tsiang, D. A. Schwartz, R. J. Edgar, S. Kraft, F. Scholze, R. Thornagel, G. Ulm, M. C. Weisskopf, S. L. O'Dell, A. F. Tennant, J. J. Kolodziejczak, and G. Zirnstein, "The AXAF HXDS germanium solid-state-detectors," in *EUV, X-Ray, and Gamma-Ray Instrumentation for Astronomy VIII*, O. H. Siegmund and M. A. Gummin, eds., *Proc. SPIE* **3114**, pp. 535–543, 1997.

[6] S. Kraft, F. Scholze, R. Thornagel, G. Ulm, W. C. McDermott, and E. M. Kellogg, "High-accuracy calibration of the HXDS HPGe detector at the PTB radiometry laboratory at BESSY," in *EUV, X-Ray, and Gamma-Ray Instrumentation for Astronomy VIII*, O. H. Siegmund and M. A. Gummin, eds., *Proc. SPIE* **3114**, pp. 101–112, 1997.

[7] M. C. Weisskopf, S. L. O'Dell, and L. P. Van Speybroeck, "Advanced X-ray Astrophysics Facility (AXAF): An overview," in *Multilayer and Grazing Incidence X-Ray/EUV Optics III*, R. B. Hoover and A. B. Walker, eds., *Proc. SPIE* **2805**, pp. 2–7, 1996.

[8] L. P. Van Speybroeck, D. Jerius, R. Edgar, T. Gaetz, P. Zhao, and P. Reid, "Performance expectation versus reality," in *Grazing Incidence and Multilayer X-Ray Optical Systems*, R. B. Hoover and A. B. Walker, eds., *Proc. SPIE* **3113**, pp. 89–104, 1997.

[9] S. S.Murray, J. H. Chappell, A. T. Kenter, K. Kobayashi, R. P. Kraft, G. R. Meehan, M. V. Zombeck, G. W. Fraser, J. F. Pearson, J. E. Lees, A. N. Brunton, S. E. Pearce, M. Barbera, A. Collura, and S. Serio, "AXAF High-Resolution Camera (HRC)," in *EUV, X-Ray, and Gamma-Ray Instrumentation for Astronomy VIII*, O. H. Siegmund and M. A. Gummin, eds., *Proc. SPIE* **3114**, pp. 11–25, 1997.

[10] E. Y. Tsiang, "JMKmod User Manual," *SAO publication* **SAO-AXAF-DR-97-276**, 1997.

[11] K. A. Arnaud, "XSPEC: The first ten years," in *Astronomical Data Analysis Software and Systems*, G. J. V and J. Barnes, eds., *ASP Conference Series* **101**, pp. 17–20, 1996.

[12] B. J. Wargelin, E. M. Kellogg, W. C. McDermott, I. N. Evans, and S. Vitek, "AXAF calibration: the HXDS flow proportional counters," in *Grazing Incidence and Multilayer X-Ray Optical Systems*, R. B. Hoover and A. B. Walker, eds., *Proc. SPIE* **3113**, pp. 526–534, 1997.

[13] E. Y. Tsiang, R. E. Edgar, S. Vitek, and A. F. Tennant, "JMKMOD: A software suite within XSPEC for the ground calibration of AXAF," in *Grazing Incidence and Multilayer X-Ray Optical Systems*, R. B. Hoover and A. B. Walker, eds., *Proc. SPIE* **3113**, pp. 132–141, 1997.

[14] R. E. Edgar, E. Y. Tsiang, A. F. Tennant, S. Vitek, and D. A. Swartz, "Spectral fitting in AXAF calibration detectors," in *Grazing Incidence and Multilayer X-Ray Optical Systems*, R. B. Hoover and A. B. Walker, eds., *Proc. SPIE* **3113**, pp. 124–131, 1997.

[15] K. Jahoda and D. McCammon, "Proportional counters as low-energy photon detectors," *Nucl. Inst. Meth.* **A272**, p. 800, 1988.

[16] P. R. Bevington, *Data Reduction and Error Analysis for the Physical Sciences*, McGraw-Hill, New York, New York, 1969.

[17] B. L. Henke, E. M. Gullikson, and J. C. Davis, "X-ray interactions: Photoabsorption, scattering, transmission, and reflection at E = 50–30000 eV, Z = 1–92," *Atomic Data & Nuclear Data Tables* **54**, pp. 181–342, 1993.

[18] J. A. Bearden, "X-ray wavelengths," *Rev. Mod. Phys.* **39**, pp. 78–124, 1967.

[19] D. E. Graessle, A. J. Burek, J. J. Fitch, B. Harris, D. A. Schwartz, and R. L. Blake, "Optical constants from synchrotron reflectance measurements of AXAF witness mirrors 2–12 keV," in *Grazing Incidence and Multilayer X-Ray Optical Systems*, R. B. Hoover and A. B. Walker, eds., *Proc. SPIE* **3113**, pp. 52–64, 1997.

[20] D. E. Graessle, J. J. Fitch, B. Harris, P. Hsieh, D. Nguyen, J. Hughes, D. A. Schwartz, and R. L. Blake, "Calibration of AXAF mirrors using synchrotron radiation," *Bull. Am. Astron. Soc.* **187**, p. 7705, 1995.

[21] J. J. Fitch, R. L. Blake, A. J. Burek, A. M. Clark, D. E. Graessle, B. Harris, D. A. Schwartz, and J. Sweeney, "AXAF synchrotron witness mirror calibrations 2–12 keV," in *Grazing Incidence and Multilayer X-Ray Optical Systems*, R. B. Hoover and A. B. Walker, eds., *Proc. SPIE* **3113**, pp. 30–39, 1997.

[22] E. M. Kellogg, L. Cohen, R. J. Edgar, I. N. Evans, M. Freeman, T. Gaetz, D. Jerius, W. C. McDermott, P. McKinnon, S. S. Murray, W. Podgorski, D. A. Schwartz, L. P. Van Speybroeck, B. Wargelin, M. V. Zombeck, M. C. Weisskopf, R. F. Elsner, S. L. O'Dell, B. D. Ramsey, A. F. Tennant, J. J. Kolodziejczak, G. Garmire, J. Nousek, S. Kraft, F. Scholze, R. Thornagel, G. Ulm, K. Flanagan, D. Dewey, M. Bautz, S. Texter, J. Arenberg, and R. Carlson, "Absolute calibration of the AXAF telescope effective area," in *Grazing Incidence and Multilayer X-Ray Optical Systems*, R. B. Hoover and A. B. Walker, eds., *Proc. SPIE* **3113**, pp. 515–525, 1997.

[23] R. F. Elsner, S. L. O'Dell, and M. C. Weisskopf, "Molecular contamination and the calibration of AXAF," in *Multilayer and grazing incidence X-ray/EUV optics for astronomy and projection lithography*, R. B. Hoover and A. B. Walker, eds., *Proc. SPIE* **1742**, pp. 6–12, 1993.

[24] D. E. Graessle, T. H. Burbine, J. J. Fitch, W. A. Podgorski, J. Z. Juda, R. F. Elsner, S. L. O'Dell, and J. M. Reynolds, "Molecular contamination study of iridium-coated x-ray mirrors," in *Advances in Multilayer and Grazing Incidence X-Ray/EUV/FUV Optics*, R. B. Hoover and A. B. Walker, eds., *Proc. SPIE* **2279**, pp. 12–26, 1994.

[25] J. J. Kolodziejczak, S. L. O'Dell, R. F. Elsner, and M. C. Weisskopf, "Evidence for dust contamination on the VETA-1 mirror surface," in *Multilayer and grazing incidence X-ray/EUV optics for astronomy and projection lithography*, R. B. Hoover and A. B. Walker, eds., *Proc. SPIE* **1742**, pp. 162–170, 1993.

[26] S. L. O'Dell, R. F. Elsner, J. J. Kolodziejczak, M. C. Weisskopf, J. P. Hughes, and L. P. Van Speybroeck, "X-ray evidence for particulate contamination on the AXAF VETA-1 mirrors," in *Multilayer and grazing incidence X-ray/EUV optics for astronomy and projection lithography*, R. B. Hoover and A. B. Walker, eds., *Proc. SPIE* **1742**, pp. 171–182, 1993.

[27] T. J. Gaetz, R. J. Edgar, M. D. Freeman, W. A. Podgorski, L. P. Van Speybroeck, P. Zhao, J. Kolodziejczak, and M. Weisskopf, "Focus and alignment of the AXAF optics," in *Grazing Incidence and Multilayer X-Ray Optical Systems*, R. B. Hoover and A. B. Walker, eds., *Proc. SPIE* **3113**, pp. 77–88, 1997.

[28] S. L. O'Dell and M. C. Weisskopf, "Advanced X-ray Astrophysics Facility (AXAF): Calibration overview," in *X-Ray Optics, Instruments, and Missions*, R. B. Hoover and A. B. Walker, eds., *Proc. SPIE* **3444**, pp. 2–18, 1998.

[29] P. Zhao, R. A. Austin, R. J. Edgar, R. F. Elsner, T. J. Gaetz, D. Jerius, J. J. Kolodziejczak, W. C. McDermott, S. L. O'Dell, M. E. Sulkanen, D. A. Schwartz, D. A. Swartz, A. F. Tennant, L. P. Van Speybroeck, B. J. Wargelin, M. C. Weisskopf, and G. Zirnstein, "AXAF mirror effective-area calibration using the C-continuum source and solid-state detectors," in *X-Ray Optics, Instruments, and Missions*, R. B. Hoover and A. B. Walker, eds., *Proc. SPIE* **3444**, pp. 234–257, 1998.

[30] E. Browne and R. B. Firestone, *Table of Radioactive Isotopes*, John Wiley and Sons, New York, 1986.

[31] F. Schwab, "Radiation Source Position." Eastman-Kodak Tech Note No. AXAF-96-0251-SCHWAB, November 8 1997.

[32] R. J. Edgar, L. P. David, T. J. Gaetz, D. Jerius, D. A. Schwartz, J. Everett, P. Zhao, L. M. Cohen, and W. A. Podgorski, "XRCF Phase 1 Testing: Preliminary Results." SAO-AXAF-DR-97-282, May 28 1997.

[33] W. H. Press, S. A. Teukolsky, W. T. Vetterling, and B. P. Flannery, *Numercial Recipes in FORTRAN, 2nd edition*, Cambridge University Press, Cambridge, 1992.

[34] J. J. Kolodziejczak, R. A. Austin, R. F. Elsner, S. L. O'Dell, M. E. Sulkanen, D. A. Swartz, A. F. Tennant, M. C. Weisskopf, G. Zirnstein, and W. C. McDermott, "Uses of continuum radiation in the AXAF calibration," in *Grazing Incidence and Multilayer X-Ray Optical Systems*, R. B. Hoover and A. B. Walker, eds., *Proc. SPIE* **3113**, pp. 65–76, 1997.

[35] D. Jerius, "Comparison of Project Science and MST Effective Area Simulations." SAO/MST memorandum, March 13 1997.

[36] R. F. Elsner, S. L. O'Dell, and M. C. Weisskopf, "Effective area of the axaf x-ray telescope: Dependence upon dielectric constants of coating materials," *J. X-ray Sci. and Tech.* **3**, pp. 35–44, 1991.